THE UNIVERSITY OF CHICAGO

THE SEARCH FOR THE DECAY $K_L \to \pi^0 e^+ e^-$

A DISSERTATION SUBMITTED TO
THE FACULTY OF THE DIVISION OF THE PHYSICAL SCIENCES
IN CANDIDACY FOR THE DEGREE OF
DOCTOR OF PHILOSOPHY

DEPARTMENT OF PHYSICS

BY
NANCY JIN-JIN LAI

CHICAGO, ILLINOIS
MARCH 2003

TABLE OF CONTENTS

LIST OF FIGURES

LIST OF TABLES

ABSTRACT

The KTeV/E799 experiment at Fermilab has finished analyzing the 1999-2000 data for the rare kaon decay $K_L \to \pi^0 e^+ e^-$. This mode is of interest because it is expected to have a large CP-violating component. The measurement of its branching ratio could support Standard Model predictions through the CKM mechanism for CP violation or it could indicate the existence of new physics. One event is observed in the 1999-2000 data, with the expected background at 0.99 ± 0.22 events. We set a branching ratio upper limit of 3.5×10^{-10} at the 90% confidence level.

ACKNOWLEDGEMENTS

Many people contributed to this thesis in a number of ways. Without them, this work would not have been possible. I would like to take this time to thank them.

First and foremost, I would like to thank my advisor, Yau Wai Wah, for his support and guidance. I will always be deeply grateful for his generosity in helping me achieve my goals. I have been very lucky to have the opportunity to learn from him. He has that remarkable combination of creative insight coupled with results-oriented practicality that is so rare and yet so crucial for success in experimental high energy physics. I hope that I have, in at least some small measure, been able to learn this important skill.

I would also like to thank my colleagues on KTeV, who have put so much work into building the hardware and writing the software. They made the task of transitioning from a very large-scale collider experiment to a much smaller fixed target experiment so smooth and easy. Among my KTeV collaborators, I would like to recognize the following people for their particular assistance: Ed Blucher, Rick Kessler, Sasha Glazov, Elizabeth Turner Worcester, Valmiki Prasad, Miguel Barrio, Leo Bellantoni, Greg Graham, Jason LaDue, Pat Toale, Tony Barker, John Shields, Angela Bellavance, Marjorie Corcoran, Elliott Cheu, and Jason Hamm.

I thank Carla Grosso-Pilcher for her friendship and support throughout the years. Thanks also to Marty Dippel for making the computers and other electronic gadgets throughout HEP run so smoothly, and for our chats on life and philosophy. I am also grateful for the help of our capable and efficient administrative assistants, Vicki McClain-Stone and Aspasia Sotir-Plutis.

I am grateful for the financial support from the Department of Defense National Defense Science and Engineering Graduate Fellowship, the Lucent Technologies Graduate Research Fellowship, and the University of Chicago Grainger Fellowship. I also appreciate the financial support from the Department of Energy and the National Science Foundation.

The support and encouragement of my family and friends has meant very much to me over the years. To Pete, thanks for believing in me when I doubted. This is the end of a time, and a time for a new beginning.

NANCY J. LAI
Chicago, Illinois
February 2003

CHAPTER 1
INTRODUCTION

1.1 CP Symmetry

1.1.1 Parity (P)

The parity transformation changes the sign of all spatial coordinates with respect to a given origin. This operation is the same as a mirror reflection through a plane, followed by a rotation of 180° about the normal line.

The laws of classical physics remain invariant under this operation. In quantum mechanics, a parity operator P may be defined. P is Hermitian and unitary, and its eigenvalues are ± 1. The fundamental particles have intrinsic parities. The intrinsic parity of boson pairs is $+1$, while the intrinsic parity of fermion pairs is -1.

A process, such as collision or decay, conserves parity if the differential cross-section of that process is the same as that of the space-inverted process. Up until 1956, it was generally assumed that parity is a good symmetry of nature. In that year, Lee and Yang suggested that parity might not be conserved in weak interactions [1]. Parity violation in the angular distributions of emitted electrons in the nuclear β decay of Co^{60} was observed the following year by C. S. Wu et al [2].

1.1.2 Charge-Conjugation (C)

The charge-conjugation operation C changes particles to their antiparticles. Particles that are their own antiparticles are eigenstates of the C operator. The eigenvalues of C are ± 1 because performing C twice on any state must give back the state itself. The photon has a C eigenvalue of -1 because it mediates the electromagnetic field A_μ, which changes sign when the signs of the charges change. States with n

photons have the C eigenvalue $(-1)^n$. A neutral pion, since it can decay into two photons, has a C eigenvalue of $+1$.

C violation in pion decay experiments of Garwin *et al.* [3] and Friedman and Telegdi [4] was observed soon after the observation of parity violation in β decay.

1.1.3 Charge-Conjugation Parity (CP)

These experiments establishing C violation in pion decay simultaneously violated parity. However, the decays are symmetric under the combined operations of C and P. Thus it was still believed that the combined symmetry CP should still be a good symmetry. This belief lasted until 1964, when Christenson, Cronin, Fitch, and Turlay [5] observed unambiguous CP violation in long-lived neutral kaons.

CP violation is a very important subject for a number of reasons. One of these stems from the supposed invariance of CPT (CP + time reversal conjugation). Under the minimal assumptions that nature is describable by local quantum field theories that exhibit Lorentz invariance and obey the spin-statistics theorem, the CPT theorem asserts that CPT must be a good symmetry for all interactions constructed in such theories. If CPT is not violated but CP is, then T violation is implied, meaning that there is an arrow of time governing even the most microscopic physical reactions. A second reason why CP violation was so interesting when first observed is that CP violation hints at the existence of a third family of quarks and leptons [6]. At the time CP violation was discovered, only two quarks and lepton families were known. A third reason for the interest in CP violation is the question of why there is more matter in the universe than antimatter. If we assume that matter and antimatter were present in equal amounts in the early universe, one of the requirements for the observed matter dominance is that there is CP violation [7]. The other conditions are baryon number non-conservation and thermodynamic disequilibrium.

1.2 CP Violation in the Neutral Kaon System

1.2.1 Phenomenology

The neutral kaon system may be described by several useful bases. The first linearly independent set of states spanning the space of the neutral kaon system is simply K^0 and $\overline{K^0}$. Since

$$|K^0\rangle = |\overline{s}d\rangle \tag{1.1}$$

and

$$|\overline{K^0}\rangle = |s\overline{d}\rangle, \tag{1.2}$$

K^0 and $\overline{K^0}$ are eigenstates with definite strangeness. However, they are not simultaneously eigenstates of CP, since

$$CP|K^0\rangle = |\overline{K^0}\rangle \tag{1.3}$$

and

$$CP|\overline{K^0}\rangle = |K^0\rangle, \tag{1.4}$$

where we have chosen the arbitrary phase to be zero[1].

From this discussion, it is obvious that the basis of CP eigenstates is

$$|K_1\rangle = \frac{1}{\sqrt{2}}(|K^0\rangle + |\overline{K^0}\rangle) \qquad (CP = +1) \tag{1.5}$$

and

$$|K_2\rangle = \frac{1}{\sqrt{2}}(|K^0\rangle - |\overline{K^0}\rangle) \qquad (CP = -1) \tag{1.6}$$

[1] $\phi = \pi$ is another common choice.

The basis sets of strange or CP eigenstates are useful when discussing the strong or electromagnetic interactions where strangeness and CP is conserved. However, because weak decays conserve neither strangeness nor CP, neither the basis of strange eigenstates (K^0 and $\overline{K^0}$) nor the basis of CP eigenstates (K_1 and K_2) have definite lifetimes for weak decay or definite mass.

The CP eigenvalues of the K_1 and K_2 are important to the lifetimes of these states. Since the two-pion final states ($\pi^0\pi^0$ and $\pi^+\pi^-$) have CP eigenvalue $+1$ and the three-pion final states ($\pi^0\pi^0\pi^0$ and $\pi^+\pi^-\pi^0$) have eigenvalue -1, if CP were always conserved, then K_1 would never decay to three pions and K_2 would never decay to two pions. Since the lower Q value of the three-pion final state restricts the overall amount of phase space available for K_2 decay, the K_2 has a longer lifetime than the K_1. If CP were a good symmetry, then the short-lived neutral kaon would correspond to the K_1 and the long-lived neutral kaon would be the K_2.

1.2.2 Observation of CP Violation

The belief that CP was a good symmetry was shattered by the discovery in 1964 by Christenson, Cronin, Fitch, and Turlay [5], which indicated that a long-lived particle with the same mass as the K_2 decayed to $\pi^+\pi^-$. At first, it was hypothesized to be a new particle of the same mass as the K_2, but with opposite CP, which could decay to $\pi^+\pi^-$ [8, 9]. Soon thereafter, interference in the $\pi^+\pi^-$ decays of the short- and long-lived states was observed [10], confirming that the long-lived neutral kaon decayed to $\pi^+\pi^-$.

Because of the small violation in CP symmetry observed in kaon decay, the CP eigenstates are not the same as the weak interaction eigenstates. However, unlike the maximal violation of parity and charge-conjugation individually, the violation in the combined CP symmetry is small. The weak eigenstates are taken to be small perturbations of the exact CP eigenstates K_1 and K_2, namely that

$$|K_S\rangle = \frac{1}{\sqrt{1+|\epsilon|^2}}(|K_1\rangle + \epsilon|K_2\rangle) \tag{1.7}$$

and

$$|K_L\rangle = \frac{1}{\sqrt{1+|\epsilon|^2}}(|K_2\rangle + \epsilon|K_1\rangle) \tag{1.8}$$

where K_S and K_L are the short- and long-lived neutral kaon, respectively. This is the model proposed by the superweak theory, which views the CP-violating decay as a direct consequence of the long-lived neutral particle being a mixture of CP eigenstates, with the part of the K_L decaying into two pions being the K_1 contamination. ϵ parametrizes the magnitude of this "indirect" CP violation, which arises from purely $\Delta S = 2$ interactions in the mass matrix.

In "direct" CP violation, a CP eigenstate of one type is allowed to decay into another CP eigenstate. Examples of direct CP violation are the decay of the K_2 into two pions or the K_1 into three pions. Direct CP violation is parametrized by ϵ'. By counting the number of different $K^0 \to \pi\pi$ decays, the ratio $\mathrm{Re}(\epsilon'/\epsilon)$ can be measured. The world average listed in the PDG [11] is $\mathrm{Re}(\epsilon'/\epsilon) = (18.0 \pm 4.0) \times 10^{-4}$, unambiguously confirming the existence of direct CP violation.

The decays $K_L \to \pi^0 l^+ l^-$ are promising avenues for the study of CP violation because even at the level of Standard Model predictions, the direct CP-violating components are expected to be comparable to or larger than indirect CP-violating or CP-conserving contributions.

1.3 Origin of CP Violation in the Standard Model

CP violation in the Standard Model is believed to arise through the charged current interaction, which is responsible for quark mixing. This interaction is defined to be

$$J_{cc} = (\overline{u} \;\; \overline{c} \;\; \overline{t}) \; M \begin{pmatrix} d \\ s \\ b \end{pmatrix} \tag{1.9}$$

where M is the Cabibbo-Kobayashi-Maskawa (CKM) matrix encapsulating the weak interaction charged current mixing angles between the three generations of quarks. The elements of M are

$$M = \begin{pmatrix} V_{ud} & V_{us} & V_{ub} \\ V_{cd} & V_{cs} & V_{cb} \\ V_{td} & V_{ts} & V_{tb} \end{pmatrix} \tag{1.10}$$

Because there are 9 constraints coming from the unitarity of M ($M^\dagger M = MM^\dagger = I$) and we are free to rephase 5 additional quark fields independently of the theory, the number of free parameters is reduced from 18 to 4. The standard parametrization [12] includes three real rotation angles and one non-trivial phase, which gives rise to CP violation in the Standard Model.

The popular Wolfenstein parametrization [13] uses $\lambda =$ sine of the Cabibbo angle, and expresses the other elements in terms of powers of λ:

$$M = \begin{pmatrix} 1-\lambda^2/2 & \lambda & A\lambda^3(\rho - i\eta) \\ -\lambda & 1-\lambda^2/2 & A\lambda^2 \\ A\lambda^3(1-\rho-i\eta) & -A\lambda^2 & 1 \end{pmatrix} + O(\lambda^4) \tag{1.11}$$

where A, ρ, and η are real numbers expected to be of order unity. If η is non-zero, then CP violation occurs within the Standard Model.

1.4 Contributions to $K_L \to \pi^0 e^+ e^-$

1.4.1 Overview of Standard Model Contributions

The decay $K_L \to \pi^0 e^+ e^-$ can occur through several different types of processes. The K_L is a mixture of the CP-even K_1 and the CP-odd K_2, and these states can pass through two intermediate states, which are CP eigenstates, to the $\pi^0 e^+ e^-$ final state, which does not have an intrinsic CP value. These intermediate CP eigenstates are $\pi^0\gamma^*$ (CP $= +1$) and $\pi^0\gamma^*\gamma^*$ (CP $= -1$). Since either K_1 or K_2 can proceed through these states, there are four different decay combinations for K_L. See Figure 1.1.

The process labeled "A" in the figure conserves CP, since it involves the K_1 going into $\pi^0\gamma^*$, both states with CP $= +1$. However, in the context of the K_L, which contains a small admixture of K_1, this is a indirect CP-violating process. "B" and "C" in the figure both represent direct CP violation. However, since process "C" is

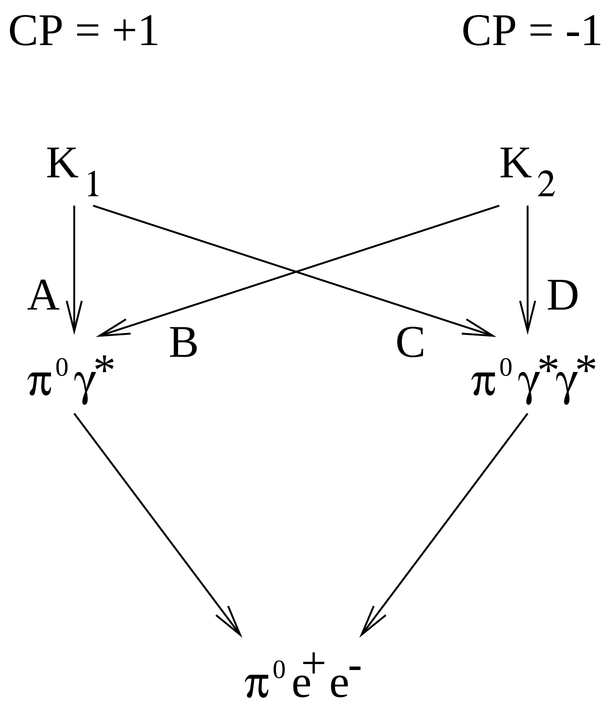

Figure 1.1: The different decay processes for $K_L \to \pi^0 e^+ e^-$. "A" represents an indirectly CP-violating process for K_L, "B" and "C" are directly CP-violating, and "D" is CP-conserving.

smaller than process "B" by a factor of ϵ in K_L, it is expected that "C" is negligible in comparison to "B" for $K_L \to \pi^0 e^+ e^-$. Finally, process "D" is CP-conserving, since both K_2 and $\pi^0\gamma^*\gamma^*$ have CP = -1.

The following sections will describe these CP-conserving, direct CP-violating, and indirect CP-violating processes in detail.

1.4.2 CP-Conserving

The CP-conserving contribution to $K_L \to \pi^0 e^+ e^-$ proceeds through the $\pi^0\gamma^*\gamma^*$ intermediate state, with the photons then converting into electrons, as shown in Figure 1.2. Diagram A in Figure 1.2 is suppressed in $\pi^0 e^+ e^-$ decay because the coupling of the photons to e^+e^- is reduced by a factor of m_e^2 due to the helicity-conserving nature of electromagnetic vertices. With extra (higher) powers of momentum in

Diagram B, this is no longer true, but now there is an angular momentum barrier. These considerations early on indicated that the CP-conserving contribution to $K_L \to \pi^0 e^+ e^-$ would be on the order of 10^{-14} [14], using a pure chiral perturbation theory calculation at $O(p^4)$. Other models, which became known as vector meson dominance (VMD) models, added in vector meson exchanges with particles such as ρ and ω, as in Figure 1.3. It was soon realized that VMD exchanges could be incorporated into the chiral perturbation theory calculation at higher orders in the chiral expansion [15]. The VMD effects could be accomodated in terms of one parameter, a_v. The dependence of the CP-conserving contribution to the branching ratio as a function of a_v can be found in [16, 17]. The latest measurement from the KTeV collaboration [18], at $a_v = -0.72 \pm 0.05 \pm 0.06$, indicates a value of 2.0×10^{-12} for BR$(K_L \to \pi^0 e^+ e^-\ )_{cons}$. However, the most recent result from NA48 [19] at $a_v = -0.46 \pm 0.03 \pm 0.03 \pm 0.02$ suggests a value closer to 0.5×10^{-12}.

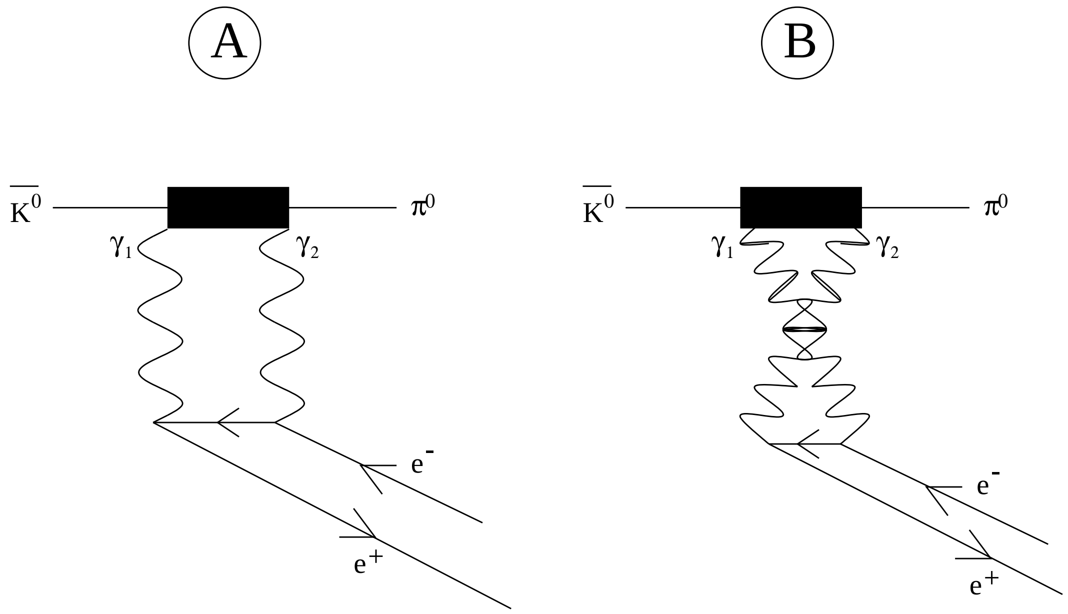

Figure 1.2: Two diagrams contributing to the CP-conserving process $K_L \to \pi^0\gamma\gamma \to \pi^0 e^+ e^-$ in Chiral Perturbation Theory.

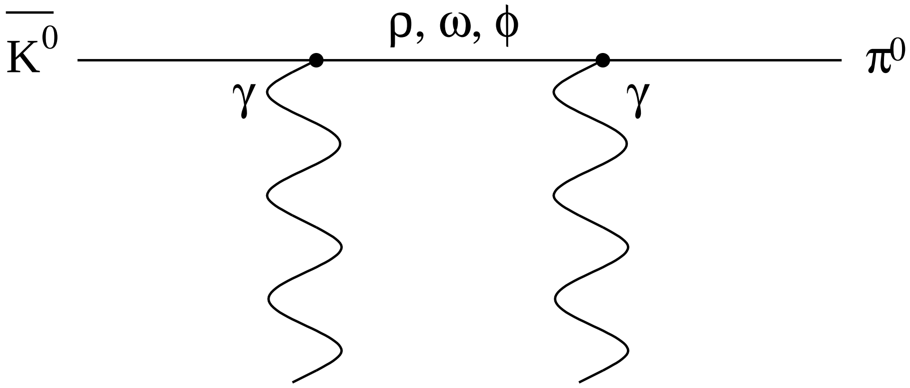

Figure 1.3: A vector dominance exchange contribution to the CP-conserving process $K_L \to \pi^0\gamma\gamma \to \pi^0 e^+ e^-$.

1.4.3 Direct CP-Violating

The direct CP-violating contribution to $K_L \to \pi^0 e^+ e^-$ proceeds through a $\pi^0\gamma^*$ intermediate state. The two dominant contributions to direct CP violation come from short-distance diagrams like the electroweak penguin in Figure 1.4 or the W box in Figure 1.5. In Figure 1.4, the s ($\overline{s}$) quark emits a W, turning into a u, c, or t ($\overline{u}, \overline{c}$, or $\overline{t}$) quark. This in turn recombines with the W to form a d ($\overline{d}$) quark. Because of the high mass of the top quark, the top quark diagrams dominates the amplitude. Since K_2 is the difference of K^0 and $\overline{K^0}$, the total amplitude involves terms involving $V_{td}V_{ts}^*$ and its complex conjugate. The result is an amplitude that is proportional to the CP-violating parameter η. The same effect occurs for the W-box diagram in Figure 1.5.

The expected rate for the direct CP-violating contribution is related to the CKM matrix element parameters by the following expression [16]

$$Br(K_L \to \pi^0 e^+ e^-)_{DIR} = 4.16(y_{7A}^2 + y_{7V}^2)(\mathrm{Im}\lambda_t)^2, \tag{1.12}$$

where

$$\mathrm{Im}\lambda_t = |V_{cb}|^2 |V_{us}| \eta. \tag{1.13}$$

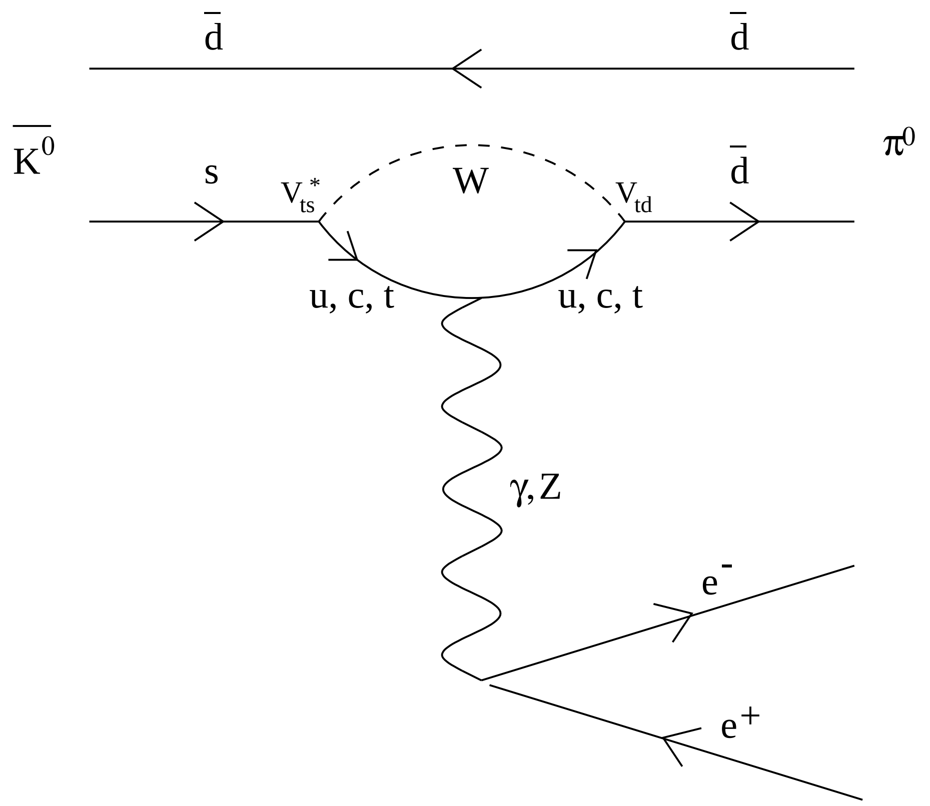

Figure 1.4: Directly CP-violating $K_L \to \pi^0 e^+ e^-$ electroweak decay penguin diagram.

The factor 4.16 comes from the branching ratio for the related decay $K^+ \to \pi^0 e^+ \nu$. y_{7A}^2 and y_{7V}^2 are QCD corrections that can be deduced from information in [16]. Using the central value of the top-quark mass, it can be found that $y_{7A}^2 = 5.415 \times 10^{-3}$ and $y_{7V}^2 = -5.339 \times 10^{-3}$. This leads to

$$Br(K_L \to \pi^0 e^+ e^-)_{DIR} = 2.41 \times 10^{-12} * \left(\frac{\text{Im } \lambda_t}{10^{-4}}\right)^2 \tag{1.14}$$

Using the best values for CKM elements, the direct CP-violating contribution is estimated [17] to be in the range (1.26 to 4.6) $\times 10^{-12}$ with the best estimate at

$$Br(K_L \to \pi^0 e^+ e^-)_{DIR} \approx 2.32 \times 10^{-12}. \tag{1.15}$$

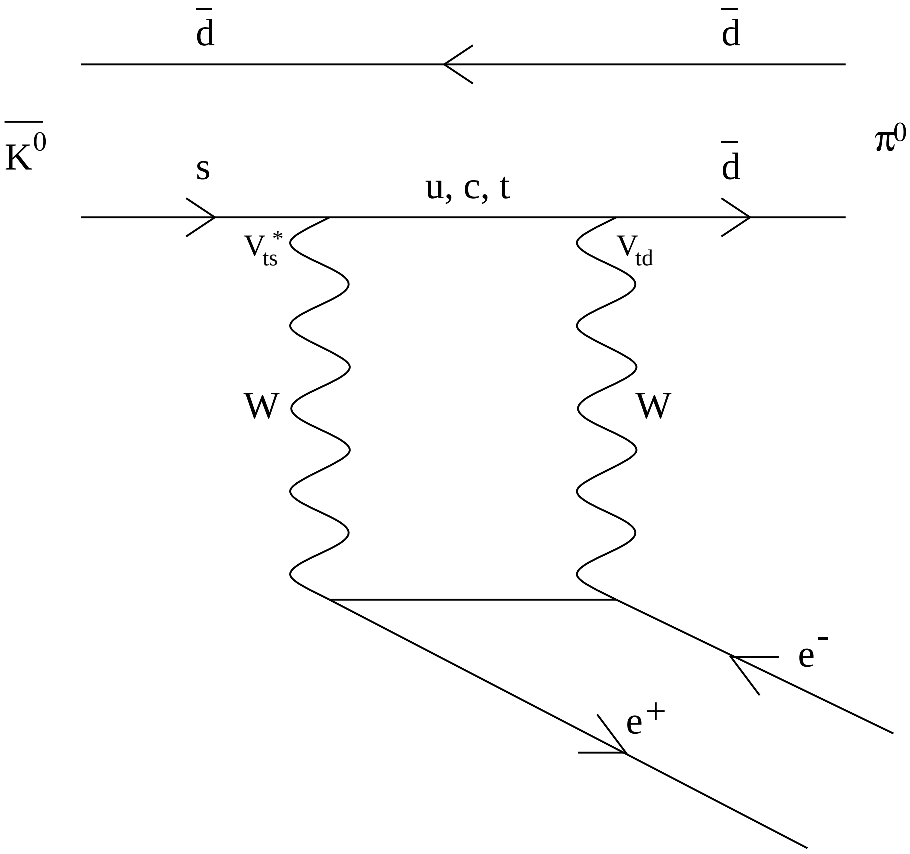

Figure 1.5: Directly CP-violating $K_L \to \pi^0 e^+ e^-$ W-box diagram.

1.4.4 Indirect CP-Violating

The indirectly CP-violating contribution to $K_L \to \pi^0 e^+ e^-$ comes from the fact that K_L contains a mixture of K_1. The indirect amplitude of $K_L \to \pi^0 e^+ e^-$ is simply

$$A(K_L \to \pi^0 e^+ e^-)_{ind} = \epsilon A(K_S \to \pi^0 e^+ e^-) \tag{1.16}$$

A measurement of $K_S \to \pi^0 e^+ e^-$ would immediately allow the indirect CP-violating part of $K_L \to \pi^0 e^+ e^-$ to be measured:

$$B(K_L \to \pi^0 e^+ e^-)_{ind} = |\epsilon|^2 (\frac{\tau_{K_L}}{\tau_{K_S}}) B(K_S \to \pi^0 e^+ e^-) \tag{1.17}$$

However, current measurements by NA48 [20] give BR($K_S \to \pi^0 e^+ e^-$) $< 1.4 \times 10^{-7}$

at the 90% C. L., which is about two orders of magnitude smaller than the expected level. The calculation of $A(K_S \to \pi^0 e^+ e^-)$ itself contains considerable theoretical uncertainty and presents a difficult challenge. Models relating $K_S \to \pi^0 e^+ e^-$ and $K^+ \to \pi^+ e^+ e^-$ have been constructed to predict that B $(K_L \to \pi^0 e^+ e^-)_{ind}$ is about 1.4×10^{-12} [21]. However, proper understanding of this component really requires the measurement of $K_S \to \pi^0 e^+ e^-$ [16].

1.4.5 Interference in Contributions

It was originally hoped that $K_L \to \pi^0 e^+ e^-$, when observed and measured, would provide evidence for direct CP violation. However, it has been demonstrated that it is also necessary to measure $K_S \to \pi^0 e^+ e^-$ and the interference of the direct and indirect CP-violating amplitudes [22]. Interference between the CP-violating and CP-conserving contributions in the decay distributions may cause the electrons and positrons to have an energy asymmetry [16, 17]. Direct CP violation could have a sizable impact on the magnitude of this energy asymmetry, to the extent that measurements of both BR($K_L \to \pi^0 e^+ e^-$) and the asymmetry can unambiguously indicate the existence of direct CP violation in the decay $K_L \to \pi^0 e^+ e^-$ [16].

1.4.6 Contributions from Non-Standard Model Processes

Enhancements to BR($K_L \to \pi^0 e^+ e^-$) are predicted in some non-Standard Model processes. Some models predict that $K_L \to \pi^0 e^+ e^-$ is dominated by an indirect CP-violating one-photon exchange process as large as 2.7×10^{-10} [23]. A supersymmetric extension of the Standard Model can enhance the $\overline{s}dZ$ effective vertex in rare kaon decays [24]. This effective vertex appears in the electroweak penguin of Figure 1.4 and is modeled as a W-quark loop. If $\epsilon^{'}/\epsilon$ is constrained to be less than 20×10^{-4}, BR($K_L \to \pi^0 e^+ e^-$) could be as large as 2.2×10^{-10} [25]. However, this upper bound is called into question in [26].

While it is not yet clear what limit is expected from non-Standard Model processes, a positive signal of $K_L \to \pi^0 e^+ e^-$ above several $\times 10^{-11}$ indicates physics beyond the Standard Model.

1.5 Previous Searches

All previous searches for $K_L \to \pi^0 e^+ e^-$ have found null results. Limits established by previous experimental searches for $K_L \to \pi^0 e^+ e^-$ are listed in Table 1.1. The best limit comes from data taken during the 1996-1997 run of the E799-II experiment at Fermilab.

90% C. L. Limit	Year	Reference
$< 2.3 \times 10^{-6}$	1980	[27]
$< 4.2 \times 10^{-8}$	1993	[28]
$< 5.5 \times 10^{-9}$	1990	[29]
$< 7.5 \times 10^{-9}$	1990	[30]
$< 4.3 \times 10^{-9}$	1993	[31]
$< 5.1 \times 10^{-10}$	2001	[32]

Table 1.1: Limits established by previous searches for $K_L \to \pi^0 e^+ e^-$.

1.6 Background Channels

The most significant backgrounds for the search for $K_L \to \pi^0 e^+ e^-$ are listed below. The main selection requirements used in the analysis to reject these backgrounds are discussed briefly.

- $K_L \to e^+ e^- \gamma\gamma$: The radiative K_L Dalitz decay has the same final-state particle content as $K_L \to \pi^0 e^+ e^-$. This is the single largest background to $K_L \to \pi^0 e^+ e^-$, and can only be suppressed with kinematic selection criteria, including a cut on $M_{\gamma\gamma}$ near the π^0 mass. However, $K_L \to e^+ e^- \gamma\gamma$ is an irreducible background in the sense that a finite amount of background will be predicted from this process no matter how tight the cut placed on $M_{\gamma\gamma}$. Fortunately, at BR ($K_L \to e^+ e^- \gamma\gamma$) = $(5.95 \pm 0.33) \times 10^{-7}$ [11], the decay $K_L \to e^+ e^- \gamma\gamma$ is intrinsically quite rare. The discussion in [33] discusses this important background in greater detail.

- $K_L \to e^+ e^- \gamma$: The K_L Dalitz decay can fake $K_L \to \pi^0 e^+ e^-$ if an extra photon is introduced, for example if the electron or positron radiates as it passes through the detector. If this happens, the angle between the electron or positron and the photon will typically be small, allowing this angle to be cut on. Another way an extra photon can appear is from accidental activity in the detector. When this happens, the invariant mass of the $e^+e^-\gamma\gamma$ tends to be much higher than the mass of the K^0, making a cut on $\mathrm{M}_{ee\gamma\gamma}$ effective in removing these events.

- $K_L \to \pi^0 e^+ e^- \gamma$: This channel can be a background if the photon is lost. Although the branching ratio for this decay is low at $(2.34 \pm 0.35_{stat} \pm 0.13_{sys}) \times 10^{-8}$ [34], it was initially thought that this decay would represent substantial background to $K_L \to \pi^0 e^+ e^-$ [35]. However, since a lost photon in $K_L \to \pi^0 e^+ e^- \gamma$ will cause $\mathrm{M}_{ee\gamma\gamma}$ to be much less than the mass of the K^0, a cut on $\mathrm{M}_{ee\gamma\gamma}$ renders this background negligible.

- $K_L \to \pi^\pm e^\mp \nu$: This semileptonic decay can become a background if the pion is mistaken for an electron and there are two extra photons coming from either accidental activity or from the electron radiating in the detector. It was the dominant background in E799-I [31], but E799-II has better π/e rejection coming from the improved calorimetry and TRDs and a cleaner beam. Kinematic cuts such as those to suppress $K_L \to e^+ e^- \gamma\gamma$ are also effective against $K_L \to \pi^\pm e^\mp \nu$ because of the large radiative component of this background.

- $K_L \to \pi^+ \pi^- \pi^0$: This decay can be a background when the pions fake electrons. When this happens, the reconstructed mass of the final-state system will be low, making this kinematic cut effective in suppressing this background. In addition, the charged pions are susceptible to strong π/e rejection coming from the calorimeter and the TRDs.

- $K_L \to \pi^0 \pi^0_D$: π^0_D denotes a pion which subsequently decays through the Dalitz channel. Although $K_L \to \pi^0 \pi^0$ is CP-violating, it occurs often enough to represent a potential background. One photon in this process must be lost, which causes the four-particle mass $\mathrm{M}_{ee\gamma\gamma}$ to be low. Also, because the electrons come from the Dalitz decay of the pion, M_{ee} will be strictly lower than the pion mass. Kinematic cuts on variables such as $\mathrm{M}_{ee\gamma\gamma}$ and M_{ee} suppress this background.

- $K_L \to \pi^0\pi^0\pi^0_D$: This CP-conserving mode has a much larger branching ratio than the CP-violating $K_L \to \pi^0\pi^0_D$. Also, because two of the pions may Dalitz decay, e^+e^- combinations with $\mathrm{M}_{ee} > \mathrm{M}_{\pi^0}$ occur. However, $\mathrm{M}_{ee\gamma\gamma}$ tends to be significantly lower than $\mathrm{M}_{\mathrm{K}^0}$ because only four of the seven or more decay products are reconstructed. Because so many final-state particles must be lost in order for $K_L \to \pi^0\pi^0\pi^0_D$ to be mistaken as $K_L \to \pi^0 e^+e^-$, kinematic cuts are very effective in suppressing this background.

CHAPTER 2
THE E799-II EXPERIMENTAL SETUP

KTeV is the name given to a collaboration of two different experiments: E799, which focuses on direct searches of CP-violating rare decays of the K_L, of which $K_L \to \pi^0 e^+ e^-$ is a flagship mode; and E832, which studies direct CP violation through measurement of ϵ'/ϵ in the $K \to 2\pi$ system. These two experiments use very similar hardware and software. The parts of the KTeV beamline and detector that are relevant to the $K_L \to \pi^0 e^+ e^-$ analysis are discussed in detail in this chapter.

The KTeV experimental facility is located along the neutrino-muon (NM) beamline at the Fermi National Accelerator Laboratory (Fermilab) in Batavia, Illinois. The data used in this analysis were recorded between Sept. 1999 and Jan. 2000.

2.1 The Beamline

A diagram of the KTeV secondary beam system appears in Figure 2.1. The beam of protons from the Tevatron strikes a BeO target located at the origin of the KTeV coordinate system by definition. The secondary beam consists mainly of neutral kaons but includes other charged and neutral particle species. The kaon beams are purified by a sequence of sweeping magnets and collimators. Detailed discussions of the design specifications of the KTeV secondary beam are to be found in [36, 37].

2.1.1 The KTeV Coordinate System

The BeO target is located at the origin of the KTeV coordinate system by definition. The $+z$ direction is defined as the downstream direction and is roughly north. The $+y$ axis is chosen to be the vertical up direction. The $+x$ axis is defined to be in

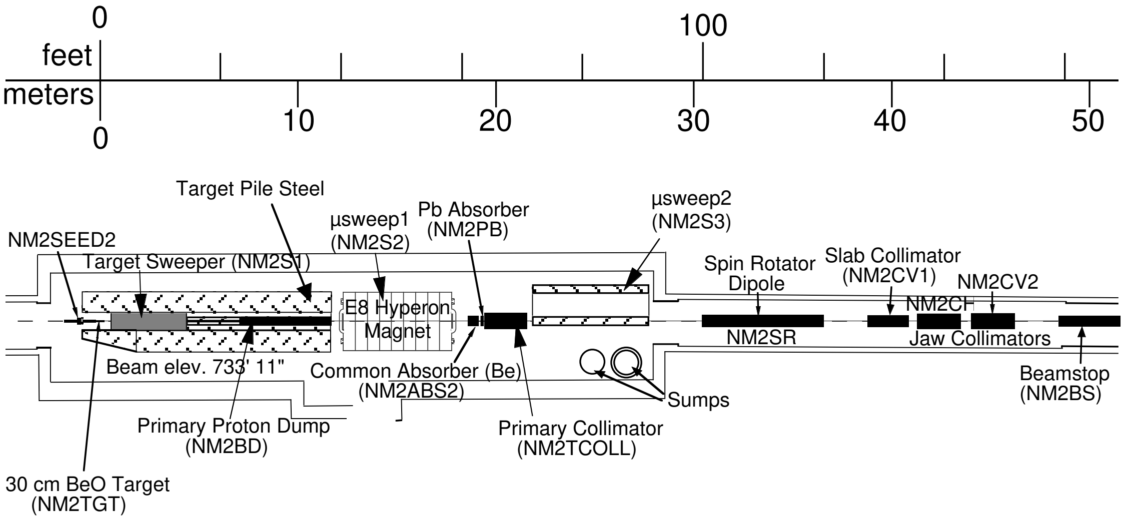

Figure 2.1: Secondary beam elements.

the direction that makes the coordinate system a right-handed system. It is roughly west or to the right if looking upstream.

2.1.2 The Primary Proton Beam

The process of generating the KTeV kaon beam starts with the Tevatron, which sends protons at energies of 800 GeV/c at the BeO fixed target. The protons are delivered by the Tevatron in a structured way. Protons arrive at the target in pulses 1-2 ns wide in a so-called “RF bucket” of 19 ns. These buckets occur at a frequency of 53 MHz for about 23 seconds, called a “spill”. Each spill is followed by an off-spill period lasting 37 seconds where no protons are delivered. The Tevatron provides up to 5 $\times 10^{12}$ protons every spill.

2.1.3 The Target

These protons are directed against a narrow BeO rod, measuring 3×3 mm across and 30 cm long. This length represents approximately 1.1 interaction lengths of BeO. The width of the primary proton beam spot is about 1 mm, and is tilted downward at an angle of 4.8 mrad with respect to the z-axis. This angle is chosen in order to avoid neutrons, which tend to be produced more forward than kaons, while optimizing the kaon to neutron ratio with high kaon flux. The primary proton beam is monitored by beam shape monitors used to help focus the beam onto the target. The first monitor, NM2SEED2, is located slightly upstream of the target. The target is cooled by a flow of nitrogen gas designed to maintain it at an operating temperature of about 125^o C.

2.1.4 The Sweeping Magnets, Absorbers, and Collimators

In order to purify the neutral kaon beam, charged and neutral particles must be removed from the beam. This is achieved by a series of sweepers. Absorbers are placed in the beam to increase the kaon content of the neutral beam, which consists mostly of neutrons and photons. Collimators are used to define the beam in the transverse direction.

"Sweeper" magnetic fields deflect charged particles out of the path of the beam. The "target sweeper" is the first sweeper magnet and is located about 2 m downstream of the target. This magnet deflects the remains of the primary proton beam towards a water-cooled copper beam dump. The other sweeping magnets are designed to remove muons from the kaon beam. The first of these is "μsweep1", which follows the primary target and removes muons from the beam. "μsweep2" removes particles created by interactions in the lead absorber and the primary collimator. The Final Sweeper magnet is located at z = 90 m, just behind the defining collimator. It removes charged particles from decays upstream of the collimator or produced in it.

The first absorber is the common absorber, located at $z = 18.5$ m and consisting of 20 inches of beryllium. More neutrons than kaons are removed because of different interaction cross-sections in beryllium. Just downstream is the lead absorber, a layer of lead 3 inches thick at $z = 19$ m. Photons are converted into e^+e^- pairs, which are absorbed.

The collimation system defines the beam with increasing precision. The primary collimator at $z = 20$ m is made of brass and has two tapered rectangular cylinders cut through it to create and roughly shape the two kaon beams[1]. The centers of the two beams are separated by 1.6 mrad with respect to the target. The next collimator is the slab collimator at $z = 38$ m. It is a single wedge of stainless steel and sits between the two beams. It prevents particles from crossing one beam into the other. The last element defining the beams is the defining collimator. It is located at $z = 85$ m and has a similar geometry to the primary collimator but is made of iron. It defines the beam shape and sets the beam divergence at 0.8 mrad. An illustration of the collimation system appears as Figure 2.2.

There are several other elements in this region. The spin rotator magnet is important to some hyperon analyses but has no effect on this analysis because kaons are spinless. The jaw collimators are also not significant to the analysis. The beam stops at $z = 50$ m are a pair of iron blocks which are required to be rolled

[1]KTeV was designed with two kaon beams to accommodate the study by E832 of ϵ'/ϵ, but the split beam has little effect on E799-II's rare decay searches.

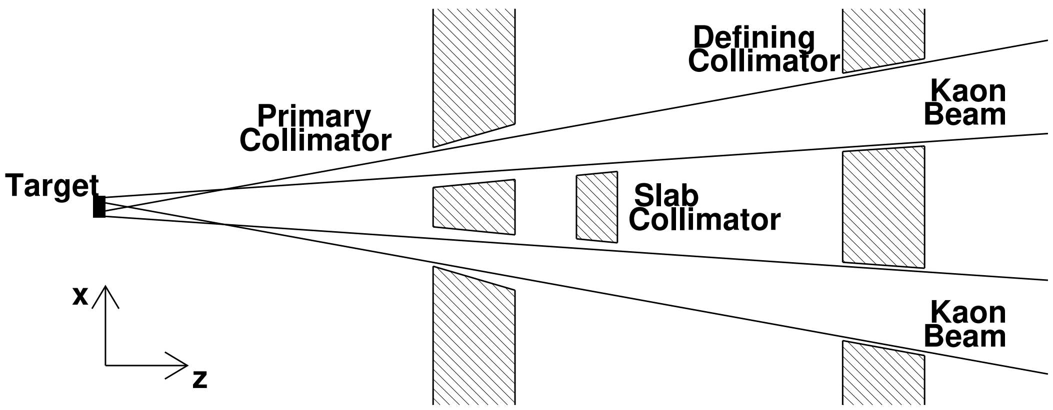

Figure 2.2: Schematic illustration of the KTeV collimator system. Figure is not to scale. Sweepers, absorbers, and other elements of the larger secondary beam definition system are not shown.

into place before lab personnel could be granted access to the detector hall to make quick repairs on the equipment.

2.1.5 Beam Characteristics

At this point, the beam contains mostly neutrons and kaons at a ratio of 1.3 to 1. Fortunately, the long lifetime of the neutrons prevents them from decaying in the detector and they usually show up as neutral accidental activity. A small amount of other neutral particles are also present in the beam. Among them are photons, neutral hadrons, and small amounts of cascades, and lambdas. These neutral particles are suppressed by several orders of magnitude relative to kaons and neutrons. The K_S from the target which decay in the decay region typically have very high momentum, with values around 200 GeV/c.

2.2 The Detector

A diagram showing the KTeV detector appears as Figure 2.3. The main components are a charged-particle spectrometer, followed by an electromagnetic calorimeter. These are triggered by a pair of scintillator hodoscopes. The transition radiation detectors (TRDs) provide electron identification and pion discrimination and the photon vetoes define the region of acceptance.

2.2.1 The Decay Region

The 65 m long vacuum decay region follows the defining collimator and the final sweeper. This evacuated area begins at the upstream end at $z = 93.0$ m and extends downstream to $z = 158.9$ m. It starts as a 45.73 cm diameter vacuum pipe and grows progressively larger downstream to a size of 243.84 cm in diameter. The pressure inside the tank is maintained at 10^{-6} torr. A strong but thin mylar-kevlar window is placed at the downstream end of the decay region to prevent air from rushing in. This window is 0.0015 radiation lengths thick.

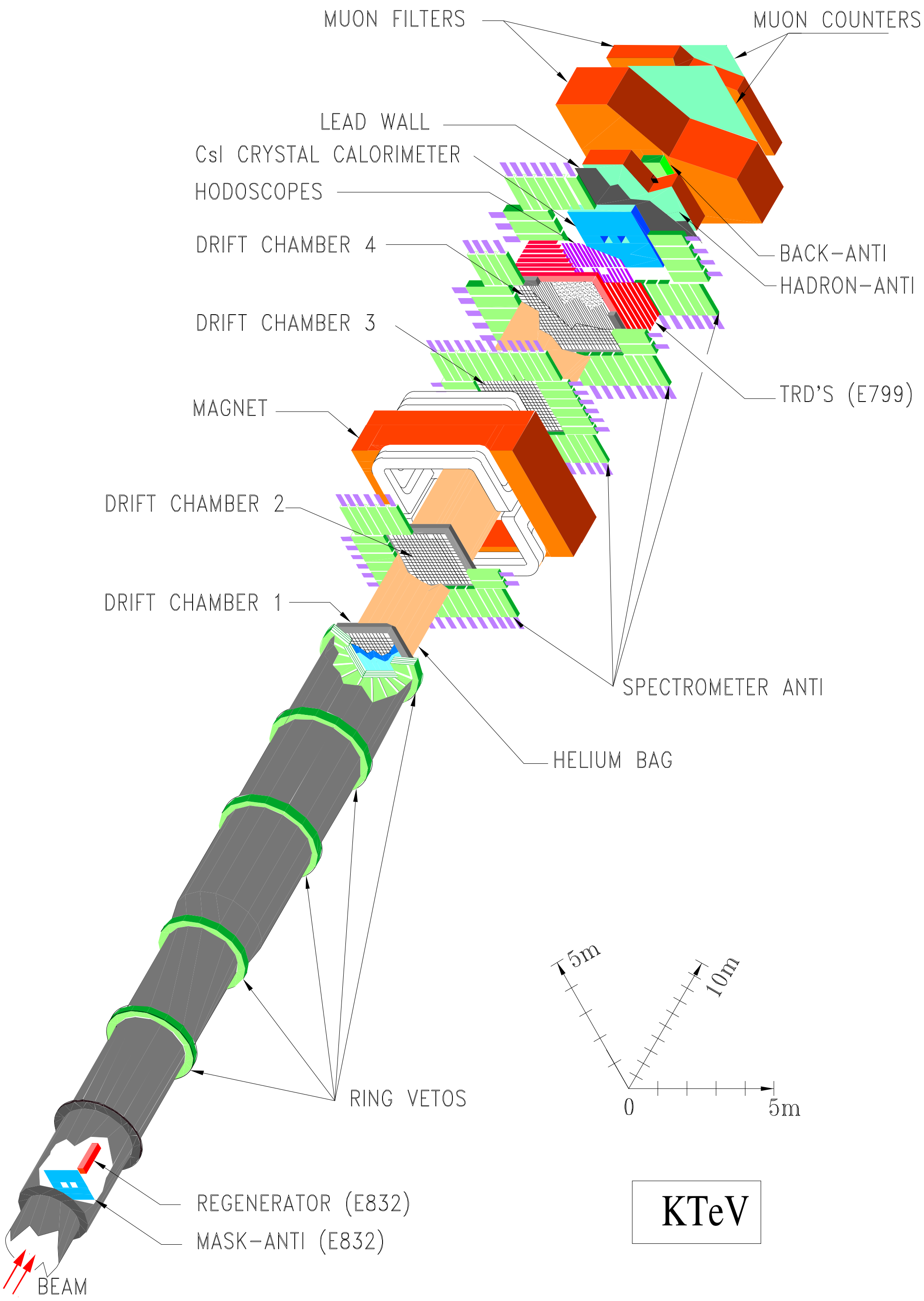

Figure 2.3: The KTeV detector.

2.2.2 The Spectrometer

The spectrometer is designed to find the trajectories of charged particles and to measure the momentum of each track. By extrapolating the particle trajectories upstream, the position of the decay vertex can be determined. The spectrometer system includes four drift chambers with an analysis magnet located between the second and third chamber.

2.2.2.1 The Drift Chambers

The wires in the four drift chambers (DCs) come in two types: sense wires for the detection of charged particles and larger field-shaping wires arranged in a hexagonal cell pattern around the sense wires. See Figure 2.4. The sense wires are 1 mil gold-plated tungsten and the field wires are 4 mil gold-plated aluminum to reduce multiple scattering from the wires.

Each DC is made up of two pairs (or "views") of planes. The first view has its sense wires oriented along the y direction ("x-view") in the upstream section of each chamber and the second is oriented along the x direction ("y-view"). The two planes in each view are offset by one half-cell (6.35 mm) to permit an unambiguous hit position measurement.

The position measurement begins when a charged particle ionizes atoms in the argon/ethane gas mixture. The ionization electrons are accelerated by the electric field toward the anode sense wires. As the electrons increasingly gain energy, they quickly ionize more and more gas atoms, forming an avalanche. A detectable current is registered when this electron avalanche reaches the sense wire. The track of a particle as it passes through the drift chamber can be reconstructed from knowledge of the position of the sense wires and the time when the current arrives. Hits from good tracks should reconstruct to a Sum-of-Distance (SOD) equal to the sense wire spacing of 6.35 mm.

The drift chambers contain a mixture of equal parts argon and ethane, with 0.5% to 1.0% isopropyl alcohol by volume added to absorb damaging UV light produced during gas amplification, thus slowing the aging of the chamber.

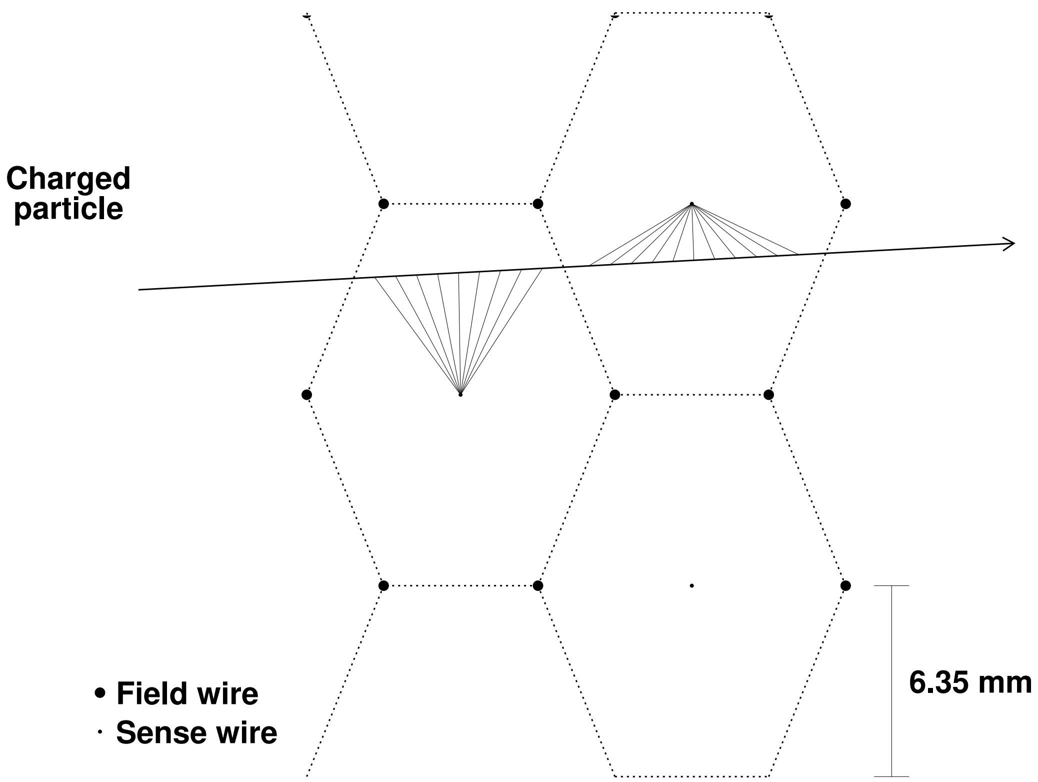

Figure 2.4: The hexagonal drift cell geometry. The trajectory of a typical charged particle through the drift chamber is shown. The drift paths of the ionization electrons toward the sense wires are represented by the thin lines.

Plastic bags filled with helium are placed in the spaces between the drift chambers in order to reduce multiple scattering of charged tracks in the spectrometer.

2.2.2.2 The Analysis Magnet

The KTeV spectrometer magnet, located at $z = 170$ m, is a large dipole magnet producing a vertical field of $\sim$2000 gauss over a gap of 2 m. The field produced is very uniform over the face of the magnet, with variations under 0.25%. The magnitude of the momentum kick in the x-view is given by the integral

$$\Delta p_{magnet} = \frac{1}{c} \int B dz \tag{2.1}$$

During the 1999-2000 runs of E799-II, a charged particle crossing this field received a Δp_{magnet} of approximately 150 MeV/c.

The field orientation is reversed periodically in order to remove systematic biases relating to magnet polarity.

2.2.3 The Transition Radiation Detectors

The transition radiation detectors (TRDs) are designed to discriminate between electrons and pions. They are significant to rejection of background involving charged pions. Transition radiation is emitted by particles passing between media with differing indices of refraction, and the amount of energy radiated is inversely proportional to the mass of the particles. The profile of the energy deposited in the TRD is different for pions and electrons. For the former, the energy profile will be a single ionization peak while the profile for the latter tends to be broader. By looking at the energy profiles, electrons can be distinguished from pions, thus allowing for efficient π/e discrimination. Further details about the TRDs are available in [38].

2.2.4 The Trigger Hodoscopes

Two back-to-back banks of scintillator counters provide first-level trigger information for charged-particle triggers. This is because trigger signals from the drift chamber are delayed by a maximum of $\sim$2000 ns since drift times for electrons in the drift chambers could take up to that long. These counters, called V and V$'$, are located at $z = 183.90$ m and 183.95 m, respectively, just in front of the calorimeter. The geometry of the VV$'$ counters is shown in Figure 2.5. Each plane is 1.0 cm thick and consists of an array of scintillator paddles aligned in the vertical direction, allowing for a quick determination of track multiplicity, since the analysis magnet deflects tracks in the x direction and not in the y. The paddles are not overlapping in an individual plane, but the two planes are offset by one-half counter, reducing the possibility of particles slipping through the VV$'$ banks undetected. Due to worries of radiation damage to the calorimeter caused by particles produced in interactions of the beam with the counters [39], the trigger hodoscopes have beam holes cut out.

2.2.5 The Calorimeter

The crown jewel of KTeV is the CsI calorimeter. At the time KTeV was being designed, lead-glass was the customary material used in the calorimetry. It had been used in previous kaon fixed-target experiments at Fermilab (E731, E773, and E779-I). CsI crystals were found to be a great substitute material with excellent energy and position resolution, quick signals and good radiation hardness.

The purpose of the CsI calorimeter is to meaure the location and magnitude of the energy deposited in it by kaon decay products interacting electromagnetically within the crystal. The calorimeter is the only way to detect photons in the detector.

The calorimeter consists of 3100 blocks of pure CsI. Each block is 50 cm long, which corresponds to 27 radiation lengths or 1.4 hadronic lengths of material. There are 868 "large" crystals measuring 5.0 cm $\times$ 5.0 cm across, and 2,322 "small" crystals measuring 2.5 cm $\times$ 2.5 cm across. The crystals are arranged in a square array 1.9

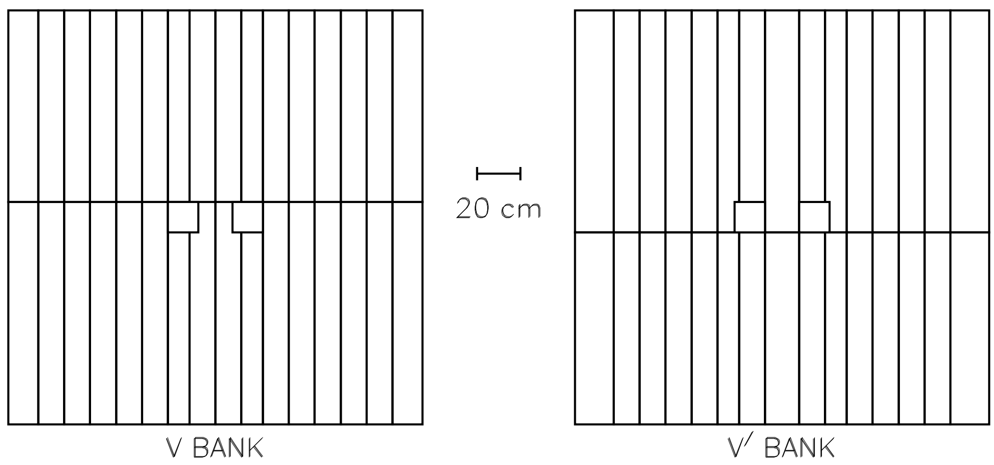

Figure 2.5: The layout of the V and V′ trigger hodoscope counters.

m wide on a side with two 15 cm square holes for the neutral beams. The small crystals at placed at the center, where particle interaction with the CsI is maximal, and the large crystals are arranged around them. The CsI array is illustrated in Figure 2.6.

Each crystal is separately wrapped with reflective and dark materials to achieve light-tightness and uniform light transmission over its length. The total light output is more than 10 photo-electrons per MeV deposited per crystal [40]. The energy deposited by particles that interact electromagnetically, such as photons and electrons, is almost entirely contained within the calorimeter because the CsI is 27 radiation lengths long. However, showers due to hadronic backgrounds such as $\pi^{\pm}$ are not fully contained by the calorimeter because it is only 1.4 hadronic interaction lengths long.

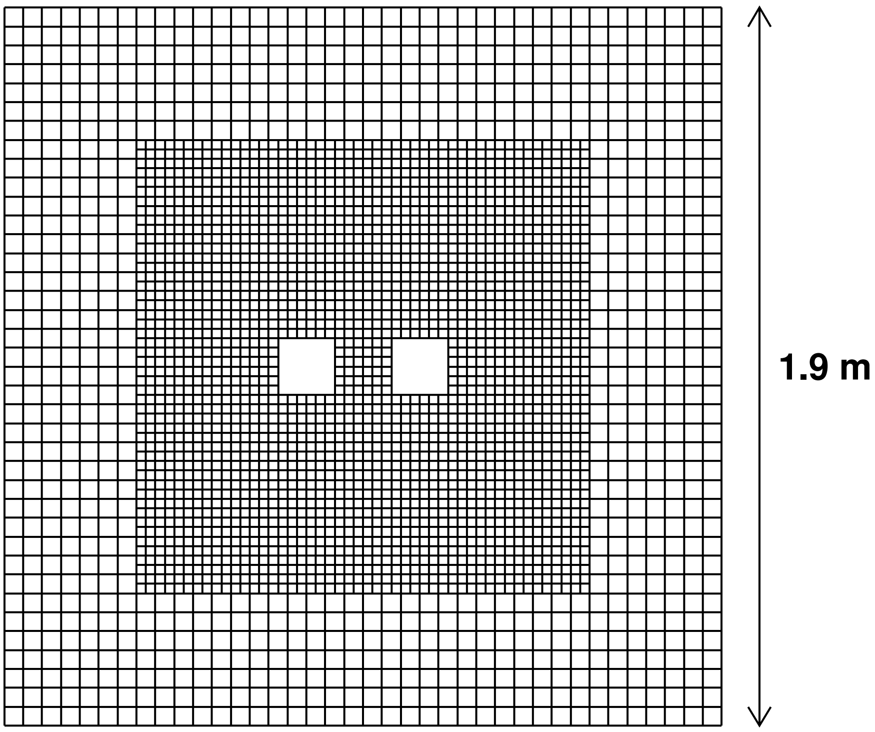

Figure 2.6: The layout of the CsI calorimeter. It is 1.9 m on each side and 0.5 m deep. The centers of the two beam holes are at $x = \pm 15$ cm and $y = 0$.

By looking at the ratio E/p, with E the energy measured in the calorimeter and p the momentum as determined by the spectrometer, electrons may be effectively distinguished from charged pions.

2.2.6 The Veto Counters

The veto detectors in the KTeV experiment are designed to define a hermetic fiducial region. They complement the spectrometer and calorimeter by detecting decay products which are not observed by them because of the limited physical extent of these detectors. Many K_L particle decays can fake the signature of a $K_L \to \pi^0 e^+ e^-$ decay if one or more particles are missed, for example when $K_L \to \pi^0 \pi^0_D$ with a missing photon. The veto counters prevent situations in which particles are missed from occurring. The location of these detectors can be seen in Figure 2.3.

2.2.6.1 The Ring Photon Vetoes

The Ring Counters (RCs) veto events where a decay product leaves the fiducial decay volume of the detector. These counters are circular on the outside and are placed flush with the vacuum vessel walls. The inner aperture is square. The RCs are made of 24 alternating layers of lead and scintillator, equivalent to 16 radiation lengths. The detectors are segmented into 12 azimuthal sectors and are overlapped to prevent particles from slipping through cracks. Fibers read out the scintillation light, which are fed to PMTs. The signals from the PMTs are passed through a discriminator to filter out noise. The PMT signals are sent to the trigger system and are digitized by ADC modules.

2.2.6.2 The Spectrometer Antis

The three Spectrometer Antis (SAs) define the apertures around drift chambers 2, 3, and 4, and were located just upstream of these chambers. The SAs have 16 radiation lengths of Pb, arranged in 32 layers of 0.5 radiation length Pb and scintillator. They are capable of detecting stray photons down to energies of 100 MeV [41, 42]. Light is gathered and sent out of the SAs by glass fibers to phototubes. Phototube signals are digitized by ADCs and sent to the Level 1 trigger system, which could then make a quick decision to veto an event whose decay products are detected to be escaping the detector.

2.2.6.3 The Cesium Iodide Anti and the Collar Anti

The Cesium Iodide Anti (CIA) and the Collar Anti (CA) are the two veto counters around the outer and inner edges of the calorimeter, respectively. The CIA is constructed similarly to the SAs and sits just upstream of the calorimeter. It provides signals to the Level 1 trigger to veto events that would be mis-reconstructed due to energy leakage out of the side of the calorimeter. It covers half of the cystals calorimeter's perimeter.

The CA is located just upstream of the CsI calorimeter and defines its inner aperture. It detects photons hitting the calorimeter near the edge of the beam holes. Events with such photons are rejected, because much of the shower energy of the photon can be lost down the beam holes, making the energy and the position difficult to determine. The CA includes two identical square annular detectors and overlaps the crystals immediately adjacent to the beam holes by 1.5 cm. It is made up of three layers of tungsten and scintillator [43], read out by fibers going to phototubes mounted at the edge of the calorimeter. The CA is shown in Figure 2.7.

2.2.6.4 The Hadron Anti

A 15 cm thick Pb wall is located just downstream of the calorimeter. It is designed to increase the probability that hadrons and pions passing the calorimeter will shower while absorbing all the leakage from electromagnetic events. In this way, events with a $\pi^{\pm}$ (such as $K_L \to \pi^{\pm} e^{\mp} \nu$) could be vetoed at the trigger level by the Hadron Anti (HA) [44], while maintaining high efficiency for photons and electrons. The HA is located at the downstream face of the Pb wall, and is composed of 28 scintillator paddles, half located above and half below the neutral beams. The Pb wall and HA have rectangular holes to allow the beams to pass through. These measure 60 cm $\times$ 30 cm in the wall and 64 cm $\times$ 34 cm in the HA.

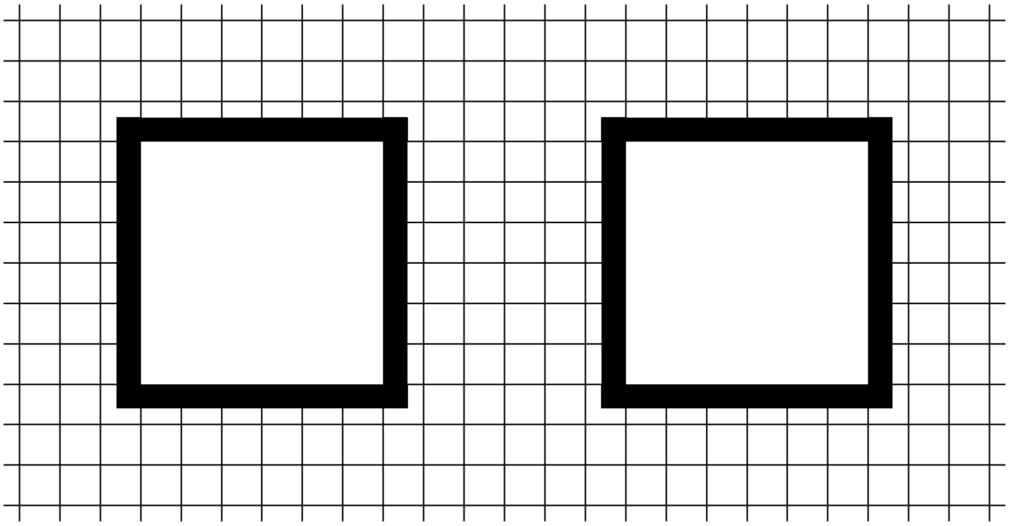

Figure 2.7: Illustration of the collar anti (CA) counters. The CA are the two black annular regions surrounding the beam holes of the calorimeter, which is depicted here by the grid showing the edges of the 2.5 cm × 2.5 cm square CsI crystals.

CHAPTER 3
EVENT SELECTION

Event selection includes an online trigger and offline data reduction. The trigger system includes two hardware stages, Levels 1 and 2, and one software stage, Level 3. Offline data reduction consists of a data split to separate data according to general physics topics and a data crunch to roughly identify and remove uninteresting events.

3.1 The Trigger System

The rate of K_L decays in the KTeV detector is very high. K_L decays in the fiducial volume of the detector occur at the rate of about 1 MHz. It is impossible and undesirable to record every K_L decay. Most decays proceed to final states that are not useful for calibration or interesting to study. The purpose of the trigger system is to decide which are the most interesting events for the data acquisition system (DAQ) to read out of the detector and record to tape.

The trigger system consists of three successive stages, Levels 1, 2, and 3, which make more and more stringent requirements on the candidate events to be read out. The trigger effectively reduces the rate from 1 MHz to 60,000 events per spill. The Level 1 and Level 2 trigger systems are implemented in hardware using quick electronic signals directly from the detector. The Level 3 software trigger involves a full reconstruction of events.

Further details on the design, construction, and performance of the trigger may be found in [45–50].

3.1.1 Level 1

The deadtimeless Level 1 trigger uses the fastest Boolean sources in simple logical combinations to make decisions. These signals come from the drift chambers and the phototubes, including the Ring Counters, Spectrometer Antis, Cesium Iodide Anti, Collar Anti, the trigger hodoscopes V and V$'$, the Hadron Anti hodoscope, and energy information from the CsI calorimeter. These signals are shaped with commercial electronics, and timed so that they arrive at the Level 1 trigger decision center at the same time.

The trigger used in this analysis is the 2E-NCLUS trigger, so called because two electron tracks and $N \geq 4$ clusters are required. At Level 1, the 2E-NCLUS trigger logic is succinctly expressed as

$$\mathrm{L1} = \mathrm{2V} \cdot \mathrm{ET\_THR3} \cdot \mathrm{DC12} \cdot \mathrm{PHVBAR} \cdot \overline{\mathrm{HA}} \cdot \overline{\mathrm{CA}}. \tag{3.1}$$

In plain English, this requires all of the following to be true:

- 2V : There must be at least 2 hits in V and 1 hit in V$'$ or vice-versa. This is tantamount to allowing one hit to be missing due to inefficiencies or cracks between the V and V$'$ paddles.
- ET_THR3 : The total energy, ETOT, in the event must be greater than 25 GeV.
- DC12 : For triggering, groups of 16 wires in the two overlapping planes of a drift chamber are grouped together into a drift chamber "paddle". This trigger requires that at least one such paddle in DC1 or DC2 must be hit.
- PHVBAR : There is no counter registering energy greater than 500 MeV in the RCs, SAs, or CIA.
- $\overline{\mathrm{HA}}$: The HA sum did not fire above 2.5 MIPS.
- $\overline{\mathrm{CA}}$: No CA counter registered above 14 GeV.

In the analysis, the VV$'$, ETOT, and photon vetoes are explicitly verified.

3.1.2 Level 2

The Level 2 trigger uses custom electronics to perform pattern matching on fast detector signals at a more sophisticated level than Level 1. During Level 2 processing, the Level 1 trigger is inactive.

The Level 2 trigger system includes subsystems which count hits in the DCs, find in-time pairs in the DCs, and count the number of clusters in the CsI calorimeter.

Hit counting in the DCs is done in order to reject events without enough hits to reconstruct the required number of tracks specified by the trigger. The hit counting logic is implemented on custom VME boards called "Kumquat" modules. The Kumquats take fast signals from each wire and count the number of hits in each of the eight DC views (x- and y-view in the four DCs).

The Kumquats cannot tell if the hits it counts are in-time or not. In order to make this determination, "Banana" modules must be used. These modules latch DC hits and measure the time of each hit with a 625 MHz TDC. Classification of isolated hits, in-time pairs, and out-of-time pairs is performed by consulting memory look-up maps. The processing time of the Bananas and Kumquats is 800 ns.

The number of clusters in the CsI calorimeter is counted by the Hardware Cluster Counter (HCC) [51]. The HCC receives 3,100 discriminated signals from the calorimeter phototubes. These discriminators are tuned to a threshold of 1 GeV. The HCC provides a three-bit cluster count and an overflow bit to Level 2, allowing triggering on any number of clusters up to 7, and on greater than 8 clusters. The processing time of the HCC is 2.5 μs, making it the slowest Level 2 subsystem.

The Level 2 trigger requirement for 2E-NCLUS is

$$\mathrm{L2} = \mathrm{2HCY\_LOOSE} \cdot \mathrm{1HC2X} \cdot \mathrm{HCC\_GE4}. \tag{3.2}$$

This means that the following must occur:

- 2HCY_LOOSE : There are at least two hits in each y-view, but at most one missing hit in either the DC1 or DC2 y-view (not both) is allowed.

- 1HC2X : At least one acceptable in-time hit pair is found by a DC2 x-view Banana.

- HCC_GE4 : At least four HCC clusters are found.

3.1.3 Level 3

If Level 2 decides to pass an event, all detector data is immediately read out to four SGI Challenge computers. The Level 3 trigger makes a full but simplified reconstruction of events using rough "online" calibration constants that may not be as accurate as the constants determined later offline. However, the accuracy of these online calibration constants is sufficient for purpose of making the loose cuts required in the Level 3 decision.

Level 3 examines events satisfying the 2E-NCLUS trigger at Level 2 to see if they pass one of various trigger tags corresponding to specific physics criteria. For this analysis, the relevant Level 3 tag is the "2E-NCLUS" tag. For an event to be tagged as 2E-NCLUS, the following requirements must be met:

- There must be at least two oppositely-charged tracks which can be reconstructed using loose tracking cuts.
- These tracks must come from a single decay vertex.
- There must be at least two tracks with $E/p > 0.75$, in order to identify electron candidates.
- There must be four or more clusters in the calorimeter.
- Both tracks must point towards clusters in the CsI.

An event must satisfy the full set of requirements for at least one of the tags in order for it to pass Level 3 and be recorded. A small amount of prescaled random accepts are also written out for use in studying the efficiency of the Level 3 trigger.

3.2 Data Reduction

3.2.1 The 1999-2000 E799-II Run

The E799-II experiment took data in two stages: the 1997 Run spanned the Jan. 1997 to Sept. 1997 time period[1], and the 1999-2000 Run extended from Sept. 1999 to Jan. 2000. Since the data in the 1997 Run have already been extensively searched for $K_L \to \pi^0 e^+ e^-$ [32, 38, 45, 52], this analysis uses the data collected in the 1999-2000 Run.

Each uninterrupted period of data collection in the larger E799-II Run is also called a run. A single run typically lasts for about eight hours. This is about the length of time it takes for output tapes to fill during normal running conditions and beam intensity. The 1999-2000 period of data-taking span the runs 14625 and 15548. A total of 226 runs are used within this range.

3.2.2 The Data Split

Although the trigger system makes efficient decisions about which events to write to tape, there is still an enormous amount of raw data recorded. The purpose of the data split is to separate the raw data by trigger type and Level 3 tags into smaller sets of output tapes. The tape split of the 1999-2000 data results in 133 DLTs of data in the 2E-NCLUS stream.

3.2.3 The Data Crunch

Following the data split, additional tighter cuts relative to the Level 3 selection criteria are imposed in order to reduce the size of the data set further. Because this crunch stage performs a more sophisticated analysis on the events, it requires use of the more accurate set of calibration constants determined after offline analysis.

The 2E-NCLUS identified and tagged ten separate physics modes within the 2E-NCLUS triggers. Table 3.1 summarizes the different filter tags and physics modes.

---

[1] With a three-month hiatus between April and June 1997.

Filter Tag	Cuts	Tagged %	Physics
EEGG	L3*$\cdot$ T3FVTX $\cdot$ EOP* $\cdot$ (NHCLUS = 4) $\cdot$ (Vtx $\subset$ CsIhole $\pm$ 5 cm) $\cdot$ ($\mathrm{P_T^2} < 0.004$ (GeV/c)^2)	3.54%	$\pi^0 e^+ e^-$ $e^+ e^- \gamma\gamma$
EEGGG	L3*$\cdot$ T3FVTX $\cdot$ EOP* $\cdot$ (NHCLUS = 5) $\cdot$ (Vtx $\subset$ CsIhole $\pm$ 5 cm) $\cdot$ (M > 0.380 GeV)	3.70%	$\pi^0 e^+ e^- \gamma$ $\pi^0\pi^0$ ($\pi^0 \to ee\gamma$) $\pi^0\gamma\gamma$ ($\pi^0 \to ee\gamma$)
L3RAND	L3 Random Accept Tag	0.18%	Systematic Studies
PI0TEE	L3*$\cdot$ (NCLUS $\geq$ 6) $\cdot$ EOP*$\cdot$ ($\mathrm{M_{ee}} \geq 0.07$ GeV)	4.42%	$\pi^0 \to e^+ e^-$
3T6SC	L3*$\cdot$ (NCLUS $\geq$ 6) $\cdot$ EOP*$\cdot$ (NTRK $\geq$ 3) $\cdot$ EOP3*	0.89%	$\pi^0 \to e^+ e^-$ background
4TRACK	L3*$\cdot$ EOP* $\cdot$ T3FVTX4	4.45%	$e^+ e^- e^+ e^-$ $\pi^0 \to e^+ e^- e^+ e^-$
2T8C	L3*$\cdot$ EOP* $\cdot$ T3FVTX $\cdot$ $\overline{\mathrm{T3FVTX4}}$ $\cdot$ (NHCLUS $\geq$ 8)	1.37%	$\pi^0\pi^0\pi^0$ ($\pi^0 \to ee\gamma\gamma$) $\pi^0\pi^0\pi^0\gamma$ ($\pi^0 \to ee\gamma$)
2PI0EE	L3*$\cdot$ EOP* $\cdot$ T3FVTX $\cdot$ (NHCLUS = 6) $\cdot$ ($\mathrm{P_T^2} < 0.005$ (GeV/c)^2) $\cdot$ (M > 0.44 GeV)	5.92%	$\pi^0\pi^0 e^+ e^-$ $\pi^0\pi^0\gamma$ ($\pi^0 \to ee\gamma\gamma$)
3T7C	L3*$\cdot$ EOP* $\cdot$ T3FVTX $\cdot$ (NTRK = 3) $\cdot$ (NHCLUS $\geq$ 7)	0.64%	Background to $\pi^0\pi^0\pi^0$ ($2 \times \pi^0 \to ee\gamma$) with a missing track
3PI0D	L3*$\cdot$ EOP* $\cdot$ T3FVTX $\cdot$ (NHCLUS = 7)	25.74%	$\pi^0\pi^0\pi^0$ ($\pi^0 \to ee\gamma$)

Table 3.1: Listing of crunch filter tags and associated physics modes.

The cuts listed in abbreviation in the table mean the following:

- L3* : The Level 3 trigger tagged the event as either 2E-NCLUS or 3PI0DAL.
- NCLUS : The number of software clusters found.
- NHCLUS : The number of clusters found in the HCC.

- EOP* : Two or more tracks have $E/p \geq 0.9$.
- EOP3* : Three or more tracks have $E/p \geq 0.9$.
- NTRK : Number of tracks.
- T3FVTX : A two-track vertex can be reconstructed.
- T3FVTX4 : A four-track vertex can be reconstructed.
- $\mathrm{P_T^2}$: The square of the transverse momentum.
- (Vtx $\subset$ CsIhole $\pm$ 5 cm) : The line drawn from the target passing through the reconstructed vertex position intersects the face of the calorimeter at a point within 5 cm of a beam hole.

More detailed information about the 2E-NCLUS crunch can be found in [53].

The 2E-NCLUS crunch output is written onto 22 DLT tapes. Normalization mode $K_L \to \pi^0\pi^0_D$ data used in this analysis is taken from the NQND04, NQND05, and NQND06 tapes of the 2E-NCLUS crunch. These tapes contain a total of 9.22 million events. Signal mode data come from the NQNE03, NQNE04, and NQNE05 tapes. These tapes contain a total of 9.01 million events.

CHAPTER 4
THE EVENT RECONSTRUCTION

The event reconstruction is made up of two separate and complementary pieces. The first is a track-finding algorithm using drift chamber hits to reconstruct the trajectories and momenta of charged particles. The second is a CsI clustering algorithm which reconstructs the energies of clusters in the calorimeter.

Roughly speaking, the event reconstruction proceeds as follows. First, track candidates in the x- and y-views are identified. If the right number of track candidates are found, then the energy clusters in the calorimeter are reconstructed. Corrections to the tracks are then calculated and kinematic quantities evaluated.

4.1 The Database

The online and offline calibration constants in KTeV are stored in a database based on the CERNLIB HEPDB system. The reliable KTeV database architecture makes the job of book-keeping and simulating different parts of the analysis trouble-free, since the right constants are identified by detector, run number and isource. The isource identifier refers to a constant (isource=1) used during the run, (isource=2) used in the Level 3 filter, and (isource=3) used in the offline analysis following extensive calibration.

4.2 Tracking

The "T3" tracking algorithm [54] is responsible for finding track candidates. It uses only data gathered from the drift chambers (and no information from the calorimetry), and identifies track candidates in both the x- and y-views.

4.2.1 Hits and SODs

The first task of the tracking code is to find the drift distances of the track to the nearest wires. This information is extracted from the raw drift chamber TDC hits by subtracting a wire-dependent time offset from the TDC value, and then using a look-up table to map the time to a drift distance. If hits are outside a 170 ns wide time window, they are considered to be out-of-time. No drift distance is calculated for such hits. Only the first in-time hit on each wire is used.

Recall that there are two complementary planes in each plane pair of the drift chamber. If a charged particle leaves a hit in both planes of a pair, the two hits are considered a "hit pair". The tracking code compiles a lits of such hit pairs and categorizes them according to the quality of their "sum of distances" (SODs).

Since the two planes in a plane pair are offset by half a cell spacing, or 6.35 mm, the SOD of any hit pair should be equal to this distance, within resolution. Drift distance resolutions are typically $\sim 100\ \mu$m, so the SOD resolution is $\sim 140\ \mu$m.

Figure 4.1 shows how different hit pairs are classified according to their SODs. If the SOD of a hit pair is close to the nominal 6.35 mm, it is considered a "good SOD" pair. (Close is defined as being within 1 mm.)

"Low SOD" pairs where the SOD is less than 5.35 mm sometimes occur. They could be due to the traversal of two tracks through the same cell. This causes the SOD to be low because each sense wire sees the charge from the nearest track, resulting in a SOD lower than the nominal value. Low SOD pairs could also be due to a single track which emits a δ-ray, from an electron knocked off an atom.

Isolated hits carry information only on the distrance from the track to the wire, but not its direction. It is due to intrinsic inefficiencies in the drift chamber planes because of defects on the sense wires. There is no measurable SOD for isolated hits.

The last category is "high SOD" pairs where the SOD is greater than 7.35 mm. These pairs can arise when a tracks passes close to a wire in one of the complementary planes. They are caused by inefficiencies near the sense wire due to radiation damage and insufficient signal gain.

The distribution of SODs from all plane hit pairs in the EEGG data appears

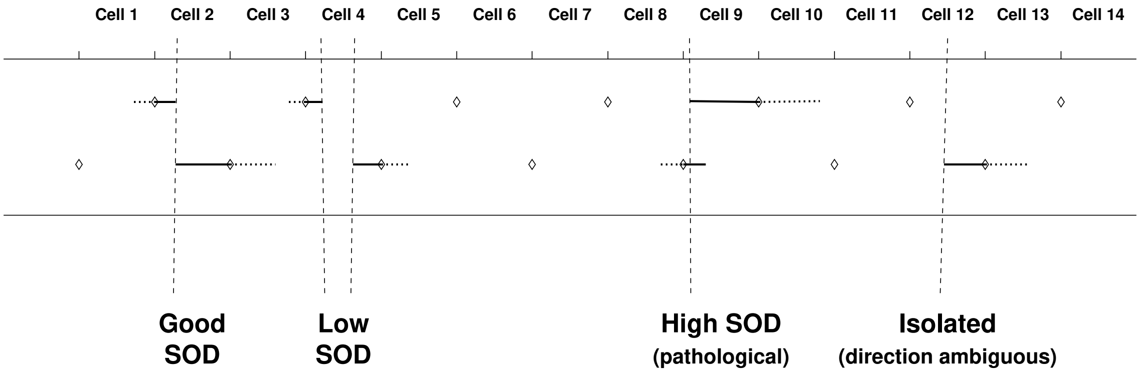

Figure 4.1: Graphical illustration of the different types of drift chamber hit pairs. The diamonds show the sense wire positions, the dashed vertical lines show the paths of the charged particles through the DC, the solid horizontal lines show the true drift distances reconstructed from the hit times, and the dotted horizontal lines show the hit being placed on the other side of the wire.

as Figure 4.2. This dataset contains the $K_L \to \pi^0 e^+ e^-$ signal candidates and the background $K_L \to e^+ e^- \gamma\gamma$.

In the tracking code, each hit pair is given a “quality value” corresponding to the quality of its SOD. Good SOD pairs are assigned a quality value of 4, low and high SOD pairs a quality of 2, and isolated hits a quality of 1.

4.2.2 X and Y Track Candidates

After hit pairs have been identified and a quality value has been calculated for them, the next step in the tracking algorithm is to look for track candidates. Track candidates are searched for separately in the x- and y-views. No constraints are placed on track candidates at this stage; they are not required to originate from the beam or to point to the calorimeter, and the same hits or hit pairs may be shared by more than one track candidate.

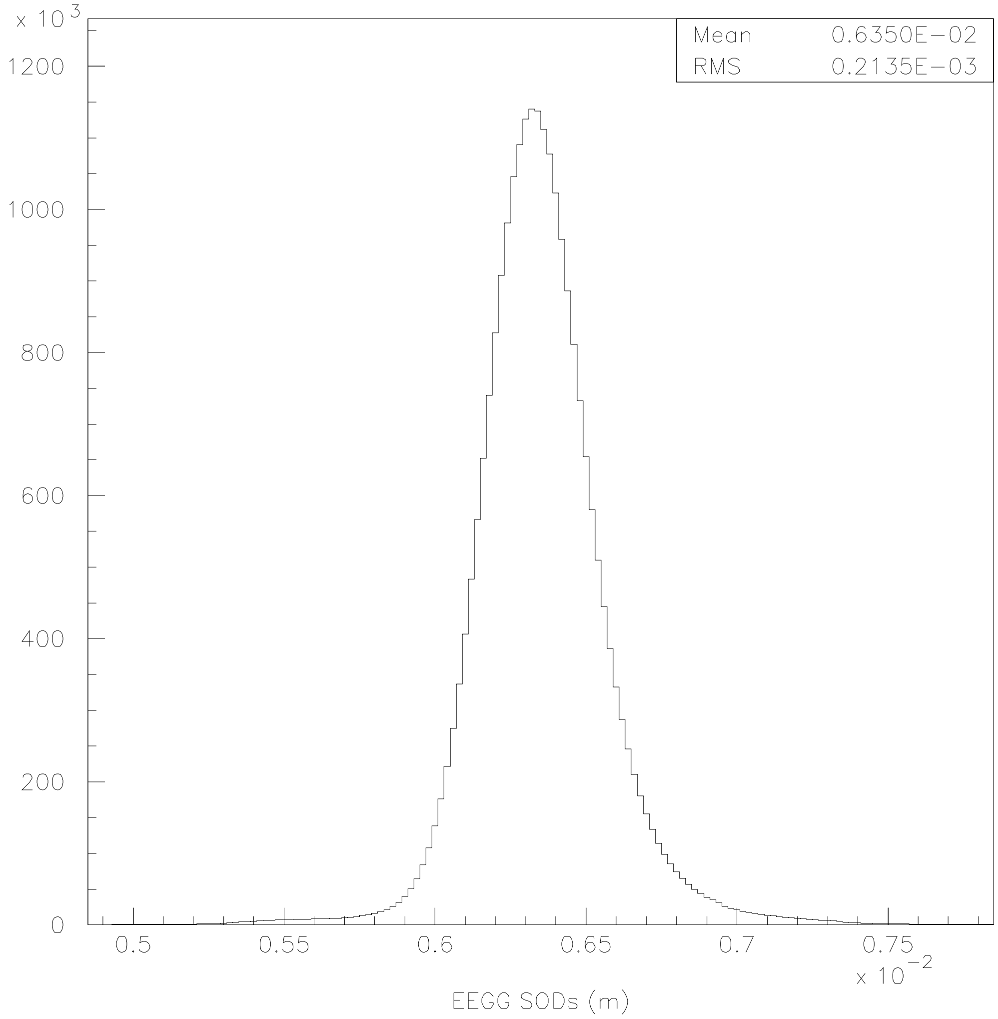

Figure 4.2: Distribution of SODs from the EEGG dataset, which contains $e^+e^-\gamma\gamma$ events. Isolated hits, with no calculable SOD values, are not shown. The mean of the distribution falls right at the mean of the nominal sense wire spacing of 6.35 mm.

4.2.2.1 Finding Y Tracks

The tracking code searches for tracks in the y-view first since the analysis magnet bends tracks in the x-view and not the y-view, making the Y track algorithm more straightforward and reducing the number and complexity of the combinatorics.

The tracking code begins by looking for one pair of hits in DC1 and one pair in DC4 and drawing a line between them. Any pairs in DC2 and DC3 which are less than 5 mm distant from this line are found and the quality values of the pairs from the four chambers are added. To qualify as a Y track candidate, a track need not have the quality sum of a perfect track (4 good SODs), which is 16 (4 good SODs $\times$ quality value of 4 per good SOD). If the sum is 11 or larger, the four pairs are considered a Y track candidate. A quality sum of 11 corresponds to two good SODs, one low or high SOD, and one isolated hit. It is also the minimum sum of a track with at most one isolated hit.

If a track passes the quality sum test, it must still have an acceptable track χ^2 in order to be kept as a Y track candidate. If the χ^2 of the track fit to a line is not normalized to the expected hit resolution, then the sum of the squares of the residuals must be less than 4×10^{-6} m^2.

After all Y track candidates are processed, the tracking algorithm decides whether to keep or reject the event. Events are retained only if there are two or more Y track candidates that can coexist with one another. Two tracks can coexist with each other if they do not share any hits or good SOD pairs, although tracks are allowed to share hits in one chamber if each track includes the hit in different good SOD pairs. This is because the hit ambiguity can be resolved at a later stage, after all final X and Y track candidates are determined.

4.2.2.2 Finding X Tracks

Because the analysis magnet bends tracks in the X direction, finding X track candidates is more complicated. The tracking algorithm first finds track segments in the x-view, between DCs 1 and 2, and between DCs 3 and 4. A line is drawn between each pair in DC1X and in DC2X. If the quality sum of the hit pairs is at least 4 and the line makes an angle of less than 100 μrad with respect to the Z axis, the pairs qualify as an upstream X track segment. In a similar fashion, lines are drawn between pairs in DC3X and DC4X. In order to be considered a downstream X track segment, however, the sum of the quality values must be 5 or greater and the angle with respect to the Z axis may not exceed 150 μrad.

For each pair of upstream and downstream X track segments, the distance between their projections to the midpoint of the magnet bend plane at $z = 170.0$ m is calculated. If the separation distance is less than 6 mm and the quality values of the hit pairs of the two segments add up to at least 11 cm, then the two segments are considered to form an X track candidate. If an event has fewer than two X tracks that coexist, it is rejected.

4.2.3 Track Vertex Candidates

At this point, there are at least two X and two Y track candidates that have been identified. The z positions where each pair of Y track candidates intersect are calculated, and the same is done for X track candidates. The algorithm then finds all combinations of two track candidates in each view intersecting at the same z and located within the decay area. This is defined to be a vertex candidate. Requirements are kept fairly loose, so that some events have many vertex candidates. The two X tracks in a vertex candidate are required to bend in different directions at the analysis magnet, consistent with the hypothesis of two oppositely charged particles.

There is no way to pair specific X and Y tracks of a vertex candidate at this point. Consider the case of just two X and two Y track candidates. It is impossible to decide which of the two pairing combinations that result is the right one, since each Y track candidate can be paired with either of the two X track candidates. CsI calorimeter cluster position information is required in order to resolve this ambiguity.

4.2.4 Event Display of Tracks

Data and MC events can be displayed by a convenient event viewing utility called KDISP. The X and Y track candidates for a typical $K_L \rightarrow e^+e^-\gamma\gamma$ background event can be seen in Figure 4.3.

4.3 Energy Reconstruction and Clustering

4.3.1 Energy Calibration

Digitized PMT (DPMT) [55] signals are read out for the time slice containing a trigger and the subsequent three time slices. In order to translate the DPMT readings to actual energies deposited in the crystal, an energy calibration which involves two separate stages is required. The DPMT response to different levels of light in the crystal must first be linearized. This is done by calibrating with a laser flash system using information obtained by scanning the array many times during the run. Then another calibration must be done to determine the energy scale converting DPMT output to actual energy. This measurement is performed with K_{e3} electrons. The E/p (CsI energy / track momentum) response for each crystal is estimated using a rough set of CsI energy calibration constants. The true gain is the factor that scales the measured E/p to the value 1.0.

4.3.2 Clustering Algorithm

The first step in the clustering algorithm is to search for "cluster seed" blocks, or local maxima, in crystals for which the HCC bit is set. The HCC flags crystals with 50 MeV or more energy. Clusters are found by summing the energies from a pre-defined number of crystals surrounding the cluster seed. For the small 2.5 cm $\times$ 2.5 cm crystals, this is a 7 $\times$ 7 array of crystals centered around the seed block. For the large 5.0 cm $\times$ 5.0 cm crystals, it is a 3 $\times$ 3 array. Along the border between small and large crystals, the large crystal array size is used. Four small crystals are considered the equivalent of one large crystal.

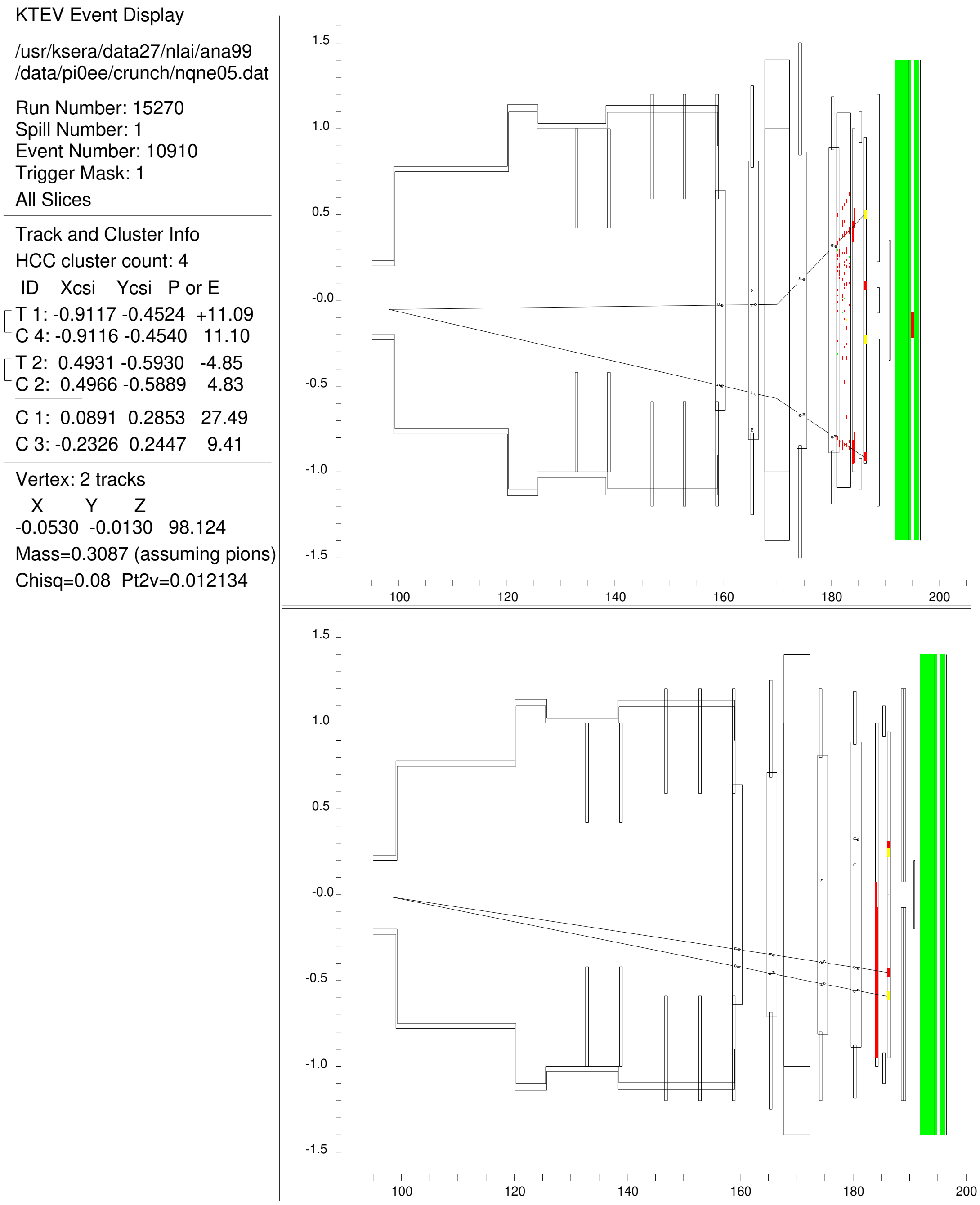

Figure 4.3: The KTeV event display for the X and Y track candidates of a typical $K_L \to e^+e^-\gamma\gamma$ background event. The X track candidates are shown in the top detector diagram and the Y candidates in the bottom. Cluster energies and positions are listed on the left.

4.3.3 Cluster Position

The energy of a cluster is typically spread out over several blocks. The distribution of energy deposited in the blocks of a cluster can be used to deduce where the particle struck the calorimeter. Ratios of the energy in the cluster seed block to the energies in neighboring blocks are first calculated. These ratios are compared to values in look-up tables, which return the x and y coordinates of the cluster position. $K_L \to \pi^0\pi^0$ data and Monte Carlo are used to make separate look-up tables for large and small crystal block regions. The resulting position resolution is $\sim$ 1 mm in small blocks and $\sim$ 1.8 mm in large blocks [56].

4.3.4 Energy Corrections

After the raw cluster energies are determined as described above, several corrections are applied. These corrections fall into two categories: block-by-block corrections modifying the energies of individual crystals within a cluster, and multiplicative corrections which are applied on the total cluster energy.

4.3.4.1 Overlap Correction

Sometimes two or more clusters may share energy deposited in the same crystal or crystals. The overlap correction separates the energy in the crystals amongst the clusters. The algorithm divides the energy amongst the clusters, recalculates cluster energies and positions, and iterates this process until these values converge to within 5 MeV in cluster energy and 100 μm in x and y positions, or until the maximum number of iterations, 20, is reached.

4.3.4.2 Neighbor Correction

Energy in a cluster may sometimes leak out of the 3×3 or 7×7 array defining the extent of the cluster. This energy can significantly distort the energy profile of neighboring clusters. The problem is of particular concern for a low energy cluster beside a high energy cluster neighbor. The neighbor correction is applied to subtract off the expected energy leakage to each cluster from the tails of neighboring clusters. The size and profile of the correction is based on studies of expected shower shapes using GEANT simulation.

4.3.4.3 Missing Block Correction

Clusters overlapping the calorimeter perimeter or a beam hole may have their raw energy reconstructed significantly low, due to missing crystals. The missing block correction uses the same expected traverse shower profiles as the neighbor correction to add back the energy which would have been deposited if there were crystals beyond the edge.

4.3.4.4 Sneaky Energy Correction

Sometimes, the lost energy of a cluster near the beam hole edge may be deposited in crystals on the other side of the beam hole. A cluster at this location could have its energy measurement biased upwards due to the energy that traverses the beam hole from the opposite side. The aptly-named sneaky energy correction is applied to subtract off this energy leakage.

4.3.4.5 Threshold Correction

The readout threshold for crystals is 7 MeV. The outer crystals in a cluster often have energy below this threshold and are removed from the readout list. These crystals are not counted toward the cluster energy, skewing the sum downwards. The threshold correction is applied to rectify this problem. For each cluster, the amount of energy deposited in crystals below the readout threshold is estimated. This correction is a function of the overall cluster energy and the crystal position in the cluster.

4.3.4.6 Intra-Block Correction

The energy response of a crystal varies in the transverse direction. Data from calibration K_{e3} electrons show that the energy response is slightly lower for showers originating near the edge of a crystal than for showers near the center. Because of this effect, the raw energy calculated for a cluster depends on where the particle struck the face of the cluster's seed crystal. To nullify this effect, the intra-block scale correction is applied to each cluster energy. The size of this correction is a function of the position of the cluster within the seed crystal.

4.3.4.7 Non-Linearity Fudge Correction

The corrections above do not completely linearize the crystal response. In a perfectly linear response, the ratio E/p would remain constant over all values of p. However, variations on the order of 0.5% [57] are found. These residual non-linear variations are used to create a non-linearity fudge correction. It is used to cancel out the residual non-linearities in crystal response and is applied after all other corrections. Separate fudges are used for the small and large crystals.

4.3.5 Event Display of Clusters

The convenient KTeV event viewing program also shows calorimeter information. The cluster display for the typical $K_L \to e^+e^-\gamma\gamma$ background event shown in the track display of Section 4.2.4 appears as Figure 4.4.

4.4 Vertex Finding

With the track vertex candidates and the cluster positions in hand, track-cluster matching can proceed. For each track, the matching algorithm calculates the distance between the position of each cluster and the projected track position at the face of the calorimeter. Tracks separated by less than 7 cm from the closest cluster are "matched" to that cluster. X and Y tracks can be paired if both tracks match

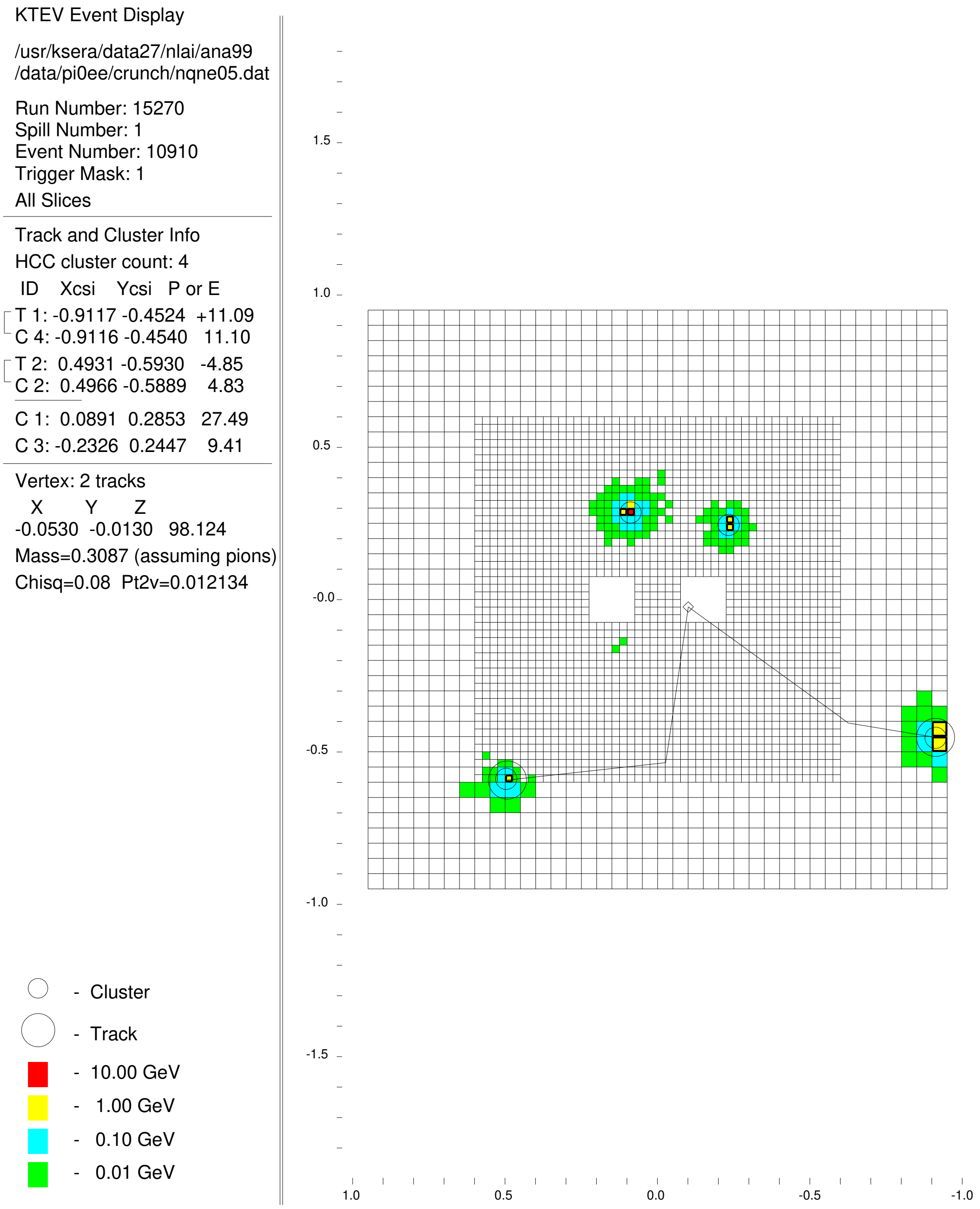

Figure 4.4: The KTeV event display of the clusters for the typical $K_L \rightarrow e^+e^-\gamma\gamma$ background event in Section 4.2.4. The four clusters correspond to the four electromagnetic particles of the final state. Track positions and momenta are listed to the left.

to the same cluster and they are separated by less than 1.5 cm of each other in x and y at the calorimeter face.

For the vertices found passing matching, tracking corrections are made to account for fringe fields from the analysis magnet, chamber alignment, and corkscrew rotations between chambers. Following these corrections, a χ^2 is calculated based on the modified z position of the vertex, the matching of upstream and downstream X track segments, and the total number of bad SODs included. The candidate with the smallest χ^2 is selected as the final "charged" vertex.

CHAPTER 5
THE MONTE CARLO SIMULATION

The Monte Carlo (KTEVMC) simulation is an essential part of the analysis for a number of reasons. First, it allows the overall acceptance of the normalization and signal modes to be determined. Secondly, the MC is used to determine the number of background events remaining in the signal candidate sample after all cuts are made. Lastly, by comparing data with MC, the performance of KTeV detector components can be evaluated and where needed or desired, corrected for.

This chapter discusses the KTeV Monte Carlo (KTEVMC) simulation in detail. The main steps are the kaon generation, the decay into various relevant modes, the tracing of the decay products in the detector volume, the simulation of accidental activity in the detector, and the trigger simulation.

5.1 Kaon Production

The generation of Monte Carlo events begins with the production of K^0 and $\overline{K^0}$ by protons on the BeO target. To determine the distribution in kaon momentum and angles, the charged kaon cross section parameterized by Malensek [58] is used. By counting valence and sea quark combinations, the size of the neutral kaon production can be related to that for charged kaons. This argument assumes that a u or d quark can come from both valence or sea, but that s quarks and anti-quarks come only from the sea. It also assumes that there are equal $u\overline{u}$ and $d\overline{d}$ components in the sea. With these assumptions, it is found that the neutral kaon cross section is related to the charged kaon cross section by:

$$K^0 \sim \left(K^+ + K^-\right)/2 \tag{5.1}$$

$$\overline{K^0} \sim K^- \tag{5.2}$$

The weights for individual quarks in the kaons are listed in Table 5.1. The relative mix predicted is approximately 55% K^0 and 45% $\overline{K^0}$.

Particle	Quark Content	Weight
K^+	$u\bar{s}$	(2+x)y
K^-	$\bar{u}s$	xy
K^0	$d\bar{s}$	(1+x)y
$\overline{K^0}$	$\bar{d}s$	xy

Table 5.1: The relative quark weights of the charged and neutral kaon species are listed. The beam proton has two u quarks and one d quark in the valence. The sea quark content relative to the valence is represented by the variable x for $u\overline{u}$ and $d\overline{d}$ and by y for $s\overline{s}$.

The Malensek approximation to the production spectra for K^0 and $\overline{K^0}$ is modified by a polynomial correction to match the observed $K_L \to \pi^+\pi^-$ spectrum. A more extensive discussion on K^0 and $\overline{K^0}$ production is available in [59] and numerical details on the KTeV kaon production algorithm are presented in [60].

5.2 Kaon Decay

Next, the generated kaon is projected to the vacuum decay region. If the kaon trajectory intersects any collimator, the event is rejected and a new kaon is generated.

Kaons generated in this analysis have a momentum between 20 and 200 GeV/c and are forced to decay between z = 90 m and z = 160 m. The initial K^0 - $\overline{K^0}$ state is evolved to the point of decay. For decay modes in which $K_L - K_S$ interference is an important consideration, including modes accessible to K_L and K_S with comparable probability, the full amplitude evolution is extended to the decay position. One example is the $K_L \to \pi^0\pi^0_D$ normalization mode, because $\pi^0\pi^0$ decay represents over 30% of all K_S decays. On the other hand, for modes in which K_S contamination is negligible, a pure K_L exponential decay distribution is used.

The various kaon decays are handled by different decay generators. The generators for the normalization and signal modes of this analysis are discussed in the following sections.

5.2.1 $K \to \pi^0\pi^0_D$ *Generation*

This kaon decay into two neutral pions is a simple two-body decay. At a $c\tau$ of approximately 25 nm, the π^0 lifetime is so short that the π^0 decay location can be considered to be at the kaon decay. The π^0 decay to two photons is the dominant decay mode and is another two-body decay.

The internal conversion of one of the photons in the more abundant $\pi^0 \to \gamma\gamma$ decay mode leads to the Dalitz decay of the π^0, which occurs about 1.2% of the time. Calculation of the rate has been done by Kroll and Wada [61] and $O(\alpha_{EM}^2)$ radiative corrections of Mikaelian and Smith [62, 63] are included. These corrections take into account inner bremsstrahlung like $\pi^0 \to e^+e^-\gamma\gamma$ and virtual-photon corrections to the $M_{e^+e^-}$ spectrum. The infrared threshold is set at $\mathrm{M}_{\gamma\gamma} > 1$ MeV/c^2. Form factors measured by the CELLO collaboration [64] are also included.

5.2.2 $K_L \to \pi^0 e^+ e^-$ *Generation*

This $K_L \to \pi^0 e^+ e^-$ decay is randomly generated using a uniform phase space constraint. This is used because the sensitivity of this search permits only non-standard-model processes contributing to this decay to be found. The flat phase space model represents the least biased view for such a search.

5.3 Tracing of Decay Products

After a kaon decay is simulated, the next step is to trace the decay products through the detector. The tracing process is terminated when the particle is stopped in a detector component, it decays or converts, or the particle escapes the detector volume.

Particles can undergo a number of interactions with material in the detector.

Charged particles can undergo multiple scattering. This process is simulated in KTeV using the Moliere theory [65], which provides for both a Gaussian scattering angle distribution and a nongaussian single-scattering tail. Simulation of multiple scattering is done for detector elements separately described by a radiation length. In addition to multiple scattering, electrons may also undergo bremmstrahlung with emitted photons according to the Bethe-Heitler cross-section [66]. Radiated photons tend to be collinear with the electron. Photon conversion to an e^+e^- pair is simulated with a probability of $1 - e^{-\frac{7}{9}(X/X_0)}$, where X/X_0 is the radiation length traversed by the photon. The conversion spectrum uses the Bethe-Heitler formula and the angle of emittance of the electron-positron pair uses routines from the EGS4 package [67].

Conversion electrons and bremsstrahlung photons produced as particles interacted with matter are also traced through the detector.

5.3.1 Photon Vetoes

If a particle hits one of the photon vetoes (the RCs, SAs, and CIA), particle tracing is terminated and all its energy is deposited in the detector. The detector response is smeared by a Gaussian distribution whose width is the resolution of the detector. Charged pions and muons are scattered through 16 radiation lengths and deposit a minimum ionizing particle's energy loss in the detector. Particles passing outside the perimeter of the vetoes are considered to have escaped the detector volume and tracing is stopped.

5.3.2 Spectrometer

5.3.2.1 Drift Chambers

When a charged particle traverses the drift chamber planes, the hit locations are found by selecting the closest sense wires. The resulting distances are smeared by a Gaussian with width equal to the measured position resolution of the drift chamber, which is approximately 100 μm. Raw SODs are calculated and several corrections are applied to these values to more closely model SOD effects observed in the data. Inefficiency is simulated by masking out additional hits on a wire for a period of

45 ns after the wire is hit, making it effectively "dead" during this period of time. δ-rays, created when particles "knock-on" electrons in the drift chamber gas, are also simulated. They can contribute to chamber inefficiency by producing spurious tracks that ionize the gas, leaving extra hits on sense wires. These tracks from δ-rays can pass closer to the sense wires than the original tracks and thus cause low SOD pairs to be recorded.

5.3.2.2 Analysis Magnet

Charged particles are given a transverse momentum kick in the $\pm x$ direction as they cross the plane of the analysis magnet. A constant kick of approximately 150 MeV/c is imparted at the midplane of the magnet at $z = 170$ m. The exact values are stored in the database. They come from calculations of the P_t kick required in order for the invariant mass of reconstructed calibration $K_L \to \pi^+\pi^-$ events to match the kaon mass.

5.3.3 TRDs

Particles pass through the TRDs after DC4. The eight planes of the TRDs are simulated as 0.14 X_0 amount of material. In the beam region, which contains no radiator material, 0.04 X_0 is assumed. Photon conversion in the TRDs is simulated, but scattering off the individual TRD wires is not. The pion rejection and electron tagging performance of the TRDs are not simulated, but are instead measured using data.

5.3.4 Trigger Hodoscopes

After the TRDs, the particles are transported to the trigger hodoscopes. If a charged particle hits a scintillator paddle in V or V′, a pulse is generated for that counter and a hit multiplicity count for the trigger is incremented. Counter efficiencies based on those measured in the data are assumed for each counter plane.

5.3.5 CsI Calorimeter

Depending on the particle species, several things occur in the simulation when a particle impinges on the face of the calorimeter. Electrons and photons produce electromagnetic showers. Muons deposit minimum ionizing energy in the calorimeter and are allowed to pass through the calorimeter. Pions could also leave minimum ionizing energy or initiate a hadron shower.

For particles producing electromagnetic showers, the transverse position of the shower is the projection of the particle trajectory into the calorimeter to the depth where the shower is initiated. Photons travel on average 1 cm further than electrons before showering. The shower mean depths for electrons and photons are [68]

$$z_e(E) = 0.11 + 0.018\ (\ln\ E) \tag{5.3}$$

$$z_\gamma(E) = 0.12 + 0.018\ (\ln\ E) \tag{5.4}$$

where E is the incident energy of the particle, expressed in GeV. The shower mean depths z_e and z_γ are measured in meters.

Electromagnetic showers are simulated using a shower library generated using GEANT. Each shower in the library contains energy information for an array of 13 $\times$ 13 small crystals. Large crystals are equivalent to a 2 $\times$ 2 array of small crystals.

Showers in the library are generated in one of six energy bins: 2, 4, 8, 16, 32, or 64 GeV. The entries are indexed by a position bin number identifying the transverse location of the shower center within the crystal. These bins range from 0.7 mm at the center of the crystal to 0.2 mm along the perimeter. The binning pattern is finer towards the edge of the crystal because the distribution of energy among the center crystal and its neighbors depends much more sensitively on position near a crystal boundary. All shower configurations can be determined using energy information generated for only one octant of the crystal because showers outside of the octant can be inferred by symmetry. The binning pattern described here appears as Figure 5.1.

When an electron or photon hits a CsI crystal, an electromagnetic shower is generated. It is chosen from the shower library and is based on its transverse po-

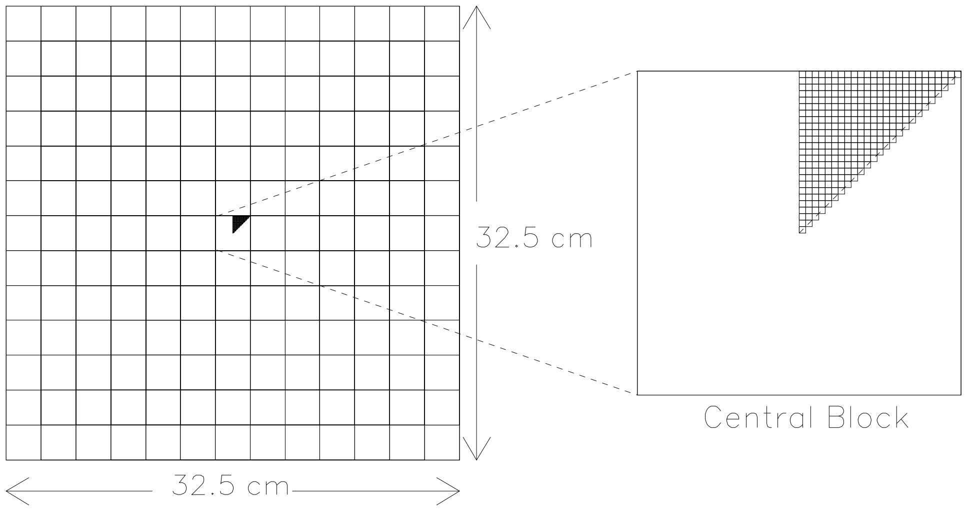

Figure 5.1: The position bins storing the GEANT electromagnetic showers in the Monte Carlo. Showers for positions outside of the octant can be referred to bins inside the octant by symmetry.

sition, z_e or z_γ, at the shower mean. Before look-up, the actual energy is distorted by a Gaussian to simulate the observed energy resolution of the CsI. The generated showers are scaled to the energy of the incident particle.

Shower response is also divided into 25 separate 2 cm bins along z. The simulated light output for a crystal is the result of convoluting the GEANT shower with known z dependencies in longitudinal light yield.

Pions showers are simulated from a hadronic GEANT shower library. Each entry from this library contains information for an array corresponding to 41×41 small blocks and has coarser transverse binning of 25 bins in an octant. Simulation of pion showers is similar to that discussed previously for electromagnetic showers.

5.4 Accidental Overlays

Beam interactions, cosmic rays, and debris from the target and vacuum window can all contribute to accidental activity in the detector and run-by-run samples are recorded to tape using an accidental trigger uncorrelated with detector activity from kaon decays. After a MC event is generated and all particles are traced through the detector, an accidental event is read from disk. Calorimeter energies from the accidental event are added to the simulated event. Track chamber hits are overlaid on the generated hit list. If any generated hit follows an accidental hit by less than 45 ns, the generated hit is eliminated in order to simulate the sense wire discrimator dead time.

The effect of accidental activity on an event is included before readout thresholds and trigger evaluations are performed. This ordering is important because accidentals cause an event to be rejected outright by firing a veto counter or cause an event to be accepted by boosting a signal energy to above threshold.

CHAPTER 6
THE NORMALIZATION MODE ANALYSIS

In order to calculate a branching ratio number or upper limit for a signal mode, the number of actual K_L decays, called the K_L flux, must be determined. However, the production of K_L's in KTeV is not tagged; only actual K_L decays are observed. Hence to calculate the K_L flux, a reasonably well-measured reference K_L decay must be used as a normalization mode. The branching ratio of the signal mode then depends on the branching ratio of the normalization mode, the ratio of acceptances, and the ratio of events observed:

$$BR_{signal} = BR_{normalization} \times \frac{N_{signal}}{N_{normalization}} \times \frac{A_{normalization}}{A_{signal}} \tag{6.1}$$

where BR is the branching ratio, A is the acceptance as measured in the Monte Carlo simulation of detector response, and N is the number of events seen in the data. Here, the signal mode is $K_L \to \pi^0 e^+ e^-$. Because N_{signal} is expected to be small, the method used for analyzing small signals is that proposed by Feldman and Cousins [69].

6.1 Motivation

There are several reasons why $K_L \to \pi^0 \pi^0_D$ decays are used to provide normalization for $K_L \to \pi^0 e^+ e^-$. First, $K_L \to \pi^0 \pi^0_D$ is a relatively abundant mode whose branching ratio is well known. Second, it is important to look for a reference normalization mode as similar as possible to the signal mode. If reconstruction and analysis proceeds in the same manner for these modes, using many of the same analysis cuts, uncertainties in the efficencies of many cuts will cancel in the ratio. The detector signature of $K_L \to \pi^0 \pi^0_D$ is similar to the signal mode: $K_L \to \pi^0 \pi^0_D$

has the two charged tracks and two photons of $K_L \to \pi^0 e^+ e^-$, with the addition of another photon. Since tracking is expected to generate more systematic uncertainty than the calorimetry, it is important to look for a normalization mode involving two tracks, similarly to $K_L \to \pi^0 e^+ e^-$. This is the $K_L \to \pi^0 \pi^0_D$ mode.

6.2 Branching Ratio

The branching ratio of $K_L \to \pi^0 \pi^0_D$ is the probability of $K_L \to \pi^0 \pi^0$ multiplied by the probability of either pion Dalitz decaying:

$$\begin{aligned} BR(K_L \to \pi^0 \pi^0_D) &= 2 * BR(K_L \to \pi^0 \pi^0) * BR(\pi^0 \to ee\gamma) * BR(\pi^0 \to \gamma\gamma) \\ &= 2 * (9.27 \pm 0.19) \times 10^{-4} * (1.198 \pm 0.032) \times 10^{-2} \\ &\quad *(0.98798 \pm 0.00032) \\ &= (2.194 \pm 0.074) \times 10^{-5} \end{aligned} \tag{6.2}$$

Here, PDG values are used [11].

6.3 Simulated Events

All MC samples are generated with KTEVANA V6.00. 9,999,888 $K_L \to \pi^0 \pi^0_D$ decays are generated between 90 m < Z < 160 m and with momentum 20 GeV/c < P < 220 GeV/c. The spill cut described in Section 6.4.1 is applied at the generation stage.

The acceptance for the $K_L \to \pi^0 \pi^0_D$ channel at several points in the generation process is listed in Table 6.1.

6.4 Basic Cuts

This section describes the most general selection requirements made to identify good data. These cuts are generally applied to both $K_L \to \pi^0 \pi^0_D$ and $K_L \to \pi^0 e^+ e^-$ candidates.

Stage	$K_L \to \pi^0\pi^0_D$ Number passing stage	$K_L \to \pi^0\pi^0_D$ Acceptance of stage
No. Generated	9,999,888	—
In good spills	9,962,868	0.99640 ± 0.00002
Ray tracing	3,662,705	0.36764 ± 0.00015
L1	1,062,686	0.29014 ± 0.00024
L2	738,775	0.69520 ± 0.00045
L3 2e tag	549,139	0.74331 ± 0.00051
EEGGG Filter	268,114	0.48824 ± 0.00067
Total	268,114	0.02681 ± 0.00005

Table 6.1: Acceptance at various stages in the $K_L \to \pi^0\pi^0_D$ generation process. Uncertainties are statistical only. Good spills are discussed in section 6.4.1.

Plots that compare a distribution in Monte Carlo to a distribution in data have the MC spectrum normalized to have the same integrated area as the data, unless otherwise indicated.

6.4.1 Spill Quality Cuts

Events are rejected which come from runs or spills taken when hardware failures in the detector were known to exist. These bad spills are identified by referring to a database of bad-spill bits. The bits that are used to cut on are listed in Table 6.2.

6.4.2 General Reconstruction Cuts

The basic reconstruction cut requirements are that: 1) the minimum number of track candidates is found; 2) a vertex is found; 3) two tracks are found; and 4) both tracks match to clusters and the minimum number of clusters is found. The required number of clusters is five in the case of $K_L \to \pi^0\pi^0_D$ and four in the cases of $K_L \to \pi^0 e^+e^-$ and $K_L \to e^+e^-\gamma\gamma$. The number of events at each stage for the $K_L \to \pi^0\pi^0_D$ normalization mode analysis can be found in Table 6.3.

Note that events have already undergone reconstruction twice, during the L3 trigger and the Crunch stages. Events are cut at this analysis-level reconstruction

Bit	Problem	Cut?
1	Trigger timing	1
2	DPMT pedestal exponent > 0	1
3	Bad DPMT capacitor	1
4	Blown QIE comparator	1
5	Miscellaneous dead DPMT	1
6	DPMT pedestal drift	1
7	DPMT gain drift	1
8	Broken dynode	1
9	Pipeline problems	1
10	Global CsI problems	1
11	ETOT problems	1
12	FERA ADC problems	1
13	DC problems	1
14	Miscellaneous veto counter problems	1
15	Trigger hodoscope problems	1
16	Muon and HA problems	1
17	HCC failures	1
18	Kumquat or Banana problems	1
19	TRD trigger	0
20	Hyperon trigger	0
21	DAQ or L3 failures	1
22	Not a 799 run	1
23	Short run	1
24	Non-standard TRD HV	0
25	1 Dead TRD plane	0
26	Dead TRD planes	1
27	TRD voltage sag	0
28	Severe TRD problem	1
29	Beam problems	1
30-32	Unused	0

Table 6.2: Bad-spill cut summary. In the “Cut?” column, “1” indicates that the cut on the bit is applied, and “0” if not.

Stage	No. Data	No. MC
EEGGG crunch tag	9,219,719	264,462
In good spill	8,614,891	262,287
Minimum no. track candidates	7,137,037	235,168
Vertex	7,136,637	235,167
Two tracks	6,076,333	233,902
Five clusters	6,048,147	233,881

Table 6.3: Number of events present at each stage in the basic reconstruction process.

stage because some requirements are different. In the analysis-level reconstruction, there must be at least two mutually exclusive Y-track candidates, while the L3 and Crunch reconstructions permit overlap in the Y view. Also, in the L3 and Crunch reconstructions, a minimum of two tracks are required, resulting in a significant four-track background in the data. These background events are removed by the analysis-level reconstruction, which requires exactly two tracks.

6.4.3 Reconstructing the Vertex

There are two ways to reconstruct vertex position. One is to use the drift chamber tracking to reconstruct the "charged vertex" from the two charged particles in the event. Another way is to find the "neutral vertex". In this case, first the π^0 candidate is found. This is the pair of unmatched clusters whose combined $M_{\gamma\gamma}$ is closest in mass to M_π, where the charged vertex is used in calculating the mass. In five cluster events, the unmatched neutral cluster is taken to be the Dalitz photon. The neutral vertex is found by applying the M_π constraint to the two neutral clusters making up the π^0 candidate:

$$Z_{\pi^0} = Z_{\mathrm{CSISHM}} - \frac{r_{12}}{M_\pi}\sqrt{E_1 E_2} \tag{6.3}$$

where Z_{CSISHM} is the location of the shower maximum in the CsI calorimeter, r_{12} represents the distance between the two clusters over the face of the CsI, and E_1

and E_2 are the cluster energies. In this formula, the small angle approximation is made [70].

The resolutions of the charged vertex and neutral vertex reconstruction algorithms are shown in Figure 6.1. In the upstream decay region, the charged vertex Z_{ch} has poorer resolution than the neutral vertex Z_{π^0} , at 1.3 m versus 0.6 m. This is a consequence of the fact that opening angles between tracks are typically very small, so that small errors in the measurement of track opening angles have a greater effect on the vertex reconstruction the more upstream the decay region. In the downstream volume, the opening angles are typically larger, and the charged vertex resolution becomes better than the neutral vertex resolution, at 0.09 meters versus 0.28 meters.

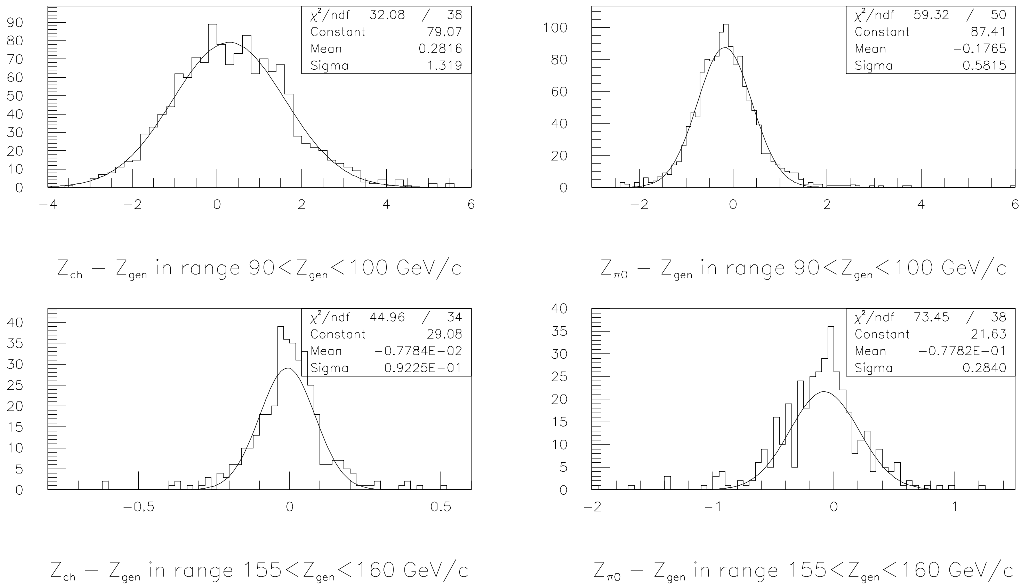

Figure 6.1: Reconstructed decay-vertex Z-coordinate in a sample of $K_L \to \pi^0\pi^0_D$ MC events, near the fiducial limits. The left plots show the charged vertex Z_{ch}. The right plots show Z_{π^0} .

6.4.4 Fiducial Region Cuts

Cuts on vertex Z and total momentum are imposed to make sure that only data events which are inside well-understood, simulated regions are examined in the analysis. The Z vertex cut requires that both Z_{ch} and Z_{π^0} lie between 96 and 158 meters. A comparison of data and MC Z_{ch} and Z_{π^0} distributions appears in Figure 6.2.

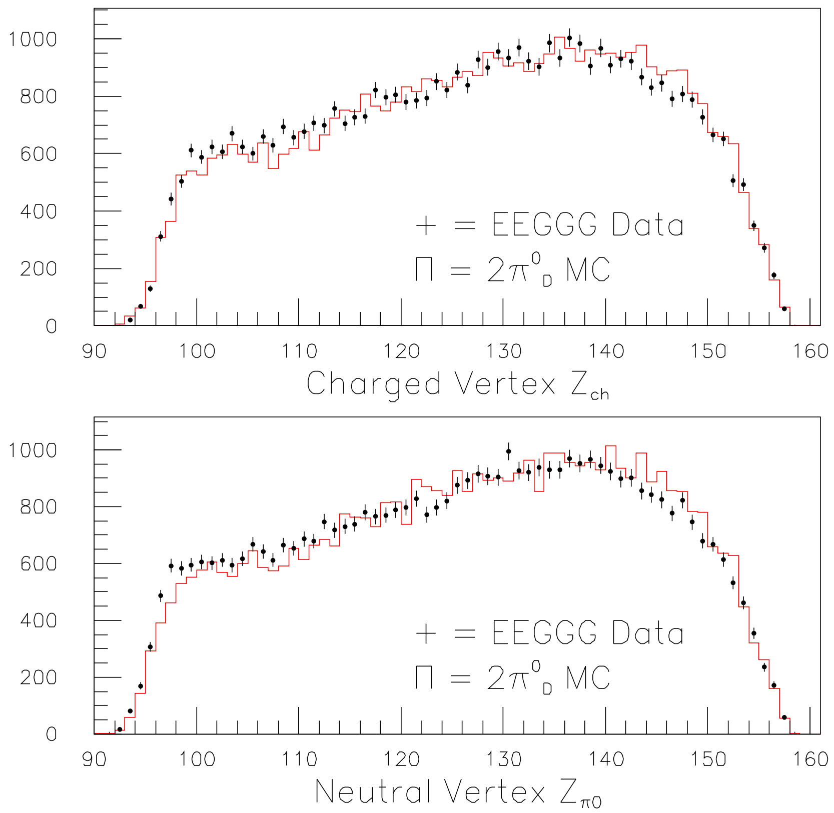

Figure 6.2: The reconstructed decay-vertex Z-coordinate for all data and MC, after all other cuts are imposed. (Top) Charged vertex Z_{ch} . (Bottom) Neutral vertex Z_{π^0} .

The cut on total momentum requires that the reconstructed momentum be between 20.3 and 216 GeV/c. These cut limits are selected because they are several σ away from the 20 to 220 GeV range generated. See Figure 6.3.

A comparison of the reconstructed momentum in data to that in MC events is

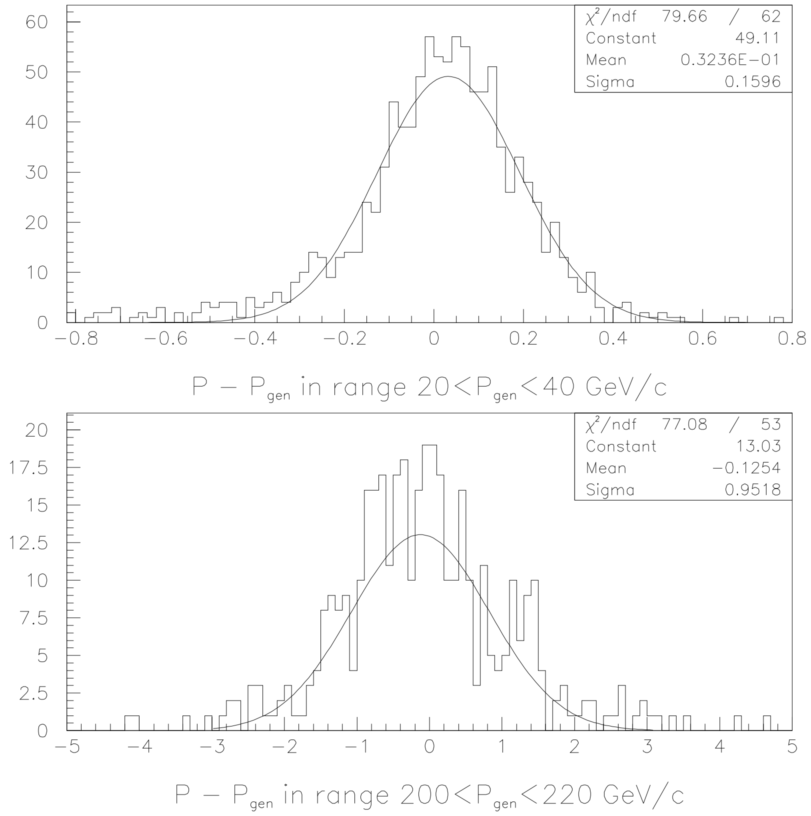

Figure 6.3: Momentum resolution in simulated $K_L \to \pi^0\pi^0_D$. This figure shows the difference between the generated total momentum and the reconstructed momentum in MC events for regions close to the fiducial limits of momentum generation.

shown in Figure 6.4. The data with high momenta are mainly $\mathrm{K_S}$ in the upstream region of the decay volume. The sharp cut-off at low momentum arises because of the ETOT cut, as discussed in Section 6.4.5.

6.4.5 Trigger Verification Cuts

Cuts are imposed to reject events close to a trigger threshold, in order to avoid potential performance variations and simulation difficulties. Cuts on trigger elements

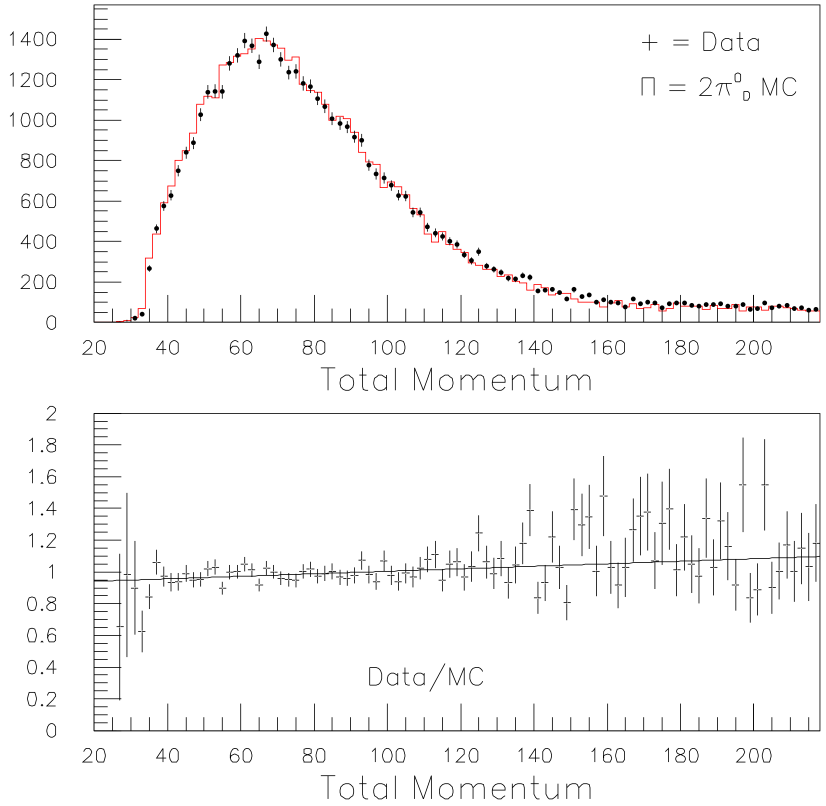

Figure 6.4: (Top) Overlay of the reconstructed momentum in data compared with that in MC, after all other cuts are applied. (Bottom) Ratio of data/MC for total reconstructed momentum.

made in this analysis include requirements on the V-bank counters, the CA, and the total calorimeter energy.

To make sure that tracks are away from the beam holes in the V-banks, it is required that the distance from each track to the nearest beam hole edge be at least 1 cm. A spectrum of the minimum track-hole separation at V0, the upstream V-bank, appears in Figure 6.5.

The nominal veto threshold during data-taking was 12 GeV. In the analysis, the energy of each CA paddle is summed to its neighbor's energy. The analysis cut requires that the maximum of these sums be less than 12 GeV. This cut is very

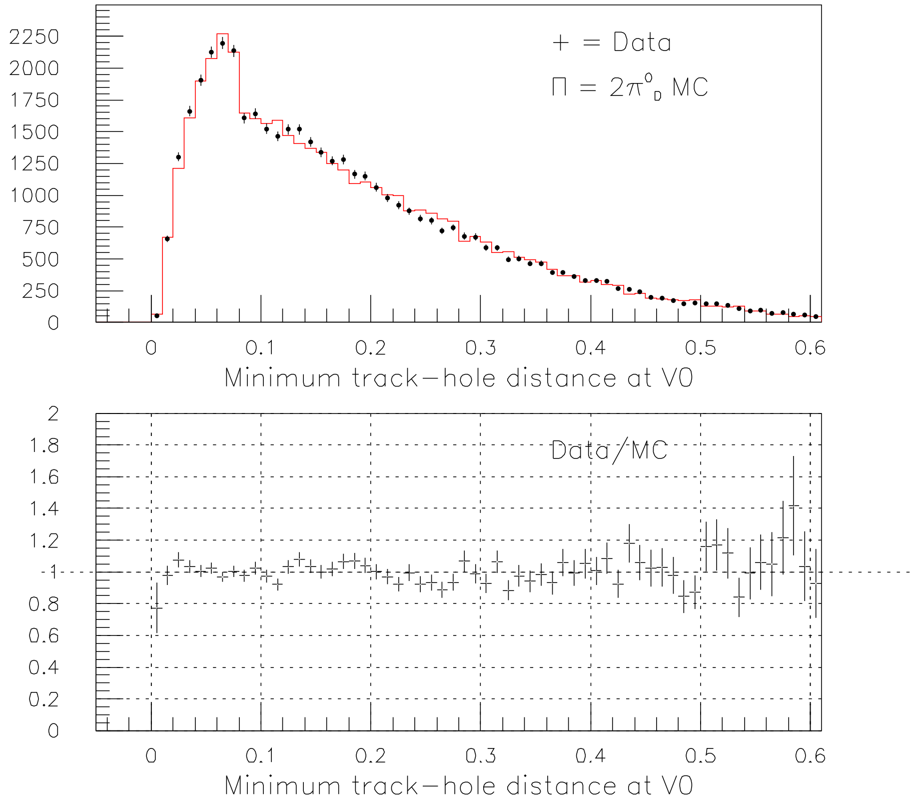

Figure 6.5: Distribution of the minimum track-hole separation at V0, after all other cuts are applied.

loose, as can be seen in the CA in-time energy comparison of data and MC shown in Figure 6.6.

The nominal total calorimeter energy threshold during data-taking was 25 GeV. To stay away from this edge, the sum of the energies in all CsI channels is computed and required to be greater than 33 GeV. The distribution in total calorimeter energy appears in Figure 6.7.

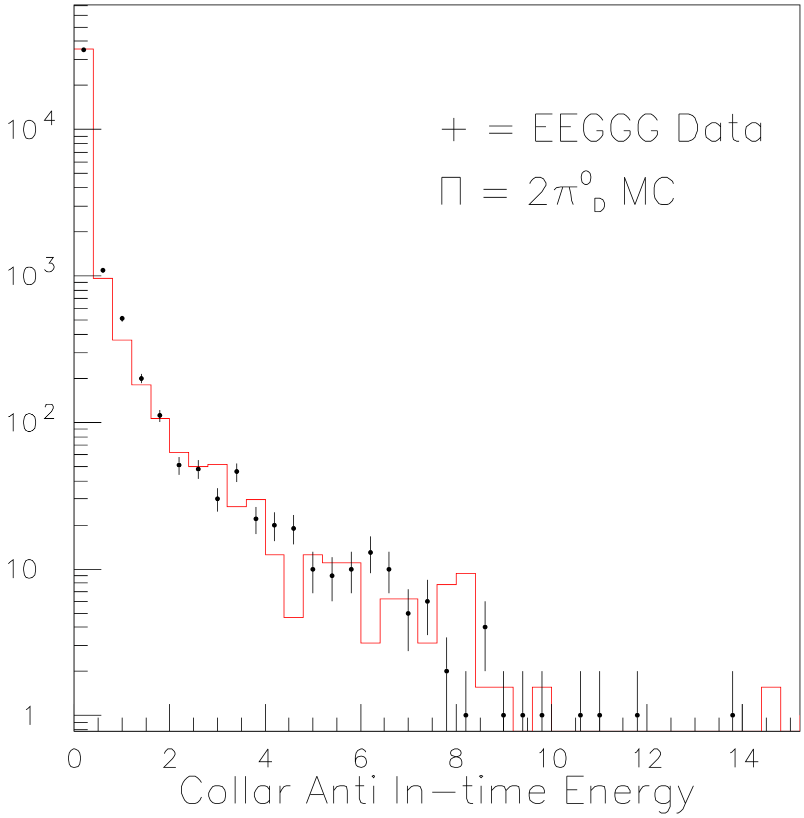

Figure 6.6: Distribution in GeV of the maximum sum of energy in any counter added to its neighbors, after all other cuts are applied.

6.4.6 Cuts on Calorimeter Quantities

There are two selection requirements on calorimeter quantities. The first involves the minimum distance in X or Y from a cluster associated with a track to the nearest beamhole. The cut requires this distance be at least 1.25 cm. Below this, the data/MC ratio becomes relatively small, as shown in Figure 6.8.

Another calorimeter cut is on cluster energy. The energy of each cluster is required to be greater than 2.5 GeV. The distribution of cluster energies in data and MC appears in Figure 6.9.

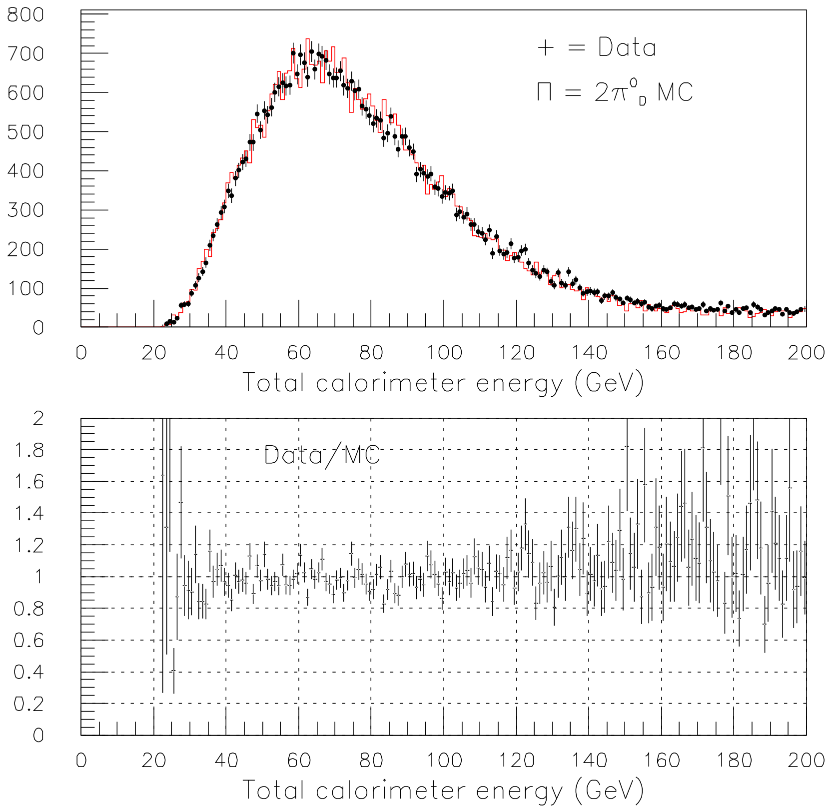

Figure 6.7: Total calorimeter energy (GeV), after all other cuts are applied.

6.4.7 TRD Cuts

Since simulation of the TRDs is not implemented, TRD requirements are applied only to data. The first cut requires that at least one TRD plane has a hit corresponding to each DC track. The second is a fiducial cut on the TRD beam region. Any event which passes through a beam region is rejected, since losses there may not be modeled well in the MC.

The kinematic cuts for $K_L \to \pi^0\pi^0_D$ in Section 6.5 are very effective in eliminating the K_{e3} background to $K_L \to \pi^0 e^+ e^-$. To remove background from this source further, a cut on the pion likelihood variable, TRDLIKE, is placed on both tracks.

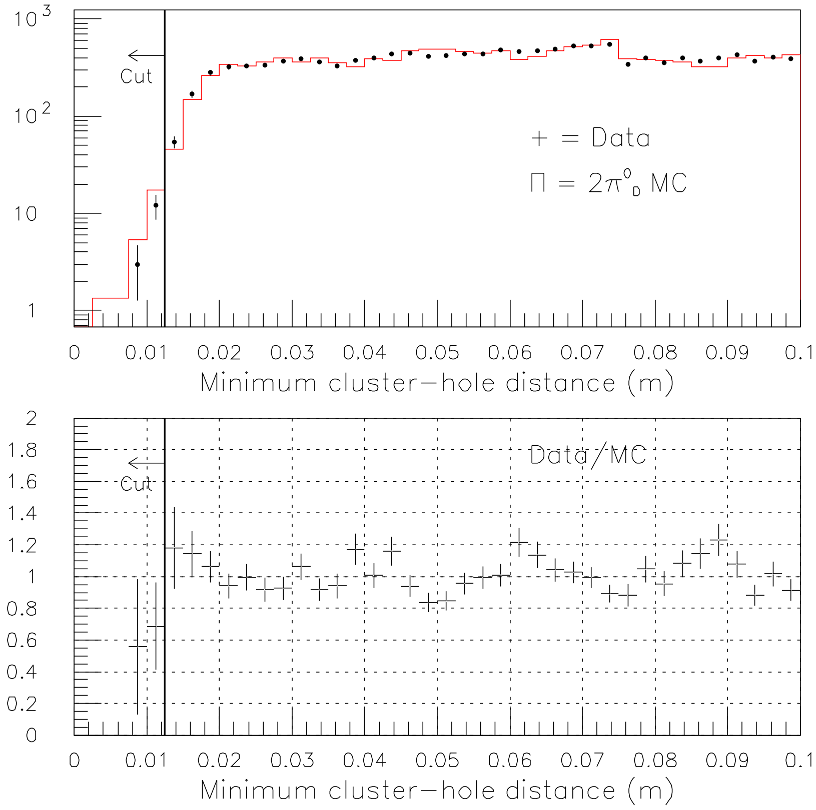

Figure 6.8: The smallest track cluster to hole distance (m), after all other cuts are applied.

The cut is set at a level to optimize signal to background and results in a pion rejection factor of about 50:1, as measured using a sample of $K_L \to \pi^{\pm} e^{\mp} \nu$ decays. The value of the TRDLIKE cut depends on the run number because changes in TRD performance occurred over time. See Table 6.4 for TRDLIKE cut value settings for different run ranges.

There are 45,274 events passing both the number of planes and $\Pi_{\rm TRD}$ cuts out of a total of 51,159 events passing at least all other non-TRD cuts. Therefore, the overall TRD acceptance is 0.8850 ± 0.0014.

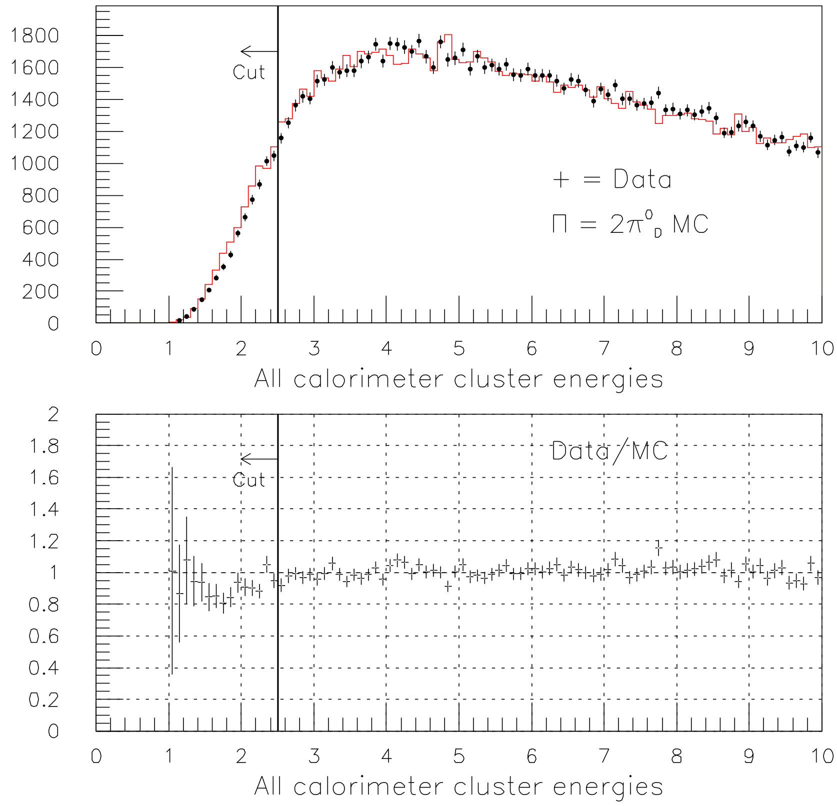

Figure 6.9: All cluster energies (GeV), after all other cuts are applied, except for the requirement on total calorimeter energy.

Run Range	TRDLIKE cut
14625 to 14651	TRDLIKE > 0.2
14652 to 14666	TRDLIKE > 3.0
14667 to 14827	TRDLIKE > 0.2
14828 to 15075	TRDLIKE > -1.8
15076 to 15236	TRDLIKE > -1.0
15237 to 15303	TRDLIKE > -1.8
15304 to 15408	TRDLIKE > -0.6
15409 to 15548	TRDLIKE > -1.4

Table 6.4: TRDLIKE cut values for various run ranges.

6.4.8 E/p Cut

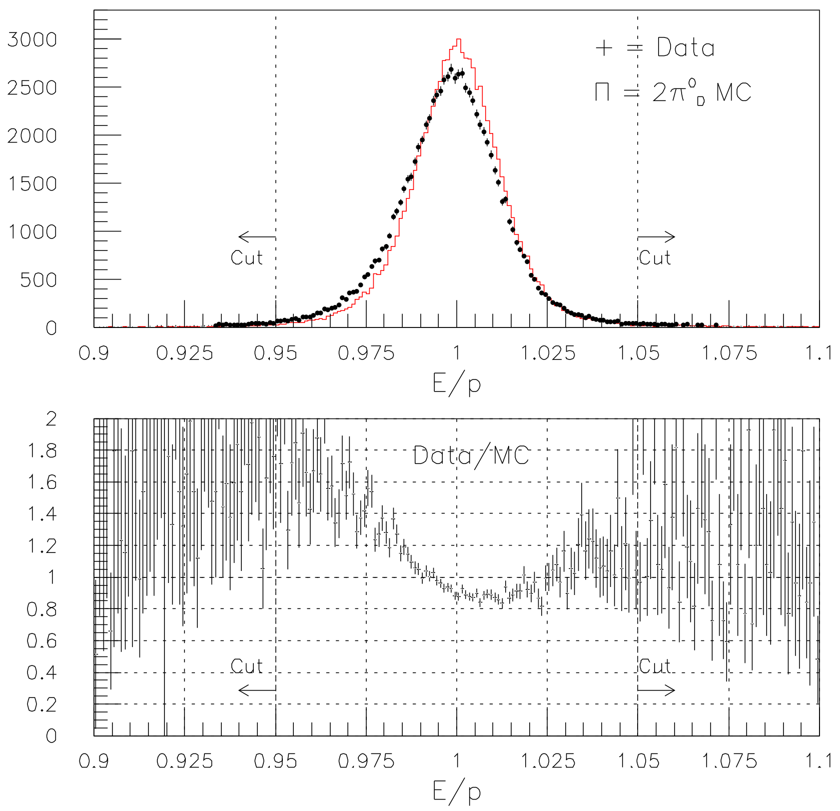

Figure 6.10: E/p for each track in data and MC, after all other cuts are applied.

The distribution of E/p in data is compared to MC in Figure 6.10. The mean of the peak is slightly higher in MC than in data. Experimentally, the E/p distribution has been found to be parametrizable as the sum of two Gaussian functions, as demonstrated in Figure 6.11. The resulting parametrization is:

$$\text{DATA}: \quad E/p = 2396\ \exp\left[-\frac{1}{2}\left(\frac{E/p-0.9986}{0.0122}\right)^2\right] + 152\ \exp\left[-\frac{1}{2}\left(\frac{E/p-0.9969}{0.0351}\right)^2\right] \qquad (6.4)$$

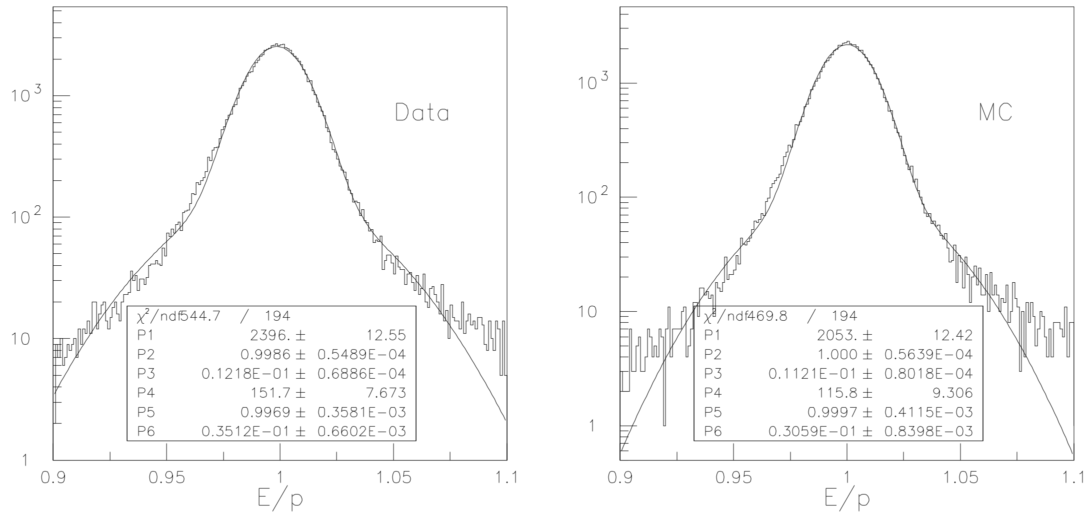

Figure 6.11: E/p distributions for each track in data and MC, after all other cuts are applied. The peak has been fit to a sum of two Gaussians.

$$\mathrm{MC:}\;\; E/p = 2053\;\exp\left[-\frac{1}{2}\left(\frac{E/p-1.0001}{0.0112}\right)^2\right] + 116\;\exp\left[-\frac{1}{2}\left(\frac{E/p-0.9997}{0.0306}\right)^2\right] \quad (6.5)$$

These equations indicate that the MC E/p mean is approximately 0.1% higher than the data mean. The resolution for either distribution is about 1%.

Because the data and MC distributions are somewhat different and in order to maintain insensitivity to their difference in spectra, the E/p cut is kept loose at about 5 σ from the central peak: $0.95 < E/p < 1.05$.

6.4.9 Cuts on Drift Chamber Quantities

To avoid the ambiguity in track-cluster matching when clusters have the same X coordinate, the distance in X between tracks projected to the calorimeter must be greater than 2.5 cm. Because the analysis magnet bends tracks with different charges away from each other, the typical X separation of tracks is relatively large. As a consequence, this selection cut removes fairly few events.

There are somewhat more tracks at small opening angles in MC than in data. To make sure that only events in regions where data and MC match closely are considered in the analysis, cuts in the track separation and in the opening angle are made. The track separation at DC1 for X appears in Figure 6.12 and for Y in Figure 6.13. It is required that there be at least 1 cm separation in both X and Y views between the two tracks. Distributions of the opening angle for data and MC are displayed in Figure 6.14. It can be seen that there are fewer MC events at small angles. The cut on the opening angle is placed at 2.25 mrad. This cut is expensive, since it removes many events from the $K_L \to \pi^0\pi^0_D$ candidate sample. However, there are ample $K_L \to \pi^0\pi^0_D$ data events, and the uncertainty on the flux measurement is dominated by systematics rather than by statistics. Furthermore, the cut removes almost no events in the $K_L \to \pi^0 e^+e^-$ mode.

6.5 Kinematic Cuts Specific to $K_L \to \pi^0\pi^0_D$

The sections above discussed cuts that are common to all modes analyzed in this work. This section describes cuts set at different values for the normalization and signal modes. Also, most of the cuts described previously are detector-based requirements, whereas the remaining cuts are based on kinematic quantities.

6.5.1 $M_{\gamma\gamma}$

The first of these cuts is on the value of $M_{\gamma\gamma}$ for the best pairing, evaluated at the charged vertex. The best pair is defined to be the one whose invariant mass is closest to the neutral-pion mass under the hypothesis that the two photons come from a π^0. An overlay of the data and MC distributions appear in the top plot of Figure 6.15. The top row of plots in Figure 6.16 show the result of fitting Gaussians to both data and MC spectra. The data mean at 135.54 $\pm$ 0.01 MeV/c^2 is significantly higher than the MC mean at 135.35 $\pm$ 0.02 MeV/c^2. Both means are higher than the PDG value of 134.9766 $\pm$ 0.0006. There are several reasons why both means may be high: there could be difficulties stemming from the downstream bias in vertex Z reconstruction or from disparities between the electron and photon cluster energy

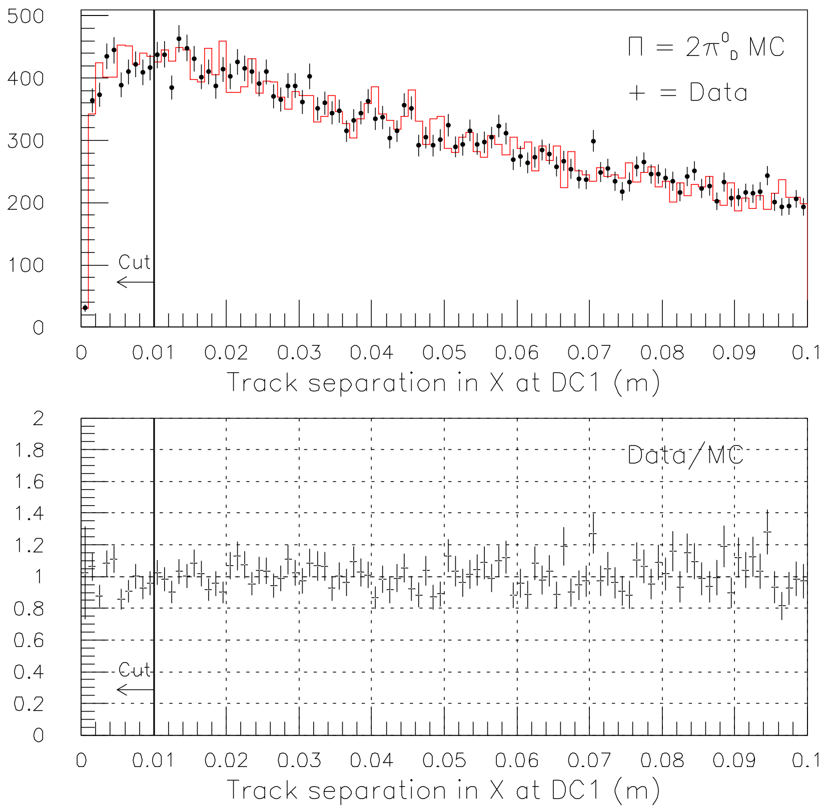

Figure 6.12: Spectrum of ΔX of the tracks at DC1 (m), after all other cuts are applied.

reconstructions. Fortunately, the fact that the MC mean is close to the data mean indicates that the effect is fairly well simulated in the analysis. The data width at 2.09 ± 0.03 MeV/c^2 is a little smaller, but not significantly so, than the MC width at 2.10 ± 0.04 MeV/c^2. To minimize the impact of the differences in mean and width, the selection requirement on $M_{\gamma\gamma}$ is kept loose. Therefore, the cut is centered on the data mean of 135.54 MeV/c^2 and requires $M_{\gamma\gamma}$ to be within 8 MeV/c^2 of this value: $|M_{\gamma\gamma} - 135.54| < 8$ MeV/c^2.

As described in section 6.4.3, Z_{ch} is found from $M_{\gamma\gamma}$. The momentum of all photons is recalculated according to the new neutral vertex and these new values

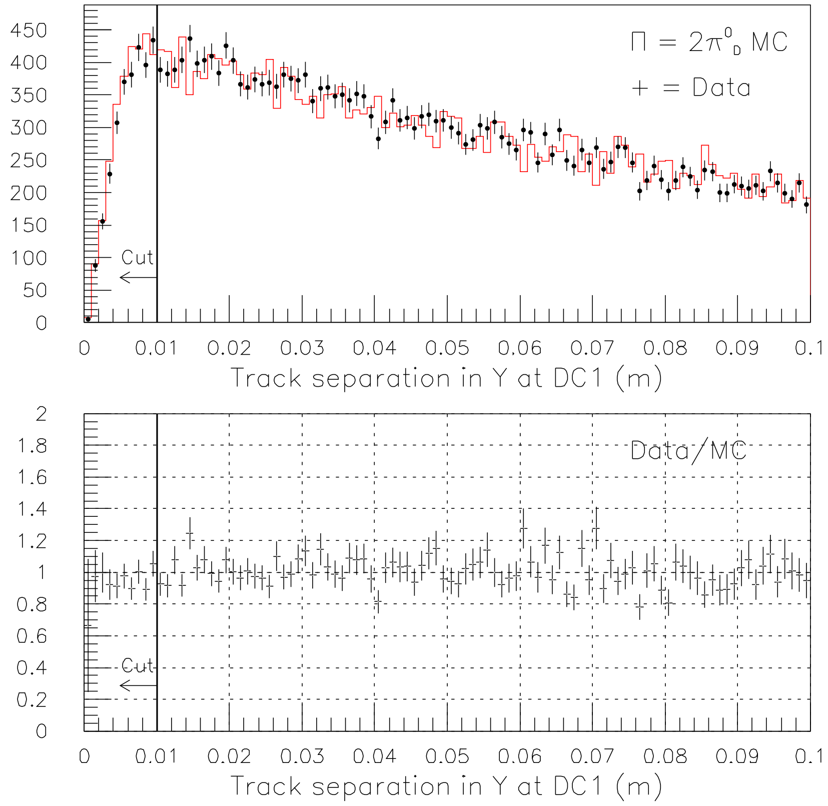

Figure 6.13: Spectrum of ΔY of the tracks at DC1 (m), after all other cuts are applied.

for the momentum are used in the cuts on $M_{ee\gamma}$, $\log_{10} P_T^2$, and $M_{\gamma\gamma ee\gamma}$ below. The resolution of these variables is improved because the neutral vertex resolution is better.

6.5.2 $M_{ee\gamma}$

The mass of the $M_{ee\gamma}$ combination evaluated at the neutral vertex is another selection cut. The data-MC overlay appears in the bottom plot of Figure 6.15. The middle row of plots in Figure 6.16 show the Gaussian fits to the peaks in data and MC.

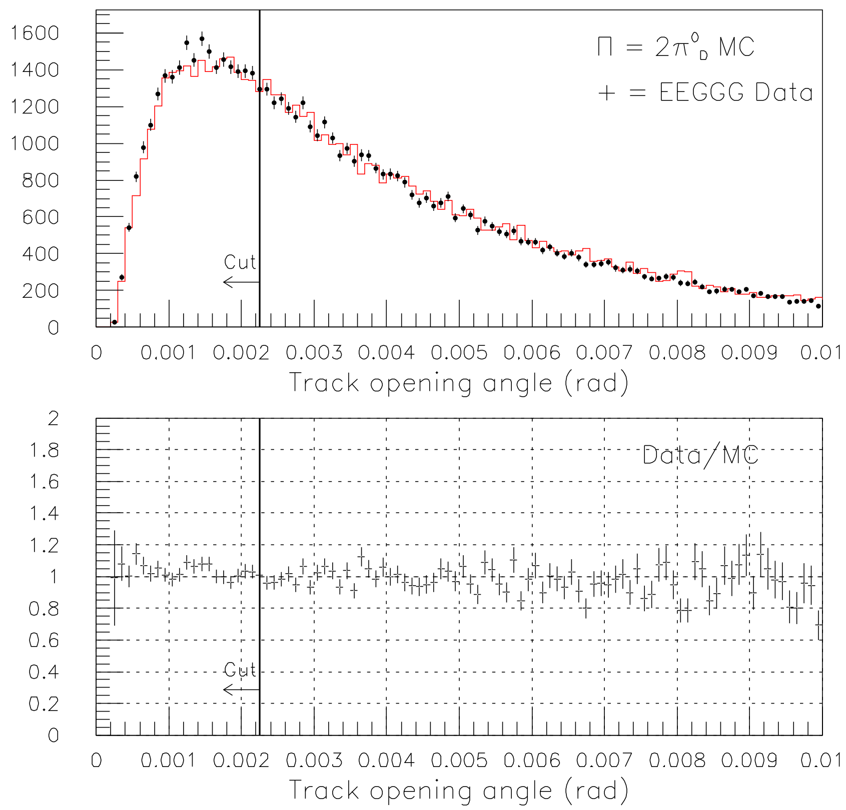

Figure 6.14: Distribution of the opening angle of the tracks at DC1 (rad), after all other cuts are applied.

The correspondence between the data and MC means and widths is good. The $M_{ee\gamma}$ selection requirement is that $|M_{ee\gamma} - M_{\pi^0}| < 6$ MeV/c^2.

6.5.3 $P_T{}^2$

The tranverse momentum, P_T^2, of the daughter particles of the K_L decay is the component of their momentum vector perpendicular to the direction of motion of the K_L. If all decay products are observed, the total transverse momentum should vanish within the resolution of the detector. Placing a cut on the transverse momentum removes background events where particles are missed during the reconstruction.

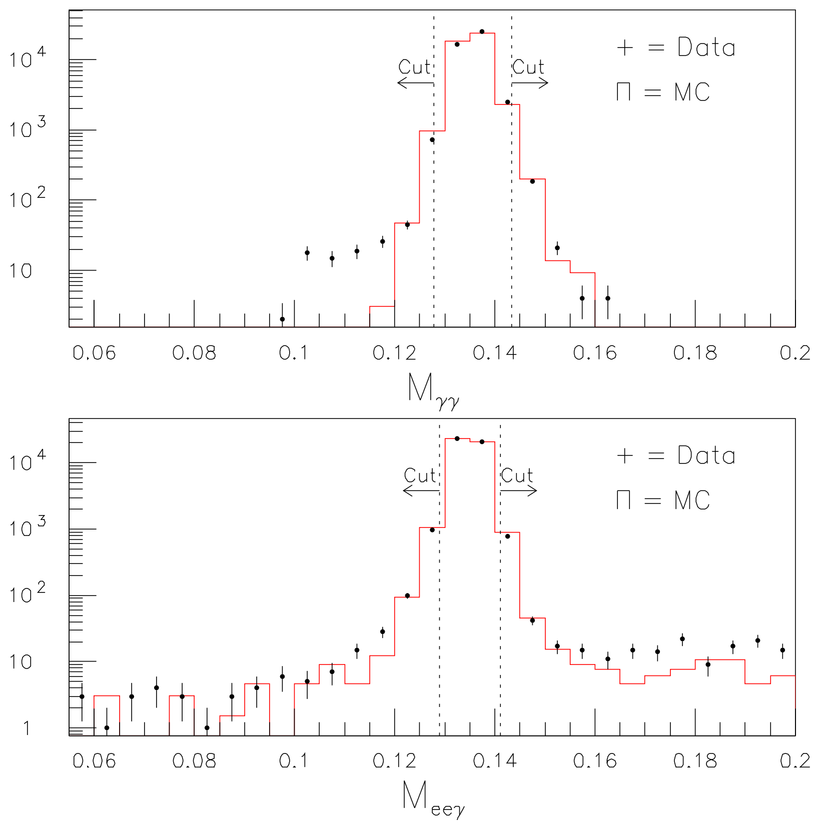

Figure 6.15: Distributions in data and MC of the charged vertex $\mathrm{M}_{\gamma\gamma}$ (top) and neutral vertex $\mathrm{M}_{ee\gamma}$ (bottom). All other cuts are applied.

Requirements are placed on both the transverse momentum calculated using the charged vertex and that calculated using the neutral vertex. The spectra of $\log_{10} \mathrm{P}_\mathrm{T}^2$ versus the reconstructed kaon mass calculated using the neutral vertex appears as Figure 6.17.

6.5.4 $M_{\gamma\gamma ee\gamma}$

The final selection requirement is on the invariant mass of the three photon and two electron combination. Figure 6.18 shows the distributions for data and MC. The spectrum for data indicates the existence of some $K_L \to \pi^0\pi^0\pi^0_D$ background

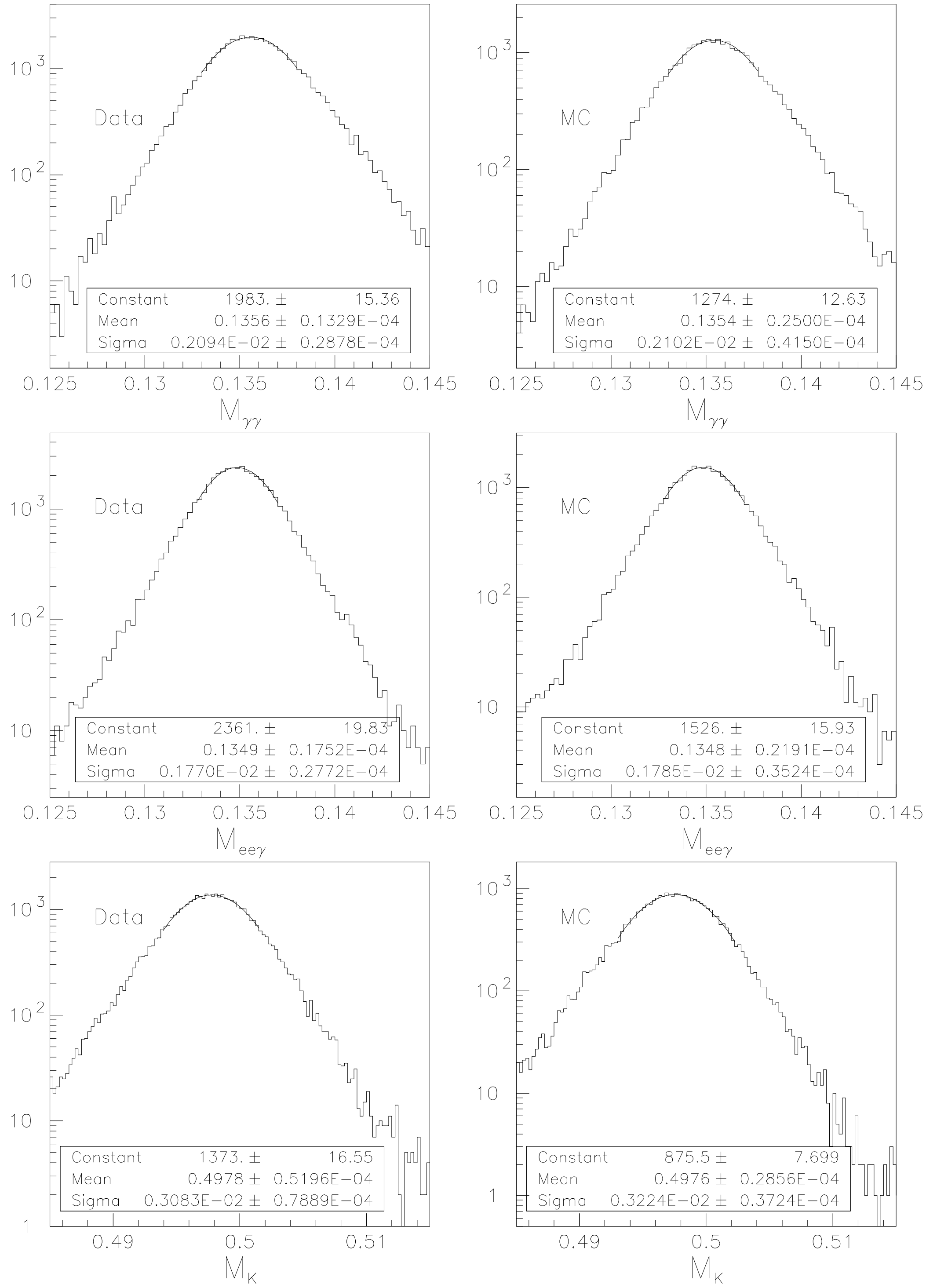

Figure 6.16: Gaussian fits to the data and MC peaks in: (top row) $M_{\gamma\gamma}$, (middle row) $M_{ee\gamma}$, and (bottom row) M_K. All other cuts are applied.

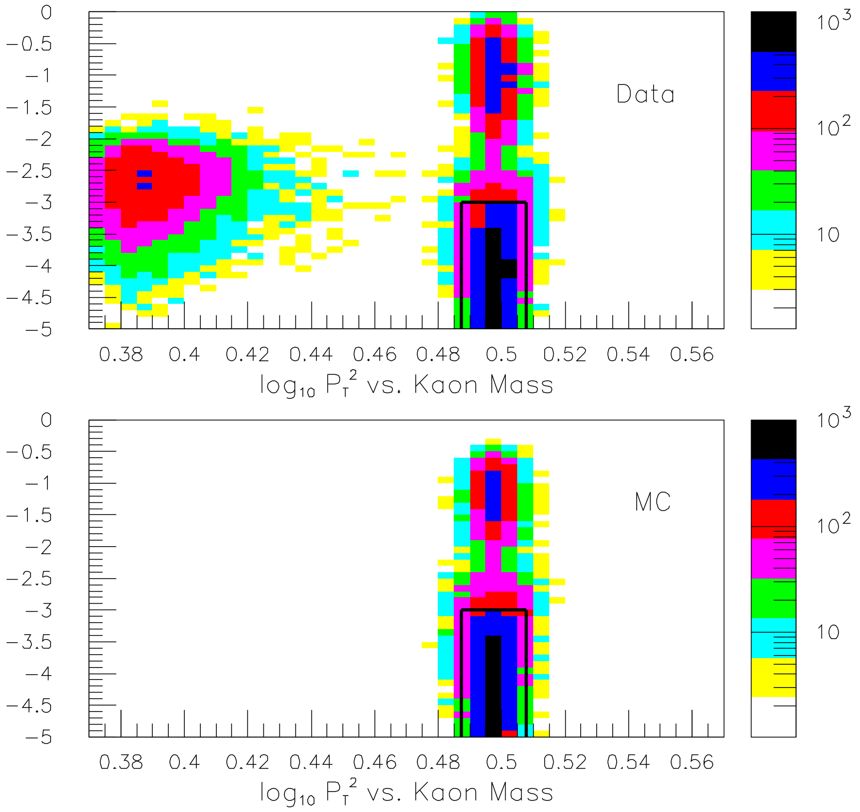

Figure 6.17: Distribution of $\log_{10}\mathrm{P}_\mathrm{T}^2$ vs. the reconstructed kaon mass in data and MC, using the neutral vertex. Besides the charged vertex P_T^2 cut, all other cuts are applied. The region ultimately accepted by the selection cuts is outlined by the box. The events with the correct kaon mass but with high $\log_{10}\mathrm{P}_\mathrm{T}^2$ are from kaons that scatter and regenerate in the defining collimator. (Top) Data. The events in the upper left are mostly $K_L \to \pi^0\pi^0\pi^0_D$ decays where two of the photons are not reconstructed. (Bottom) MC.

where two photons are not reconstructed. The background is estimated by fitting an exponential between 420 and 470 MeV/c^2, and then integrating this function over the accepted region. This results in a background of 11.8 events, which is very small, essentially negligible, compared to the total number of events accepted.

The bottom row of plots in Figure 6.16 show the Gaussian fits to the peaks in data and MC. The correspondence between the data and MC means and widths is good. The $M_{\gamma\gamma ee\gamma}$ selection requirement is that $|M_{\gamma\gamma ee\gamma}$ - M_{K^0} $| < 10$ MeV/c^2.

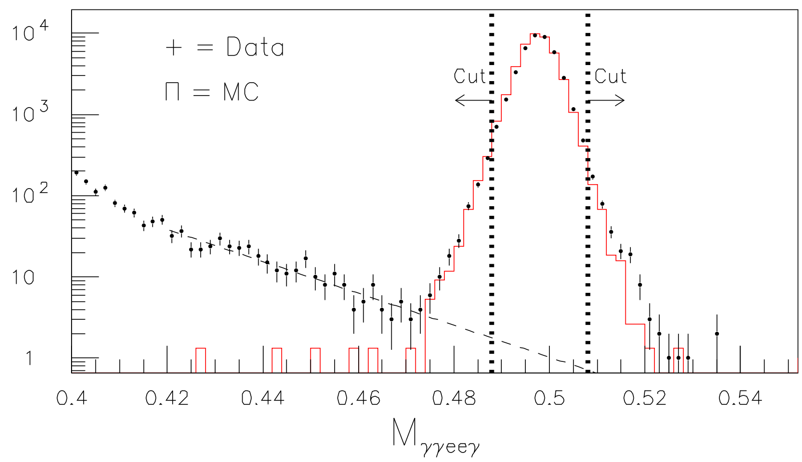

Figure 6.18: Distribution in data and MC of $M_{\gamma\gamma ee\gamma}$. All other cuts are applied.

6.6 The Normalization Mode Flux

6.6.1 The Flux Calculation

The normalization sample is very clean. Figure 6.18 shows that the number of background events in the interpolation of the $M_{\gamma\gamma ee\gamma}$ sidebands into the signal region is negligible at 11.8 events.

The flux calculation is presented in Table 6.5. The uncertainties listed include only statistical and branching ratio.

	Number	Uncertainty	Relative Uncertainty
No. Generated	9,999,888	—	—
In good spills	9,941,663	—	—
Weighted by $\mathrm{K_L}$ fraction	4,825,750	1,531	0.03%
MC events passing all cuts	32,203.2	—	—
TRD acceptance	0.8850	0.0014	0.16%
Total MC acceptance	0.005906	0.000035	0.59%
Br ($K_L \to \pi^0\pi^0$)	0.000927	0.000019	2.05%
Br ($\pi^0 \to ee\gamma$)	0.011980	0.000320	2.67%
Br ($K_L \to \pi^0\pi^0$, $\pi^0 \to \gamma\gamma$, $\pi^0 \to ee\gamma$)	2.194×10^{-5}	7.39×10^{-7}	3.37%
Data passing all cuts	45,274	213	0.47%
Flux ($\times$ $\mathbf{10^{11}}$)	3.493	0.121	3.45%

Table 6.5: Components in the flux calculation, with associated uncertainties.

6.6.2 Systematic Uncertainties

The systematic uncertainties are evaluated by varying the individual cuts and observing the resulting change in flux. Table 6.6 lists these changes.

The systematic effects embodied in the cut variations dominate the flux uncertainty. Fortunately, flux systematics of $K_L \to \pi^0\pi^0_D$ which are in common with the signal $K_L \to \pi^0 e^+e^-$ mode will cancel out when calculating the branching ratio, but those systematics not in common with the signal mode will have to be added as uncertainties on the branching ratios, including the systematic uncertainty in the cut in $\mathrm{M}_{ee\gamma}$. A table of the uncertainties are listed in Table 6.7. For this analysis, the relevant uncertainty is the quadrature sum of the flux uncertainties from statistics, BR, and varying the $\mathrm{M}_{ee\gamma}$ cut.

Change to Cuts	Δ(Flux) $\times 10^9$
Remove VV' cuts	-1.08
Tighten CA energy cut to < 1 GeV	-4.00
Remove ETOT verification cut	-1.32
Remove cluster energy cut	-7.06
Remove cluster-hole distance (HOLEDIST) cut	+0.24
Remove TRD cut	-0.03
Tighten E/p cut to 0.96 < E/p < 1.04	-3.78
Remove track separation at CsI cut	+0.03
Remove track separation in X at DC1 cut	-1.47
Remove track separation in Y at DC1 cut	-0.58
Loosen opening angle cut to 1.5 mrad	+5.96
Tighten $M_{\gamma\gamma}$ cut to 7 MeV	+0.56
Tighten $M_{ee\gamma}$ cut to 5 MeV	+0.93
Loosen $M_{\gamma\gamma ee\gamma}$ cut to 12 MeV	+0.31
Tighten P_T^2 cut to $P_T^2 < 0.0004$ (MeV/c)^2	+7.03
Tighten P cut to 40 < P < 160 (GeV/c)	-1.85
Total (quadrature sum)	12.69

Table 6.6: Systematic uncertainties in the flux measurement.

Type of Uncertainty	Δ(Flux) $\times 10^9$
Branching Ratio	11.76
Statistical	2.63
Cut Variations	12.69
BR + stat + $M_{ee\gamma}$ cut	12.09

Table 6.7: Summary of uncertainties on the flux. "BR + stat + $M_{ee\gamma}$ " is relevant to BR($K_L \to \pi^0 e^+ e^-$).

CHAPTER 7
THE SIGNAL MODE ANALYSIS

7.1 Monte Carlo Samples

1.5 million $K_L \rightarrow \pi^0 e^+ e^-$ and 20 million $K_L \rightarrow e^+ e^- \gamma\gamma$ are generated. The EEGG crunch filter tag is now used instead of EEGGG. A flat phase space model for the $K_L \rightarrow \pi^0 e^+ e^-$ decay is assumed. The vector model will be addressed in Section 7.9. Events are required to have four clusters and to pass the same basic reconstruction cuts as the normalization mode. Further cuts are explained in the following sections.

7.2 Basic Cuts

The signal $K_L \rightarrow \pi^0 e^+ e^-$ analysis is a blind analysis, so no data are used from the signal region while cuts are being finalized. In order to demonstrate how powerful cuts to remove specific background are, the following plots show distributions from data after all other cuts previously discussed are applied.

7.2.1 $M_{\pi^+\pi^-\pi^0}$ Cut

Figure 7.1 shows the distribution of the invariant mass of the particles, under the hypothesis that tracks are pions rather than electrons. This indicates that the EEGG sample is mainly $K_L \rightarrow \pi^+ \pi^- \pi^0$ at this point. A cut requiring that $M_{\pi^+\pi^-\gamma\gamma} > 520$ MeV/c^2 removes the majority of these events.

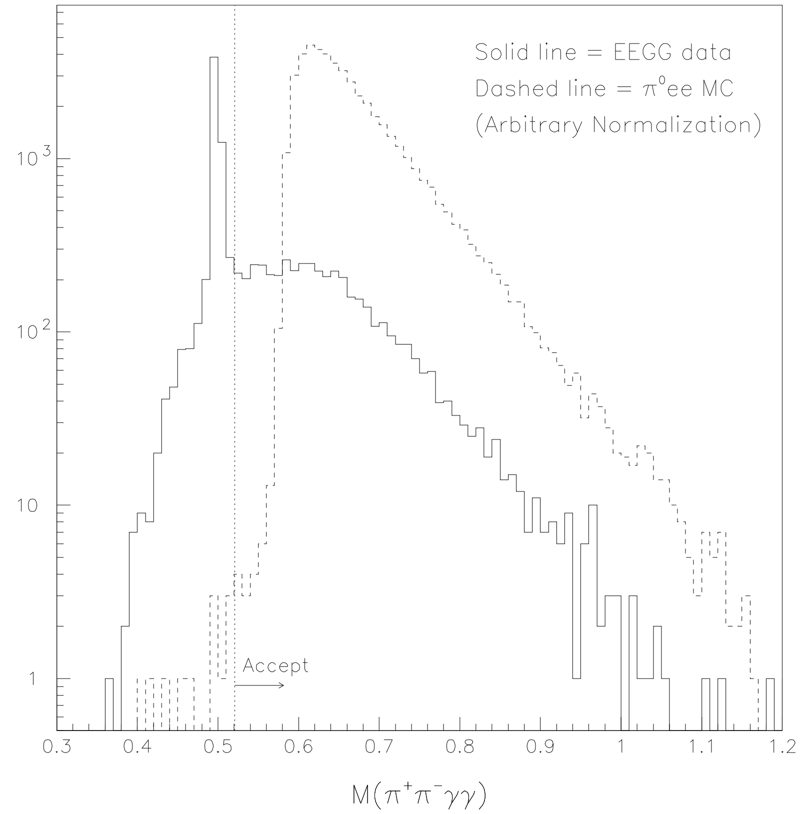

Figure 7.1: Distribution of the $\pi^+\pi^-\gamma\gamma$ invariant mass. General reconstruction cuts not involving the TRD have been applied.

7.2.2 TRD Cut

Residual K_{e3} decays accompanied by either accidental acivity or radiated photons may be removed through the TRDLIKE cut described in Section 6.4.7. This cut is imposed on both tracks.

7.2.3 M_{ee} Cut

Figure 7.2 shows the distribution in M_{ee} for data and MC. Most data events at this point is background from $K_L \to \pi^0\pi^0_D$. These π^0_D backgrounds can be removed by applying a cut on M_{ee} : 140.0 MeV < M_{ee} < 362.7 MeV/c^2. The high-end cut is set at the kinematic bound, M_{K^0} - M_{π^0}, and the low-end cut is set at $+3\sigma$ from the M_{ee} peak in the KTeV $\pi^0 \to e^+e^-$ analysis [46].

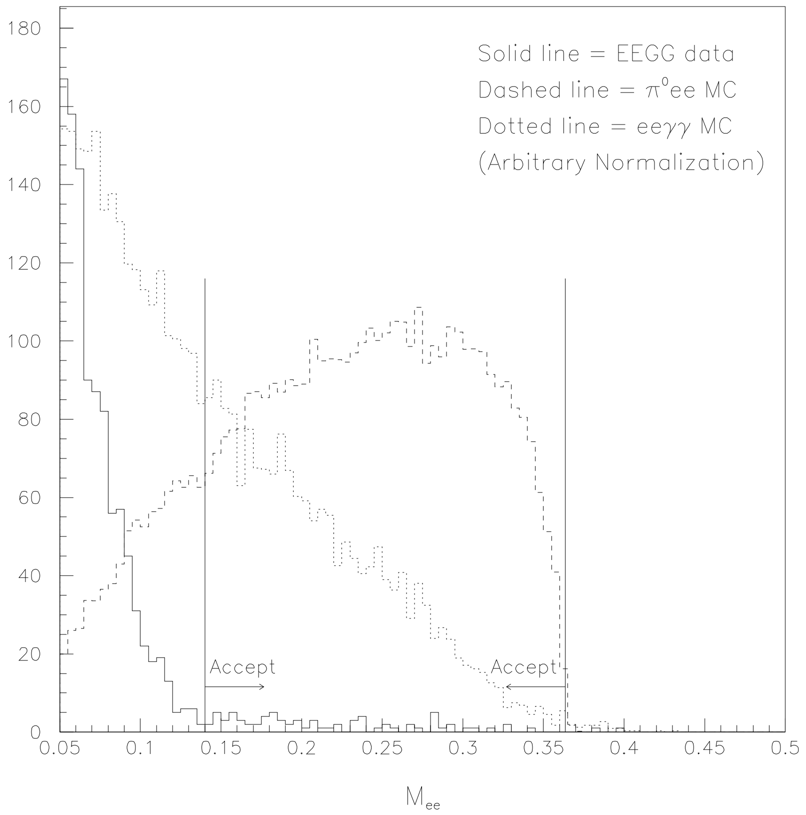

Figure 7.2: M_{ee}. All other general reconstruction cuts as well as the $M_{\pi^+\pi^-\pi^0}$ and TRD cuts have been applied.

7.3 Phase Space Fiducial Cuts

The phase space for the decay $K_L \to \pi^0 e^+e^-$ $(\pi \to \gamma\gamma)$ has five independent dimensions if the photon pair mass is permitted to vary. Two decay angles are particularly powerful in discriminating between the signal $K_L \to \pi^0 e^+e^-$ and the largest background, $K_L \to e^+e^-\gamma\gamma$. These variables are described below.

7.3.1 $|cos(\theta_{\pi^0})|$

$|\cos(\theta_{\pi^0})|$ is the cosine of the angle between a photon and the vector defined by the electron-pair in the center of mass of the photon pair. See Figure 7.3. The quantity $|\cos(\theta_{\pi^0})|$ is the same as the Greenlee variable $|y_\gamma|$ [33]. However, since $|y_\gamma|$ is by definition symmetric about zero, it is often denoted $|\cos(\theta_{\pi^0})|$.

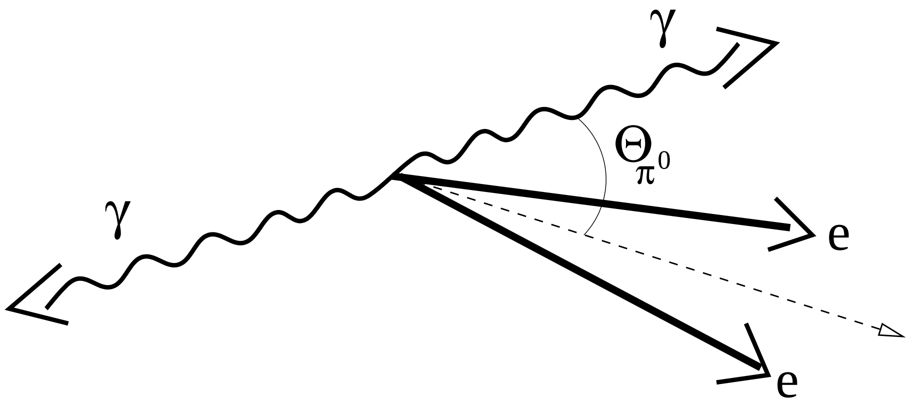

Figure 7.3: Definition of $|\cos(\theta_{\pi^0})|$.

7.3.2 θ_{min}

θ_{min} is the minimum angle between any photon and any electron in the kaon rest frame. See Figure 7.4.

Section 7.5 discusses the differences in the $|\cos(\theta_{\pi^0})|$ and θ_{min} profiles between $K_L \to \pi^0 e^+ e^-$ and $K_L \to e^+ e^- \gamma\gamma$ and shows why these variables have good separation power between signal and background.

7.4 The $M_{\gamma\gamma}$ vs. $M_{ee\gamma\gamma}$ Plane

The $M_{\gamma\gamma}$ vs. $M_{ee\gamma\gamma}$ plane is used to estimate background for different combinations of angle cuts. This estimate is made by fitting the data outside the blind signal region and interpolating into the region. The resulting estimate is then used to calculate a branching ratio confidence interval. The optimal cuts are those that would give the lowest upper limit in the absence of signal.

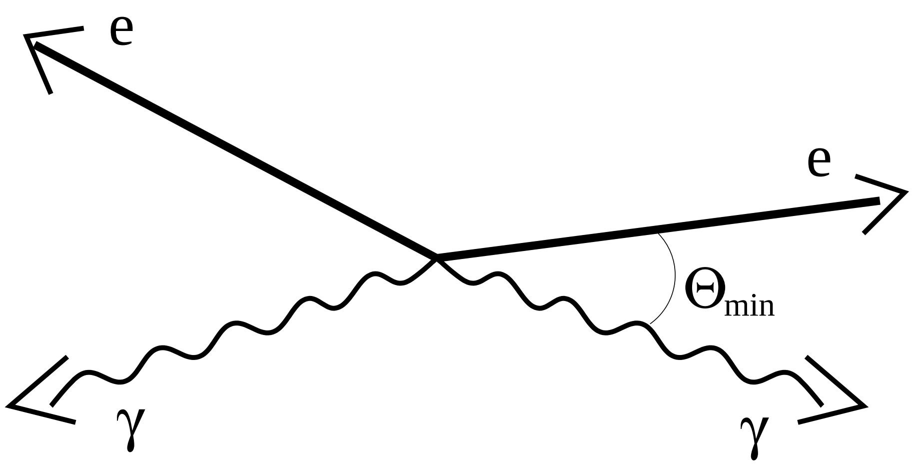

Figure 7.4: Definition of θ_{min} .

Signal in the $M_{\gamma\gamma}$ vs. $M_{ee\gamma\gamma}$ plane would in the ideal case of infinite detector resolution be localized to one point at (M_K, M_{π^0}). Practically speaking, of course, the signal is smeared by detector resolution effects.

Figure 7.5 shows the distribution in $M_{\gamma\gamma}$ vs. $M_{ee\gamma\gamma}$ for data events outside of the signal region and passing all previous cuts. Figure 7.6 shows the distribution for $e^+e^-\gamma\gamma$ MC. There are several regions of interest. The "box" is the region covered up until all cuts are finalized. It is defined by the pair of equations $130 < M_{\gamma\gamma} <$ 140 MeV/c^2 and $485 < M_{ee\gamma\gamma} < 510$ MeV/c^2. The "bump" is the signal region. It is a subset of the box containing $K_L \to \pi^0 e^+e^-$ candidates. The "swath" is the region where most $K_L \to e^+e^-\gamma\gamma$ appear. It is diagonal because the charged vertex $M_{\gamma\gamma}$ is plotted versus the neutral vertex $M_{ee\gamma\gamma}$: when $M_{\gamma\gamma}$ is greater than M_{π^0}, the neutral vertex is shifted from the charged vertex to reduce $M_{\gamma\gamma}$, which also results in $M_{ee\gamma\gamma}$ being decreased. When $M_{\gamma\gamma}$ is lower than M_{π^0}, the neutral vertex is shifted to increase $M_{\gamma\gamma}$ and $M_{ee\gamma\gamma}$. Finally, the "strip" contains fragments from $K_L \to \pi^0\pi^0\pi^0_D$ decay and $K_{e3}+\pi^0$. It covers the region $M_{ee\gamma\gamma} < 465$ MeV/c^2 and 130 MeV/c^2 $< M_{\gamma\gamma} <$ 140 MeV/c^2.

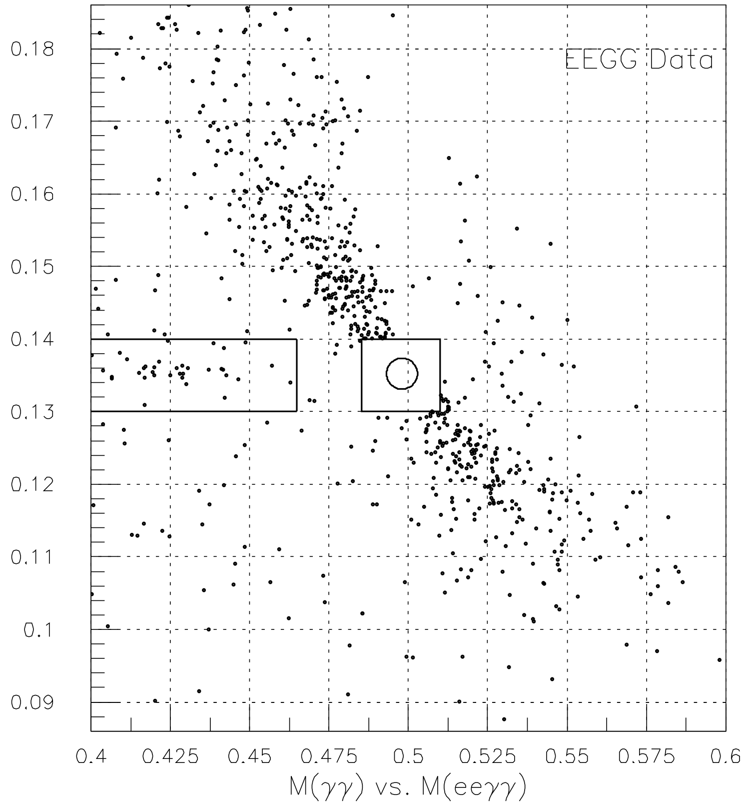

Figure 7.5: $\mathrm{M}_{\gamma\gamma}$ vs. $\mathrm{M}_{ee\gamma\gamma}$ for EEGG data subsequent to application of all selection criteria except the phase space fiducial cuts.

7.4.1 The Bump

The location of the bump may be anywhere within the box because no events in the box are used for studies while the analysis is still blind, which is the case while the last signal selection cuts, the phase space fiducial cuts, are being finalized. The optimum location for the bump, however, is obviously where the $K_L \to \pi^0 e^+ e^-$ signal is strongest. Therefore, the center of the bump is placed at the center of the peaks in $\mathrm{M}_{ee\gamma\gamma}$ and $\mathrm{M}_{\gamma\gamma}$ for $K_L \to \pi^0 e^+ e^-$ MC. The bump is actually an ellipse with the widths of the $\mathrm{M}_{ee\gamma\gamma}$ and $\mathrm{M}_{\gamma\gamma}$ distributions, doubled, as its radii. Figure 7.7 shows the distributions of $\mathrm{M}_{ee\gamma\gamma}$ and $\mathrm{M}_{\gamma\gamma}$ for $K_L \to \pi^0 e^+ e^-$ MC.

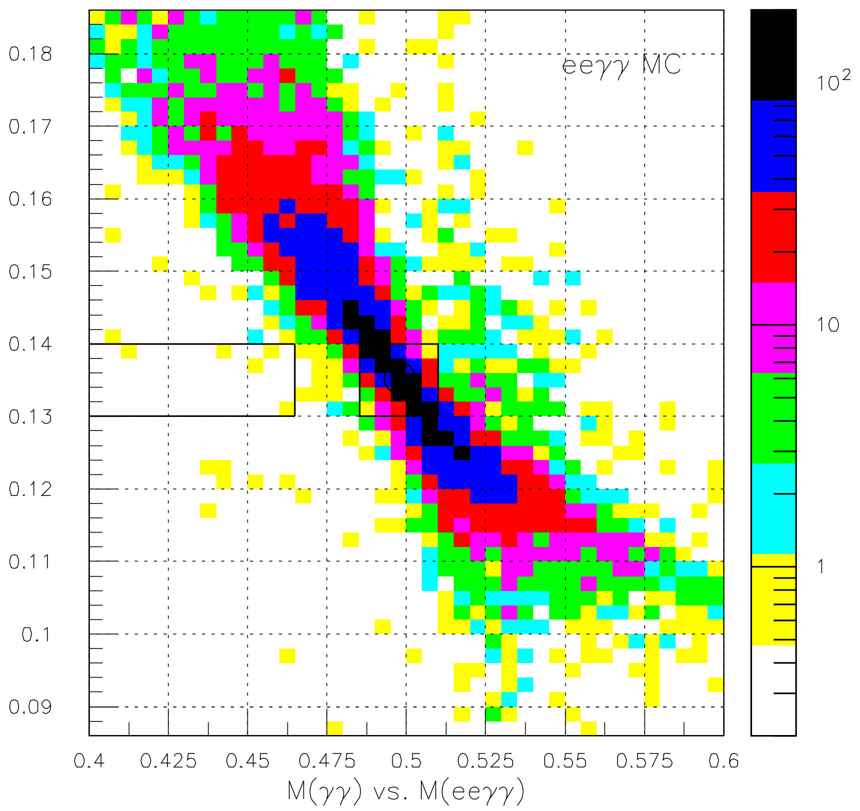

Figure 7.6: $M_{\gamma\gamma}$ vs. $M_{ee\gamma\gamma}$ for $e^+e^-\gamma\gamma$ MC subsequent to application of all selection criteria except the phase space fiducial cuts.

Fitting Gaussians to these variables yields the values listed in Table 7.1.

	Mean	Width
$M_{ee\gamma\gamma}$	497.69 ± 0.03 MeV/c^2	2.51 ± 0.04 MeV/c^2
$M_{\gamma\gamma}$	135.31 ± 0.01 MeV/c^2	1.16 ± 0.01 MeV/c^2

Table 7.1: Parameters of the $M_{ee\gamma\gamma}$ and $M_{\gamma\gamma}$ peaks for $K_L \to \pi^0 e^+ e^-$ MC.

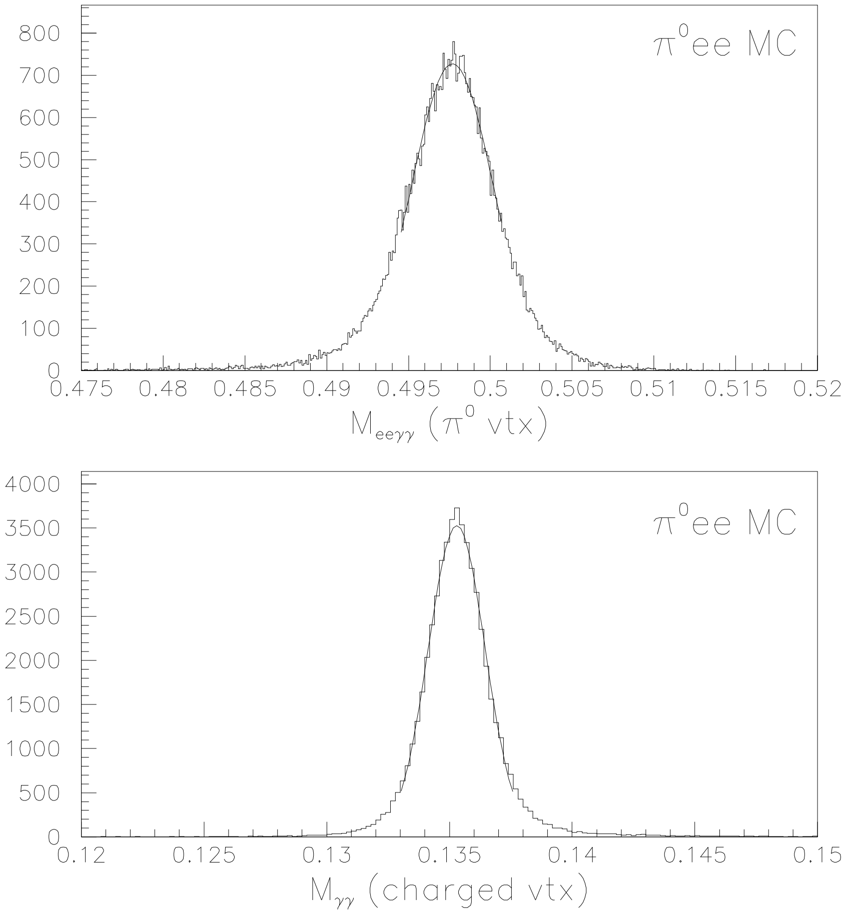

Figure 7.7: $M_{ee\gamma\gamma}$ and $M_{\gamma\gamma}$ spectra for $K_L \to \pi^0 e^+ e^-$ MC subsequent to application of all selection criteria other than the phase space fiducial cuts.

7.4.2 Background Estimation

To determine the background inside the bump, the data outside the box are fit to a function that is the sum of a plane and the $K_L \to e^+e^-\gamma\gamma$ sample:

$$\mathrm{f}\,(\mathrm{M}_{ee\gamma\gamma}\,,\mathrm{M}_{\gamma\gamma}\,) = \mathrm{A}_0 + \mathrm{A}_{\gamma\gamma}\mathrm{M}_{\gamma\gamma} + \mathrm{A}_{ee\gamma\gamma}\mathrm{M}_{ee\gamma\gamma} + \mathrm{A}_g\ \mathrm{g}(\mathrm{M}_{ee\gamma\gamma}\,,\ \mathrm{M}_{\gamma\gamma}\,)$$

where $\mathrm{g}(\mathrm{M}_{ee\gamma\gamma}\,,\mathrm{M}_{\gamma\gamma}\,)$ is the $e^+e^-\gamma\gamma$ MC distribution. The values of the parameters A_i are determined from the log-likelihood fit. Neither the planar nor the $K_L \to$

$e^+e^-\gamma\gamma$ contributions are allowed to be negative. The strip and box regions are restricted from the fit. Figure 7.8 compares the background fit with the data outside the box. The estimated background is found to be 38.11 $\pm$ 1.67 events where only 0.27 $\pm$ 0.03 events come from the plane.

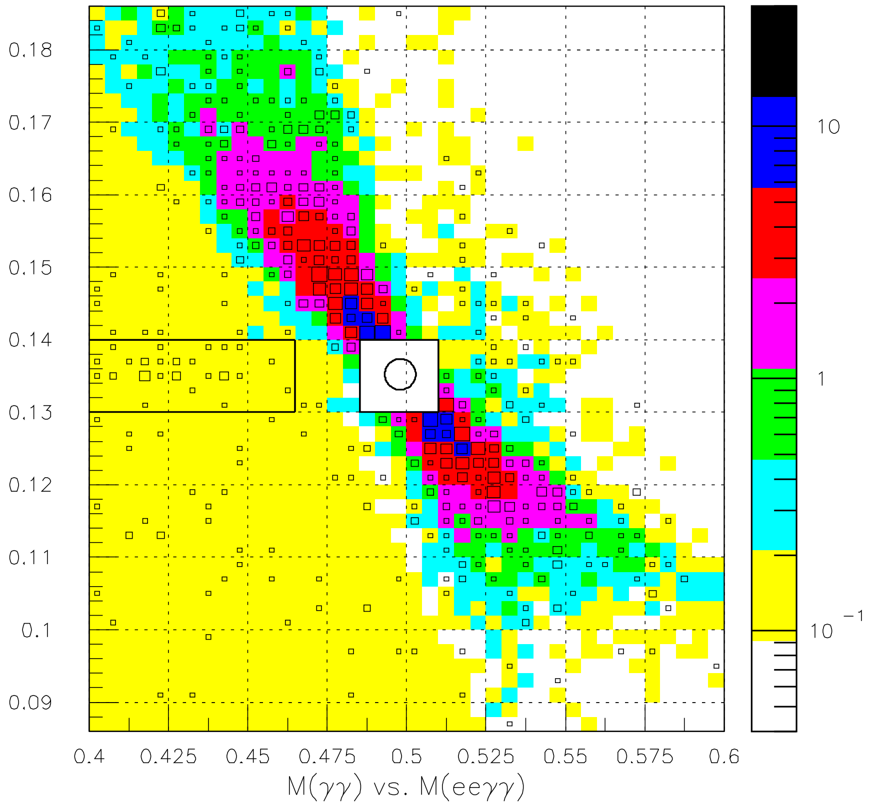

Figure 7.8: $M_{ee\gamma\gamma}$ vs. $M_{\gamma\gamma}$ for the background fit and the EEGG data. The shaded squares represent the fit on a logarithmic Z scale. The empty boxes show the data on a linear scale.

7.5 Further Checks of the $e^+e^-\gamma\gamma$ Background

The background estimate shows that $K_L \to e^+e^-\gamma\gamma$ is by far the largest background. In this section, comparisons are made between the $e^+e^-\gamma\gamma$ background and the

EEGG data. Since the analysis is blind, only events outside the box are used. To maintain high purity for $e^+e^-\gamma\gamma$, events are taken from within the swath region.

Figure 7.9 shows the projection of the swath onto the $M_{\gamma\gamma}$ and $M_{ee\gamma\gamma}$ axes. The figures show that the distribution of EEGG data outside the box is well modeled by the $e^+e^-\gamma\gamma$ background fit.

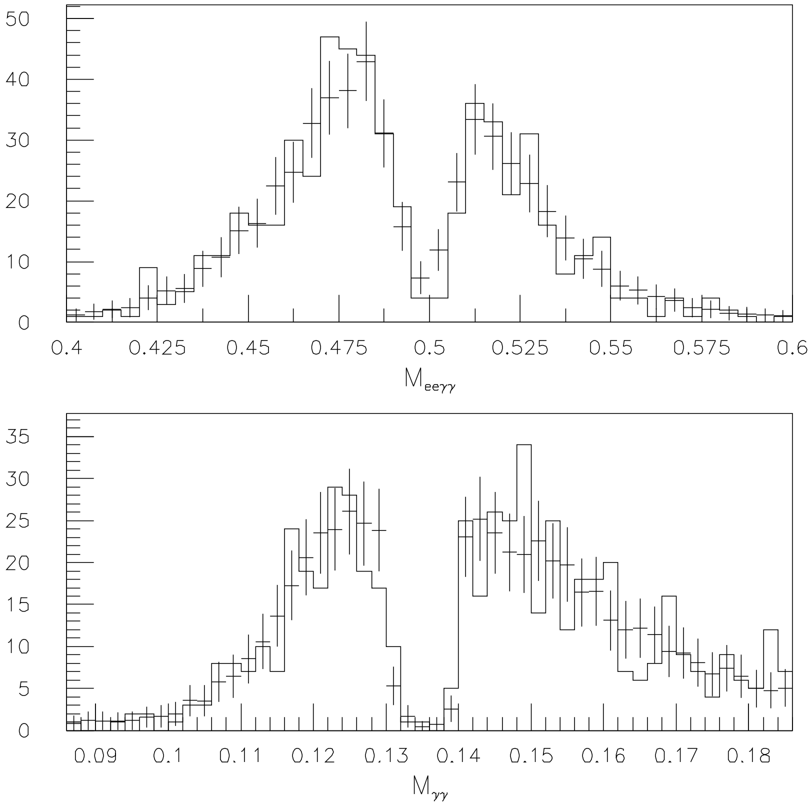

Figure 7.9: Projections of the "swath" region onto the $M_{\gamma\gamma}$ and $M_{ee\gamma\gamma}$ axes. The top plot is the $M_{ee\gamma\gamma}$ distribution, and the bottom plot is $M_{\gamma\gamma}$. The solid line is the EEGG data and the labels with error bars represent the fit.

Figures 7.10 and 7.11 compare the distributions in $|y_\gamma|$ and θ_{min}, respectively, for $K_L \to e^+e^-\gamma\gamma$ data and MC outside the box but within the swath region. Here, the $K_L \to e^+e^-\gamma\gamma$ MC has been normalized with the coefficient coming from the background fit in the previous section. These figures show that there is good data and MC agreement in $K_L \to e^+e^-\gamma\gamma$ for the swath region outside of the box. The plots also show that the $K_L \to \pi^0 e^+e^-$ $|y_\gamma|$ and θ_{min} distributions are much flatter than for $K_L \to e^+e^-\gamma\gamma$. This property forms the rationale for making selection cuts in these variables, a topic that will be discussed in the following section.

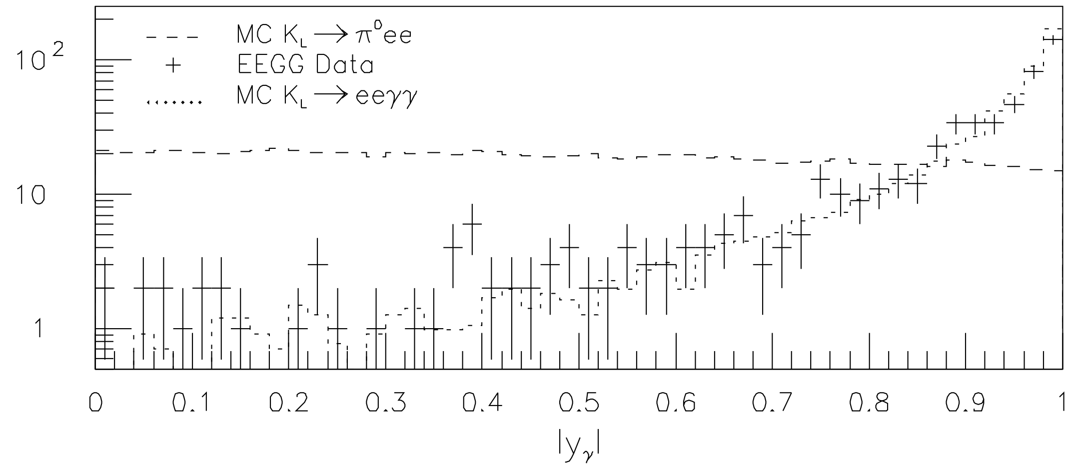

Figure 7.10: $|y_\gamma|$ distributions for $K_L \to \pi^0 e^+e^-$ MC and $K_L \to e^+e^-\gamma\gamma$ data and MC. $K_L \to e^+e^-\gamma\gamma$ events come from inside the swath but outside the box. $K_L \to \pi^0 e^+e^-$ MC are from inside the box and the normalization is arbitrary.

7.6 Optimizing the Kinematic Cuts

The approximately 38 events in the background fit of section 7.4.2 can be reduced significantly by cutting on the phase space fiducial variables θ_{min} and $|y_\gamma|$. The optimal values for these cuts are determined by iterating a specific algorithm over a pre-determined set of cut values to evaluate their performance. The figure-of-merit used here is the expected branching ratio upper limit in the absence of signal. A particular cut combination is applied to data (outside of the box and strip regions), the $K_L \to \pi^0 e^+e^-$ MC, and the $K_L \to e^+e^-\gamma\gamma$ MC. The resulting $K_L \to e^+e^-\gamma\gamma$

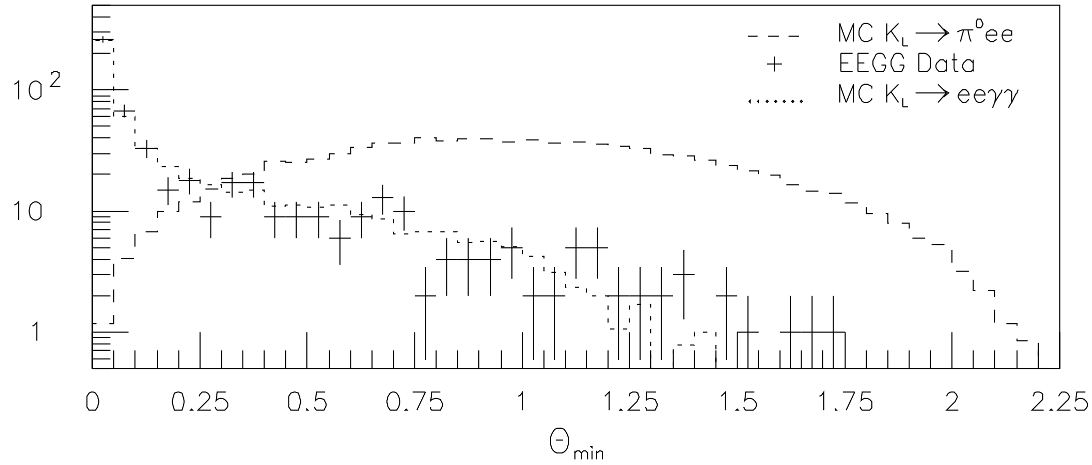

Figure 7.11: θ_{min} distributions for $K_L \to \pi^0 e^+e^-$ MC and $K_L \to e^+e^-\gamma\gamma$ data and MC. $K_L \to e^+e^-\gamma\gamma$ events come from inside the swath but outside the box. $K_L \to \pi^0 e^+e^-$ MC are from inside the box and the normalization is arbitrary.

MC background distribution is fit to the data in order to determine the mean and error of the $e^+e^-\gamma\gamma$ background contribution.

The number of events passing the cuts is assumed to come from a Poisson distribution with parameter equal to the background mean value. The 90% confidence level upper limit on the number of signal events is subsequently calculated. The expected branching ratio upper limit is then simply this upper limit on the number of signal events, divided by the product of flux and acceptance:

$$UL_i = \frac{\mu_i}{N_{K_L} \cdot \epsilon} \tag{7.1}$$

The effect of the uncertainty in the background estimate is included in the analysis. This is done by integrating over a Gaussian probability distribution function representing the background mean value and uncertainty, although the corrections are negligible for most cut combinations. Appendix B of Reference [38] discusses the algorithm in greater detail.

The methodology used for this analysis for interval construction is the approach advocated by Feldman and Cousins [69] for analyzing small signals in the particular case of a Poisson process with background.

The optimization runs over a grid of selection cut values for minimum θ_{min} and maximum $|y_\gamma|$. The 90% CL upper limit to the number of events is found to be described well by the function $N_{UL} = 2.44 + 0.834(\mu_{backgnd})^{0.794}$, for $\mu_{backgnd} \leq 5$. Since most angle cut combinations resulted in a predicted background level of less than 5, this equation is used as the figure-of-merit to determine the optimal cuts. Figure 7.12 shows the expected branching ratio upper limit as a function of the cut pair.

A two-dimensional quadratic function fit to the points around the minimum indicates the optimal cuts values to be at $\theta_{min} > 0.362 \pm 0.017$ and $|y_\gamma| < 0.745 \pm 0.002$, where the errors come from the fit. The expected background level is then reduced from a level of 38.11 ± 1.67 events with no cuts to 0.99 ± 0.35 with the above angle cuts. The 90% CL upper limit on the number of signal events is expected to be 3.27 events. The signal acceptance is $(2.749 \pm 0.013)\%$. With the single-event sensitivity at 1.04×10^{-10}, the 90% C.L. BR upper limit is 3.41×10^{-10}.

7.7 Interpreting the Predicted Upper Limit Estimate

The expected 90% CL branching ratio upper limit estimate is theoretically the average over an infinitely large ensemble of KTeV experiments with the same detector performance parameters and data profile. The expected 90% CL branching ratio upper limit at 3.41×10^{-10} is simply a weighted average over the upper limit that would result from finding a certain integrally-quantized number of events in the bump, in the limit that the entire KTeV experiment is repeated an infinite number of times. In particular, if 0 events were found, the 90% CL branching ratio upper limit would be 1.67×10^{-10}; in the case of 1 event, the number would be 3.50×10^{-10}; and in the case of 2 events, it would be 5.13×10^{-10}. Finding 3 or more events in the signal region would indicate that the 90% CL lower limit for the signal branching ratio is greater than zero.

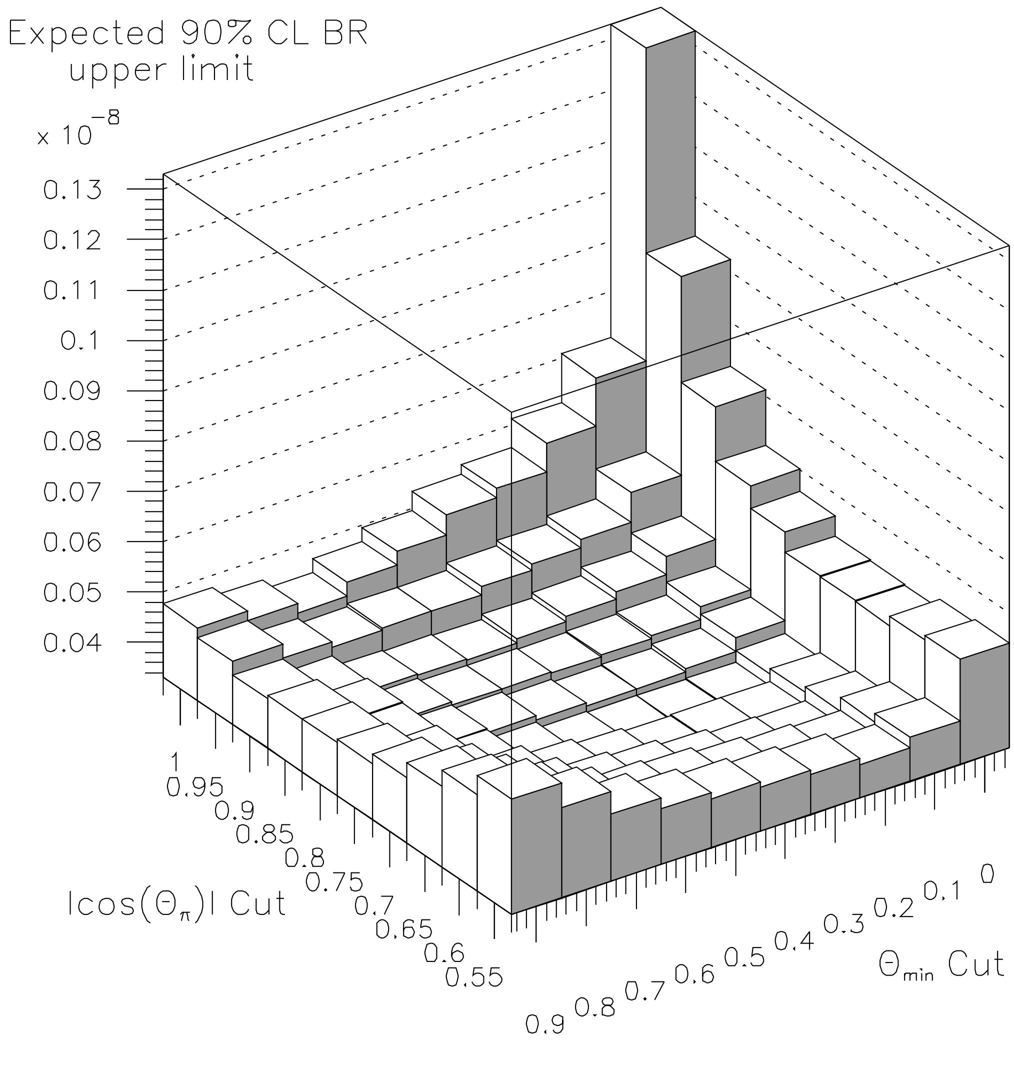

Figure 7.12: The estimated 90% CL branching ratio upper limit, as a function of the applied cuts in θ_{min} and $|\cos(\theta_{\pi^0})|$. The Feldman-Cousins interval construction procedure is used.

7.8 Result

When the box in Figure 7.5 is opened, one event is observed in the signal ellipse (Figure 7.13). Taking into account the background level and the uncertainty in this number, it is determined that BR($K_L \to \pi^0 e^+ e^-$) $< 3.50 \times 10^{-10}$ at 90% C.L.

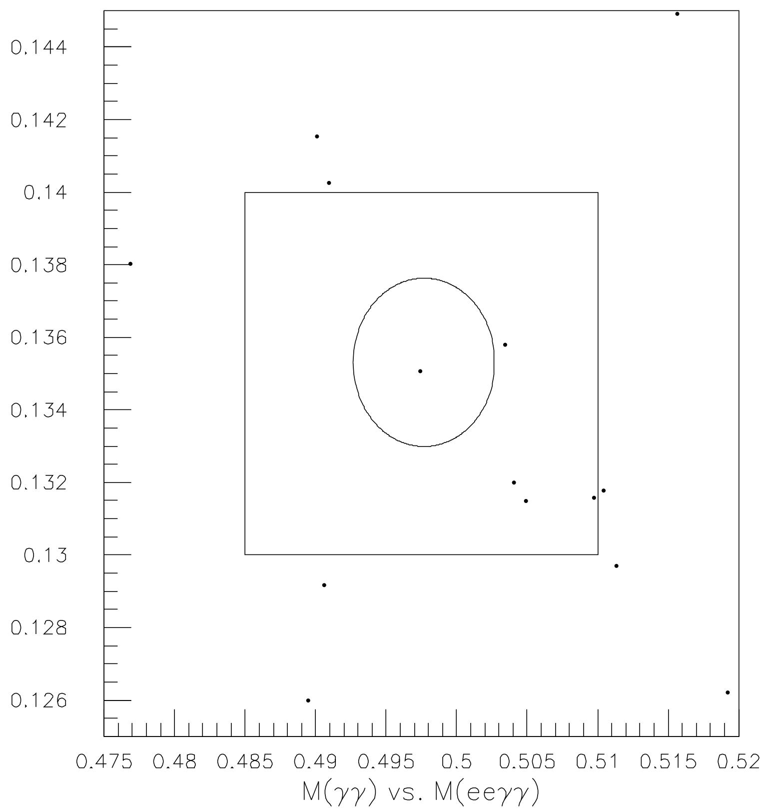

Figure 7.13: $M_{\gamma\gamma}$ vs. $M_{ee\gamma\gamma}$ in GeV/c^2 for the data after all cuts have been applied. The box is open and one event appears within the signal ellipse.

7.9 The Vector Model and CKM η Limit

The vector model is now assumed for the direct CP-violating part of the decay. The vector model is used in KTEVMC. The above optimization process is repeated. Figure 7.14 shows the expected branching ratio upper limit as a function of the cut pair. After finding the minimum using the quadratic fit, we observe there to be no distinct advantage to changing the cuts above.

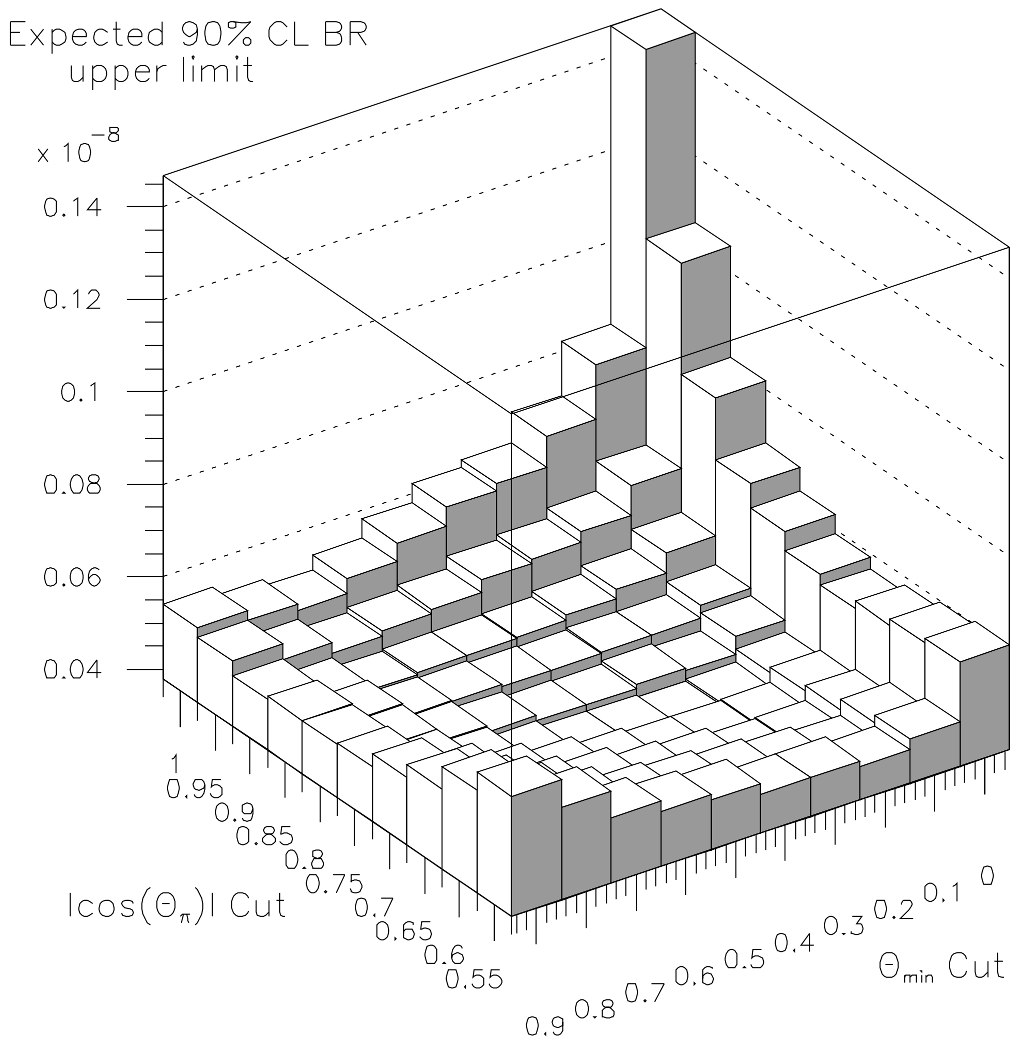

Figure 7.14: The estimated 90% CL branching ratio upper limit, as a function of the applied cuts in θ_{min} and $|\cos(\theta_{\pi^0})|$. This figure assumes the vector model for $K_L \to \pi^0 e^+ e^-$.

The signal acceptance is $(2.370 \pm 0.013)\%$. With the single-event sensitivity at 1.21×10^{-10}, an ensemble of many KTeVs is expected to produce an average BR upper limit of 3.95 $\times 10^{-10}$ at 90% C.L. Observation of one event in the signal region leads to a BR upper limit of 4.06 $\times 10^{-10}$ at 90% C.L. If we assume that most of the decay of $K_L \rightarrow \pi^0 e^+ e^-$ is through the direct CP-violating part, we can deduce an upper limit for $|\eta|$. First, we use the Wolfenstein parametrization to relate the directly CP-violating component of $K_L \rightarrow \pi^0 e^+ e^-$ to CKM parameters [16]:

$$Br(K_L \rightarrow \pi^0 e^+ e^-)_{DIR} = 4.16(y_{7A}^2 + y_{7V}^2)(\mathrm{Im}\lambda_t)^2, \tag{7.2}$$

$$\mathrm{Im}\lambda_t = |V_{cb}|^2 |V_{us}| \eta. \tag{7.3}$$

Using the PDG values for $|V_{cb}|$, $|V_{us}|$, the mass of the top quark, and the values of y_{7A}^2 and y_{7V}^2 estimated from tables in Reference [16], we find $|\eta| < 3.49$ at the 90% C.L.

Although measurements on B decays yield a more competitive constraint on the CKM matrix, it is important to make measurements on the neutral kaon system in order to make sure that the B and K systems can be described theoretically in the same way under the CKM parametrization.

CHAPTER 8
CONCLUSION

8.1 Summary of Results

The decay $K_L \rightarrow \pi^0 e^+ e^-$ has been searched for in the 1999-2000 dataset of the KTeV/E799 collaboration at Fermilab. One event is observed at an expected background level of 0.99 ± 0.22 events, originating mainly from $K_L \rightarrow e^+ e^- \gamma\gamma$ decays. Assuming a uniform phase space distribution for the signal mode, the branching ratio upper limit has been measured to be 3.5×10^{-10} at the 90% confidence level. Combining with the previous result [32] based on the dataset taken by KTeV in 1997 yields $\mathrm{BR}(K_L \rightarrow \pi^0 e^+ e^-) < 2.1 \times 10^{-10}$ at 90% confidence level. If a vector dominance model for the direct CP-violating part of the decay is assumed instead, the branching ratio upper limit is determined to be 4.1×10^{-10} at the 90% confidence level.

8.2 Prospects

Future experiments must collect more K_L decays. Better suppression of the largest background, $K_L \rightarrow e^+ e^- \gamma\gamma$, is also required. Since the two photons in $K_L \rightarrow \pi^0 e^+ e^-$ have invariant mass equal to M_{π^0} , while the two photons from $K_L \rightarrow e^+ e^- \gamma\gamma$ do not, advances in precision calorimetry leading to enhancements in the detector resolution of $\mathrm{M}_{\gamma\gamma}$ can greatly increase discriminatory power between $K_L \rightarrow \pi^0 e^+ e^-$ and the $K_L \rightarrow e^+ e^- \gamma\gamma$ background. Improvements in pion-electron identification, as with an upgraded TRD system, are also important for suppressing less severe backgrounds. Since the Standard Model prediction for $\mathrm{BR}(K_L \rightarrow \pi^0 e^+ e^-)$ is $O(10^{-12})$ and may possibly be increased to only about $O(10^{-11})$ by theories extending the

Standard Model, sensitivity must improve by at least one or two orders of magnitude in order to approach any predicted branching ratios. There are indeed challenges ahead for uncovering the mysteries of CP-violation in $K_L \to \pi^0 e^+ e^-$.

REFERENCES

[1] T. D. Lee and C. N. Yang, *Phys. Rev.* **104**, 254 (1956).

[2] C. S. Wu *et al.*, *Phys. Rev.* **105**, 1413 (1957).

[3] R. L. Garwin, L. M. Lederman, and M. Weinrich, *Phys. Rev.* **105**, 1415 (1957).

[4] J. I. Friedman and V. L. Telegdi, *Phys. Rev.* **105**, 1681 (1957).

[5] J. H. Christenson, J. W. Cronin, V. L. Fitch, and R. Turlay, *Phys. Rev. Lett.* **13**, 138 (1964).

[6] M. Kobayashi, *Prog. Theor. Phys.* **49**, 652 (1973).

[7] A. D. Sakharov, *JETP Lett.* **5**, 24 (1967).

[8] J. W. Cronin, *Rev. Mod. Phys.* **53**, 373 (1981).

[9] V. L. Fitch, *Rev. Mod. Phys.* **53**, 367 (1981).

[10] V. L. Fitch, R. F. Roth, J. S. Russ, and W. Vernon, *Phys. Rev. Lett.* **15**, 73 (1965).

[11] D.E. Groom *et al.* (PDG), *The European Physical Journal* **C15**, 1 (2002).

[12] L.-L. Chau and W.-Y. Keung, *Phys. Rev. Lett.* **53**, 1802 (1984).

[13] L. Wolfenstein, *Phys. Rev. Lett.* **51**, 1945 (1983).

[14] C. O. Dib, I. Dunietz, and F. J. Gilman, *Phys. Rev.* **D 39**, 2639 (1989).

[15] G. Ecker, A. Pich, and E. de Rafael, *Phys. Lett.* **B 237**, 481 (1990).

[16] J. F. Donoghue and F. Gabbiani, *Phys. Rev.* **D 51**, 2187 (1995).

[17] F. Gabbiani, Ph.D. thesis (University of Massachusetts at Amherst, September, 1997).

[18] A. Alavi-Harati *et al.* (KTeV Collaboration), *Phys. Rev. Lett.* **83**, 917 (1999).

[19] L. Iconomidou-Fayard. "Results on CP Violation from the NA48 Experiment at CERN". Lepton-Photon 2001 Conference, Rome, July 2001.

[20] A. Lai *et al.*, *Phys. Lett.* **B 514**, 253 (2001).

[21] G. Ecker, A. Pich, and E. de Rafael, *Nucl. Phys.* **B 303**, 665 (1988).

[22] G. D'Ambrosio, G. Ecker, G. Isidori, and J. Portoles, *Jour. High Ener. Phys* **9808**, 004 (1998).

[23] P. Ko, *Phys. Rev.* **D 44**, 139 (1991).

[24] G. Colangelo and G. Isidori, *Jour. High Ener. Phys.* **9809**, 009 (1998).

[25] A. J. Buras and L. Silvestrini, *Nucl. Phys.* **B 546**, 299 (1999).

[26] G. Isidori. Talk given at the International Workshop on CP Violation in K, KEK-Tanashi, Tokyo, December 18-19 1998.

[27] A. S. Carroll *et al.*, *Phys. Rev. Lett.* **44**, 525 (1980).

[28] L. K. Gibbons *et al.*, *Phys. Rev. Lett.* **70**, 1199 (1993).

[29] K. E. Ohl *et al.*, *Phys. Rev. Lett.* **64**, 2755 (1990).

[30] A. Barker *et al.*, *Phys. Rev.* **D 41**, 3546 (1990).

[31] D. A. Harris *et al.* (E799-I Collaboration), *Phys. Rev. Lett.* **71**, 3918 (1993).

[32] A. Alavi-Harati *et al.* (KTeV Collaboration), *Phys. Rev. Lett.* **86**, 397 (2001).

[33] H. Greenlee, *Phys. Rev.* **D 42**, 3724 (1990).

[34] A. Alavi-Harati *et al.* (KTeV Collaboration), *Phys. Rev. Lett.* **87**, 021801 (2001).

[35] J. F. Donoghue and F. Gabbiani, *Phys. Rev.* **D 56**, 1605 (1997).

[36] T. Kobilacik *et al.*, *KTeV Internal Memo 97.*

[37] P. Shawhan, *KTeV Internal Memo 257.*

[38] G. E. Graham, Ph.D. thesis (The University of Chicago, August, 1999).

[39] K. Arisaka *et al.*, *KTeV Design Report*, Technical Report FN-580, Fermilab, 1992.

[40] A. Roodman, in *Proceedings of the Seventh International Conference on Calorimetry in High Energy Physics*, edited by E. Cheu *et al.*, (World Scientific, Singapore, 1998), page 89.

[41] T. Barker and U. Nauenberg, *KTeV Internal Memo 102.*

[42] T. Barker and U. Nauenberg, *KTeV Internal Memo 132.*

[43] K. Hanagaki and T. Yamanaka, *KTeV Internal Memo 177.*

[44] S. Schnetzer *et al.*, *KTeV Internal Memo 191.*

[45] P. L. Mikelsons, Ph.D. thesis (The University of Colorado, December, 1999).

[46] E. D. Zimmerman, Ph.D. thesis (The University of Chicago, March, 1999).

[47] T. Barker, *KTeV Internal Memo 198.*

[48] T. Barker, *KTeV Internal Memo 199.*

[49] P. Mikelsons, *KTeV Internal Memo 201.*

[50] R. Kessler, *KTeV Internal Memo 361.*

[51] C. Bown *et al.*, *Nucl. Instrum. Methods Phys. Res., Sect. A* **369**, 248 (1996).

[52] L. Bellantoni, G. Graham, and P. Mikelsons, *KTeV Internal Memo 608.*

[53] P. Mikelsons, *KTeV Internal Memo 724.*

[54] P. Shawhan, *KTeV Internal Memo 328.*

[55] R. Ray, R. Tschirhart, and J. Whitmore, *KTeV Internal Memo 126.*

[56] P. S. Shawhan, Ph.D. thesis (The University of Chicago, December, 1999).

[57] A. Roodman, *KTeV Internal Memo 577.*

[58] A. J. Malensek, 1981. Fermilab Reports FN-341, FN-341A (errata).

[59] R. A. Briere, Ph.D. thesis (The University of Chicago, June, 1995).

[60] K. Hanagaki, Ph.D. thesis (Osaka University, 1998).

[61] N. Kroll and W. Wada, *Phys. Rev.* **98**, 1355 (1955).

[62] K. Mikaelian and J. Smith, *Phys. Rev.* **D 5**, 1763 (1972).

[63] K. Mikaelian and J. Smith, *Phys. Rev.* **D 5**, 2891 (1972).

[64] H. Behrend *et al.* *Z. Phys.* **C 49**, 401 (1991).

[65] H. Bethe, *Phys. Rev.* **89**, 1256 (1953).

[66] J. D. Jackson, *Classical Electrodynamics*, 2nd Edition (Wiley, New York, 1975).

[67] W. Nelson *et al.*, *SLAC Report* **265**, (1985).

[68] V. Prasad, Ph.D. thesis (The University of Chicago, March, 2002).

[69] G. J. Feldman and R. D. Cousins, *Phys. Rev.* **D 57**, 3874 (1998).

[70] J. R. Patterson, Ph.D. thesis (The University of Chicago, December, 1990).